Optimized Synthetic Aperture Radar (SAR) Processing for Airborne UWB FMCW Radar

By

Divya Challa

Submitted to the graduate degree program in the Department of Electrical Engineering and Computer Science and the Graduate Faculty of the University of Kansas in partial fulfillment of the requirements for the degree of Master of Science.

_____

Chairperson: Dr. Carl Leuschen

_____

Dr. John Paden

_____

Dr. James Stiles

Date Defended: Aug. 27th, 2018

The Thesis committee for Divya Challa
Certifies that this is the approved version of the following thesis:

Optimized Synthetic Aperture Radar (SAR) Processing for Airborne UWB FMCW Radar

_____

Chairperson: Dr. Carl Leuschen

Date Approved: Aug. 27th, 2018

Abstract

Remote Sensing of snow covered sea ice in melting Polar Regions has become crucial in estimating the results of increased global warming and to overcome the Earth's energy imbalance. And to accurately map the snow models over sea ice, it has become essential to build radar systems that has increased sensitivity and to use post processing techniques that enhance the performance. The Center for Remote Sensing of Ice Sheets (CReSIS) at KU has developed ultra-wideband snow radar system that operates over 2-18 GHz frequency range to effectively measure the snow thickness including very thin snow cover and map the snow-ice and snow-ice interfaces precisely. Synthetic Aperture Radar (SAR) processing is one of the post processing technique employed to further increase the sensitivity of the radar in terms of resolution and SNR. In this thesis, a time domain correlation SAR technique which is essentially a matched filter application is described and implemented. It is verified initially with an ideal simulated point target data and then with point target data collected by the snow radar system over sea-ice. Both gave the results as expected with the theoretical values. It is also shown how noise is multiplied with increasing synthetic aperture length. The effect of aircraft motion non-linearities on SAR processing are also studied at different altitudes. To overcome the effect of non-linearities and multiplicative noise, a multilooking SAR processing is proposed and explained. This is then applied to the field data collected by the snow radar in 2014 to 2017 over sea ice and observed that the azimuth resolution is improved by 4 m approximately. The optimum parameters like SAR aperture length and the number of looks are extracted based on the results of SAR processing on various data sets. Finally, a comparison of SAR application to low and high altitude data sets collected in 2016 over the same region is also provided to show that longer apertures are required for high altitude to achieve same amount of improvement in SNR and azimuth resolution.

Acknowledgements

I would like to extend my sincere thanks to my advisor Dr. Carl Leuschen for his guidance and support which made this thesis possible. Thank you for fielding my questions about research and to help me understand my thesis better and to improve it. Thank you for all the patience you had when I came with the same questions when I could not understand.

A special thank you to Dr. John Paden for taking time to answer my questions and for serving on my committee. I would like to thank Dr. James Stiles for his valuable courses on radars and serving on my committee. Also, I would like to thank Dr. Jilu Li who has been a great source of help at CReSIS.

I owe more than thanks to my parents for gifting me with constant love, my sister Sravya Challa for encouraging and being supportive all the time. They kept me grounded during some hard times. I would also like to thank my friend, Shiva, who is always there to cheer me up during stressful times and to celebrate my successes.

Thank you to all the CReSIS staff, faculty, and students for their support and friendship. I have enjoyed being a part of CReSIS and will remember my time here.

Table of Contents

List of Figures

List of Tables

1 Introduction

The new lifestyle adaptation affects the atmospheric composition and thereby the climate. These climatic changes have devastating effects on environment and life like the steady rise of global temperatures on Earth and with it comes the rise of sea level, ice sheet disintegration, loss of habitat along the coastline and many more. Earth's energy imbalance arises as a cause of such climatic forcing and the Earth's and oceanic temperatures have increased greatly over the past decade [1] and will continue to rise under current situations. Also there are studies that show that the sea level rise and melting of ice sheets is directly proportional to the temperature rise [2]. According to Intergovernmental Panel on Climate Change (IPCC), the amount of sea ice mass loss has increased to 50% from 2005 through 2012, but the measurements are not precisely accurate due to lack of complete knowledge of snow thickness [3]. On the whole, the prominent impact of the climatic change is the global temperature rise which causes melting of ice which is a major contributor to the sea level rise [2]. Hence to estimate the sea level change, ice sheet and glacier models have to be completely understood and analyzed. Due to the sensitivity of sea ice to changing climate, routine monitoring becomes very essential in order to predict the response of sea level rise to the Earth's energy imbalance.

1.1 Background

Cryosphere is the part of the Earth that contains water in its solid form like glaciers, icebergs, snow cover, ice sheets, and ground ice [4]. The potentially prominent impact of temperature rise is the aggressive reclamation of land by rising sea level caused by the melting of cryosphere components. Among all these components, snow covered sea ice and sea ice are two important subjects of study because of the snow/ice-albedo feedback mechanism. According to this mechanism, with the temperature increase, ice melts reducing the surface albedo and temperature further increases as

more heat is absorbed and likewise the converse [5]. But snow on the ice sheets can help reduce the heat transfer between the Polar Regions and atmosphere because it has high albedo and low thermal conductivity i.e., it can act as an insulation between sea ice and atmosphere reducing the aggravation of sea-ice meltdown. Scientists have estimated a sea level rise of about 6 m and 60 m if entire Greenland and Antarctica ice sheets have melted respectively [6]. Also Greenland and Antarctica snow melt runoff forms the major source of water that holds 80% of the world's fresh water [7]. Ice and snow meltdowns also are an input to the glacier mass balance. Henceforth, the study of snow covered sea ice that intersects both physical and human systems is of great importance for the present societal and climatic conditions. These studies can help in estimating sea level change and to understand and maintain the Earth's energy balance.

Radar remote sensing is one among several techniques to monitor the cryosphere and an important one to study the snow cover. Remote sensing of the glacial ice and snow by active sensors like Radar (Radio Detection and Ranging) has started in the late 1970s with the launch of Seasat [4] and advances are made each day for improved ice sheet modelling. While the space borne radar systems maps the ice surface elevation, the airborne radar systems give measurements of the three-dimensional structure of the snow and ice thickness with good resolution.

Snow accumulation rates are needed to understand ice sheet mass and snow cover on sea ice is important to understand snow loading and estimate sea ice thickness and snow depth from freeboard measurements. While there is so much research that has been done on the glacial ice and snow covering the glacial ice, there are still parts of the Greenland and Antarctica snow covered ice sheets that are needed to be studied [8, 9]. The significant factors for the better and improved climate monitoring are snow thickness on sea ice which contributes to the heat exchange between sea ice and atmosphere because it acts as an insulation layer between atmosphere and ocean.

Scientists are also interested in finding snow water equivalent since snow can serve as a fresh water resource. And hence snow depths, thick or thin has to be precisely observed to carefully monitor the snow cover on sea ice and land [10, 11, 12].

1.2 Motivation

As mentioned earlier in section 1.1, it is essential to obtain accurate models of snow covered sea ice and estimate snow thickness. The ice sheet dynamics and regular ice formation lead to thin snow cover and also the snow cover is variable in different regions. In addition to this, the snow present over sea ice also vary in physical and dielectric properties which affect the radars return signal. For example, the radar's signal penetration depth is low for wet snow zones and it increases over dry snow zone. The snow particle size and densities also affects the signal return. The radar echoes can be weak when the snow-ice interface is very rough [12]. Therefore, to unambiguously detect the snow-ice and snow-air interfaces, greater resolution images are required to accurately determine the snow thickness over sea-ice and land which is vital for future global warming prognosis. It is important to use wideband radar systems for optimum radar performance and to employ processing techniques that can handle the challenges posed by them. Signal-to-noise ratio (SNR) and resolution has to be improved to a level that all sidelobes are suppressed to obtain accurate snow-ice and snow-air interface models.

In order to address all the above mentioned issues and to measure the snow cover on sea ice and high resolution snow layering on ice sheets precisely, finer resolutions are required and thereby increased bandwidth. At University of Kansas (KU) and Center for Remote Sensing of Ice Sheets (CReSIS), polar snow thickness measurements are being done by developing airborne radars and collecting high resolution data. We designed and built 2 wideband radars operating at 2-8 GHz and 12-18 GHz called snow and Ku-band radars respectively. To improve the performance, an

ultra-wideband radar of 2-18 GHz is also built for better resolution images. These are operated as part of NASA's Operation Ice Bridge (OIB) mission and large Polar Regions are studied.

Antenna arrays and additional post processing techniques like deconvolution, Synthetic Aperture Radar (SAR) processing are also used to further improve the performance. SAR systems have a side-looking imaging geometry with a radar installed on a forward moving platform. In the platform's direction (along-track dimension), SAR techniques help improve the azimuth resolution and SNR which enables us to distinguish the snow-ice and snow-air interfaces and measure thickness of very thin snow cover.

1.3 Objectives

The objective of this work is to validate a time domain SAR processing technique with simulated data and to optimize it for 2-18GHz Ultra-wideband (UWB) FMCW radar. **We analyze how SAR processing affects the SNR, resolution, beamwidth for various parameters like altitude of the aircraft, frequency of the radar, length of the synthetic aperture, number of looks and see how we can handle them for 2-18GHz bandwidth**. This SAR processing is applied to corner reflector and the radar data collected by the KU-band and snow radar to see how the SNR and along-track resolution is improved and compare them to the theoretical values and results obtained from the simulated data. SAR processing is also extended to the Multi look SAR processing to reduce the sensitivity to unknown platform motion and the speckle noise generated through SAR processing. We also looked at the parameters that would give the optimum results for the UWB radars like the SAR aperture length, number of looks in multi-look SAR.

1.4 Organization

There are a total of 6 sections in this Thesis. The first section describes a brief background to the work, motivation behind the work, the research objectives and an outline of the thesis. The second

chapter describes various radar systems built at CReSIS, its applications and the past measurements, complete hardware design of the Ku-band and snow radar. The third chapter elaborates the existing signal processing of the radar raw data from the CReSIS toolbox, additional signal processing methods like SAR processing and elaborates the techniques useful for accuracy like the motion compensation. Fourth section explains in detail the time domain correlation SAR processing technique, aircraft non-linearities affecting SAR processing. This also describes multilook SAR processing and how this can resolve the non-linear effects of the path. Fifth chapter provides some of the results when applied to simulated point target, corner reflector and the field data for various SAR parameters. It also provides a comparison of SAR processing application to low and high altitude data. Sixth part concludes the thesis with summary of the work, and future work that can be done.

2 Radar System and Applications

This chapter introduces radar systems and its applications briefly. The radar systems developed at CReSIS, data collected with these radars, and the signal processing that is applied to the raw radar data collected is described. CReSIS have developed two wideband FMCW radars, one of them is the snow radar which operates at 2-8 GHz frequency range and the other is the Ku-band radar that operates in 12-18 GHz. For better performance of the system and increased range resolution, a new ultra-wideband snow radar is developed and deployed which operates over a larger frequency range of 2-18 GHz. The detailed description of these radar systems and the achievable performance metrics like SNR, resolution with these systems is provided.

2.1 CReSIS Radar Systems

Radar systems operate by transmitting an electromagnetic wave through a transmitting antenna and detecting the reflected signal with a receiving antenna. This echo undergoes a series of signal processing techniques and required information is extracted from this processed echo depending on the application. Radar systems find its application in many fields like surveillance systems, air-defense systems, RADAR astronomy, remote sensing, geological observations, etc.

At CReSIS, several airborne radars have been designed and deployed for sounding and imaging of the ice sheets in the Polar Regions. It started with Multichannel Coherent Radar Depth Sounder (MCoRDS) which operates over a frequency range of 140-230 MHz [13] which could produce vertical resolution of about 6m in ice. Then an eight channel wideband Synthetic Aperture Radar (SAR) operating at 160-230 MHz is developed [14] which gave a resolution of 1m. To improve the performance of the system, several wideband, greater frequency and multi frequency radars are being developed since then. A wideband UHF radar that operating over a greater bandwidth of

600-900 MHz to map the near surface internal layers known as “Accumulation Radar” is deployed and resulted in an improvement of vertical resolution to 60cm [14]. To further improve the resolution of the system, ultra-wideband FMCW radar known as “Snow Radar” is developed and flown on NASA P-3 and DC-8 aircrafts [13]. This operates over the frequency range of 2-8 GHz and could achieve a range resolution of 5 cm. And then this is extended to frequencies from 12 to 18 GHz which falls within Ku band from Standard Radar frequency nomenclature and hence the radar termed as “Ku-band radar”.

2.1.1 Snow Radar

The 2-8 GHz snow radar uses Ultra-Wideband Band (UWB) Frequency Modulated Continuous Wave (FMCW) linear chirps and the advantages of using FMCW in airborne radars over other waveforms has been explained in [15], [16], and [17]. Brief summary of this system hardware is given below and the complete description of the system can found in [15], [18], and [19].

At the transmitter section, a 600-900 MHz linear chirp with a pulse duration of 240 us and 2 KHz Pulse Repetition Frequency (PRF) is generated by the Direct Digital Synthesizer (DDS) [18]. This is filtered and frequency multiplied 20 times by a Phase Locked Loop (PLL) to obtain a 12-18 GHz chirp which is then low pass filtered to 2-8 GHz chirp by a 10GHz Phase Locked Oscillator (PLO). Thus generated signal is transmitted, received and processed. This radar is deployed in seven NASA aircrafts for low altitude measurements in Arctic and Antarctic regions and could map to depths of 40 m [14]. The normalized beat frequency signal when tested with a 2.95 us delay line has shown a side lobe of -20 dB approximately and the Range resolution achieved was about 5 cm in air [13].

2.1.2 Ku- Band radar

While snow radar is used for near surface measurements, Ku-band radar operating from 12 to 18 GHz is for high precision surface measurements. The entire system description and its system performance has been clearly given by Patel [20], [21] and Gomez-Garcia [22]. An overview of the system is presented here.

Ku-band radar system is also an FMCW radar system designed for an optimum performance at altitudes of 500m and higher. The system hardware is similar to that of snow radar. The transmit signal is generated by Voltage Controlled Oscillator (VCO) with a PLL. The reference chirp from 900 to 600 MHz is generated and frequency multiplied to achieve a linear chirp of 12-18 GHz with a length of 250 us and a PRF of 2 KHz. A 20 dBi standard gain horn antenna with 3 dB beamwidth of 19 degrees is used to transmit and receive the reflected echo. This received echo is processed to generate the echograms. The performance of this radar is measured with an impulse response by passing through a delay line and the range sidelobes are found to be 20 dB less than main lobe [22]. This is flown on NASA's DC-8 aircraft and NSF's Twin Otter aircraft and used for mapping over depths of 10 m [14].

2.2 2-18 GHz UWB Snow Radar

A new snow radar is developed for operating over the range of both snow and Ku-band radar i.e., 2-18 GHz to achieve the combined advantage of determining snow thickness with finer resolution over both sea-ice and land and measure SWE. This ultra-wideband snow radar is a FMCW radar and the whole system hardware description is given in detail in fig. 1. The entire radar system can be categorized into four sections: chirp generator, RF section, IF section, and Data Acquisition unit.

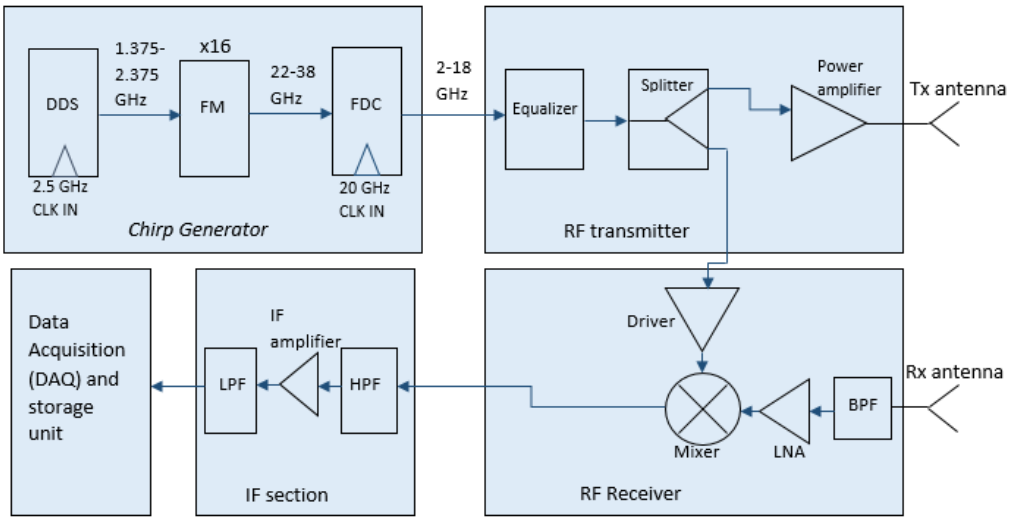

Figure 2:1 Snow radar hardware description

The chirp generator produces a 2-18 GHz linear chirp in a 3 step process. The DDS generates a frequency modulated chirp of 240 µs length over the frequency range of 1.375-2.375 GHz by a Field Programmable Gate Array (FPGA) [23]. A frequency multiplier (FM) now multiplies this base-band chirp by 16 times to a 22-38 GHz chirp. This is now down converted to our desirable frequency of 2-18 GHz chirp by a Frequency down-converter (FDC) by mixing with a 20 GHz PLO.

In the RF transmitter section, the chirp is amplified, filtered and fed to the transmitting antenna. The reflected signals from the target are captured by the receiving antenna and sent to the RF section at the receiver end.

At the RF receiver section, the received RF signals are band pass filtered and amplified by a low noise amplifier (LNA). Then they are multiplied with the transmitted signal to convert them to IF frequency. These IF frequency signals called as beat frequency signals contain information on range and scattering properties of the target. In the IF section, they are again filtered to remove any other noise present.

The beat frequency signals are digitized using 14-bit ADC which has a sampling rate of 125 MSPS and stored using a RAID controller. The receiver's minimum detectable signal (MDS) is between -125 dBm and -130 dBm over the frequency range of 2-18 GHz with a gain of 60 dB [23].

Antenna configuration:

This radar is operated for National Aeronautics and Space Administration (NASA), Operation Ice Bridge (OIB) on DC-8 and P-3 aircrafts and also National Science Foundation (NSF) on Twin Otter aircraft. For the Twin Otter system, two 2-18 GHz horn antennas separated by a distance of 6 m are used in nadir mode with a minimum isolation of 80 dB at 2GHz [25]. And 10 x 10 dual-polarized Vivaldi antenna array is used at 30^0 off-nadir. Fig. 2.2 below shows both these antennas when mounted on an aircraft.

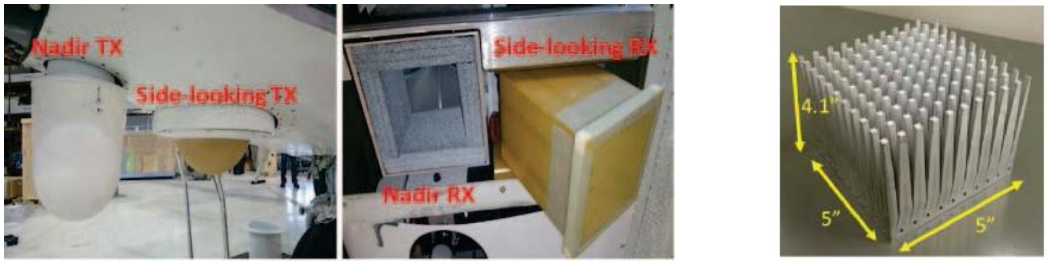

Figure 2:2: Transmit and Receive antennas mounted on front and back of the Twin Otter aircraft (left & middle) and Vivaldi array antenna (right) for off-nadir mode [24]

For the NASA DC-8 and P3, a set of Horn antennas with antenna gain of 10 dBi and beamwidth of 45 degrees were used for transmitting and receiving operations. The transmit and receive antennas are isolated by 70 dB for the DC-8 aircraft and 50 dB for the P3 aircraft [14]. CAD models of the DC-8 and P3 aircrafts and antenna installation on the aircrafts are shown in fig. 2.3.

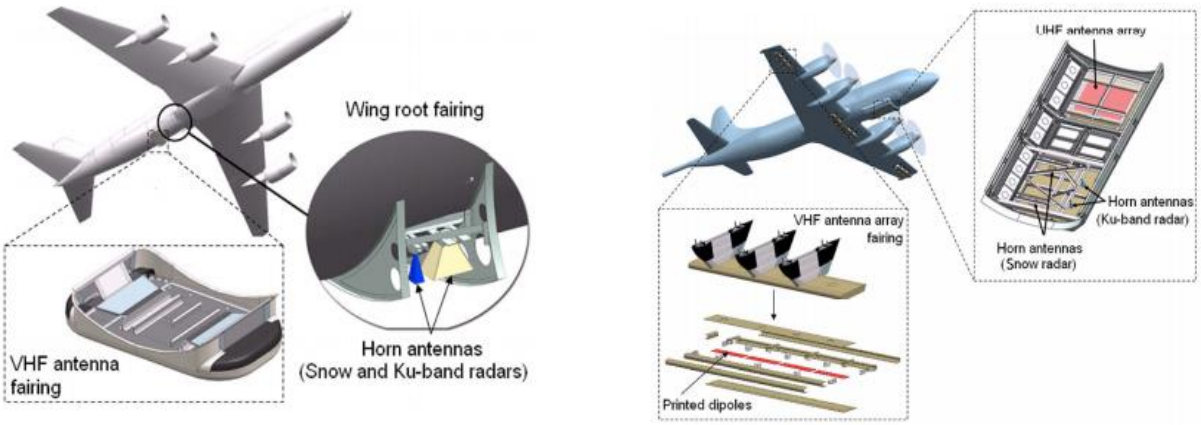

Figure 2:3: CAD images showing the antenna structures on aircrafts. Left: NASA DC-8; right: NASA P3 [14]

The complete list of system specifications of all the three radar systems are given in Table 1.

Table 1: Snow Radar system specifications

PARAMETER	*UNIT*	*Ku-band radar*	*Snow radar*	*New snow radar*
Operating Frequency	GHz	12-18	2-8	2-18
Bandwidth	GHz	6	6	16
Range Resolution	cm	4	4	0.94
Chirp Length	µs	240	240	240
PRF	kHz	2	2	3.9
Peak Power	dBm	20	24	34
ADC sampling rate	MSPS	125	125	125
ADC Resolution	bit	14	14	14

The data collected with this is signal processed and the resolution that can be achieved with this new UWB snow radar is 1.64 cm which is greater than Ku-band and 2-8 GHz Snow radar. The signal processing steps required to obtain the final echograms are explained in detail in the next chapter.

3 Current Radar Data Processing (CReSIS Toolbox)

This section of the thesis explains the signal processing steps to generate the echograms from the raw data collected and extract information like backscattering coefficient, snow cover thickness, etc. from those echograms. It also explains advanced signal processing steps like the coherent noise removal, deconvolution, radio frequency interference (RFI) suppression, and coherent and incoherent processing that are in the CReSIS toolbox that allows for more accurate measurements by overcoming the signal loss.

3.1 Signal Processing

Chapter 2 explained in detail the hardware designs of the radar systems built at CReSIS. These radars are mounted on different aircrafts in different seasons to study the snow cover at various regions of Greenland and Antarctica. Once the radar systems operate and collect the raw data over the snow surface, this raw data has to be converted to images that contain information about the surface and the underlying layers called “echogram”. The basic processing steps to generate an echogram from the radar data are mentioned here.

The received raw data is a 2-D matrix with fast time and slow time samples. These are several pulses with same pulse duration, bandwidth, and center frequency. This raw data is windowed using a Hanning window to reduce the sidelobes and to improve the vertical range resolution. Now FFT is applied in the fast time domain to deconstruct the time domain data into the frequency domain or the range domain. This process is analogous to the pulse compression. A high pass filter is applied in the azimuth dimension to remove any coherent noise present. The causes and filtering of coherent noise will be discussed in detail in section 3.1.1. These are the basic processing steps performed for any echogram generation. Incoherent processing is done as a part of CReSIS’s routine data processing and when SAR processing is not applied. For each range-bin, 5 along track

range lines are incoherently processed to reduce fading and then decimated by 5 in along-track dimension. The processed data is also elevation compensated to remove large platform motion errors to produce an echogram. The detailed compensation method is described in a further section.

Before the actual deployment of the radar, laboratory tests are done to characterize the radar in terms of output power, frequency nonlinearity of the chirp. These non-linearities increase with range and affect the sidelobes [14, 23]. So to determine full the system response, laboratory experiments are conducted using a 260 m optical delay line as the distant point target. The delay line is simulated using the processing steps mentioned above and the systems loopback (transmitter and receiver connected by a delay line) measurement is shown in fig. 3.1. The 3dB resolution for the delay line is found to be 1.14 cm and the peak side lobe around -30 dB less than the main lobe.

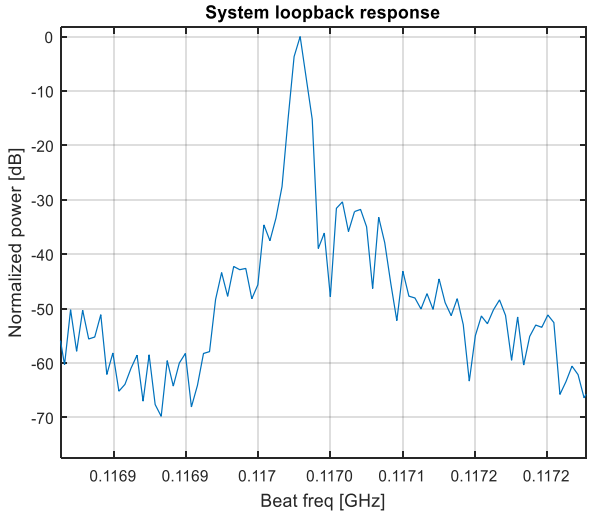

Figure 3:1 Received signal after processing measured in the laboratory for 2-18 GHz snow radar [23]

The actual field results generated from data collected are available on CReSIS website [26]. An example of the snow radar echogram from field data collected in March 2015 during the NRL sea ice survey in Barrow, AK is shown in fig. 3.2. This echogram is generated from all the processing steps mentioned above and we can clearly see range sidelobes and coherent IF signals.

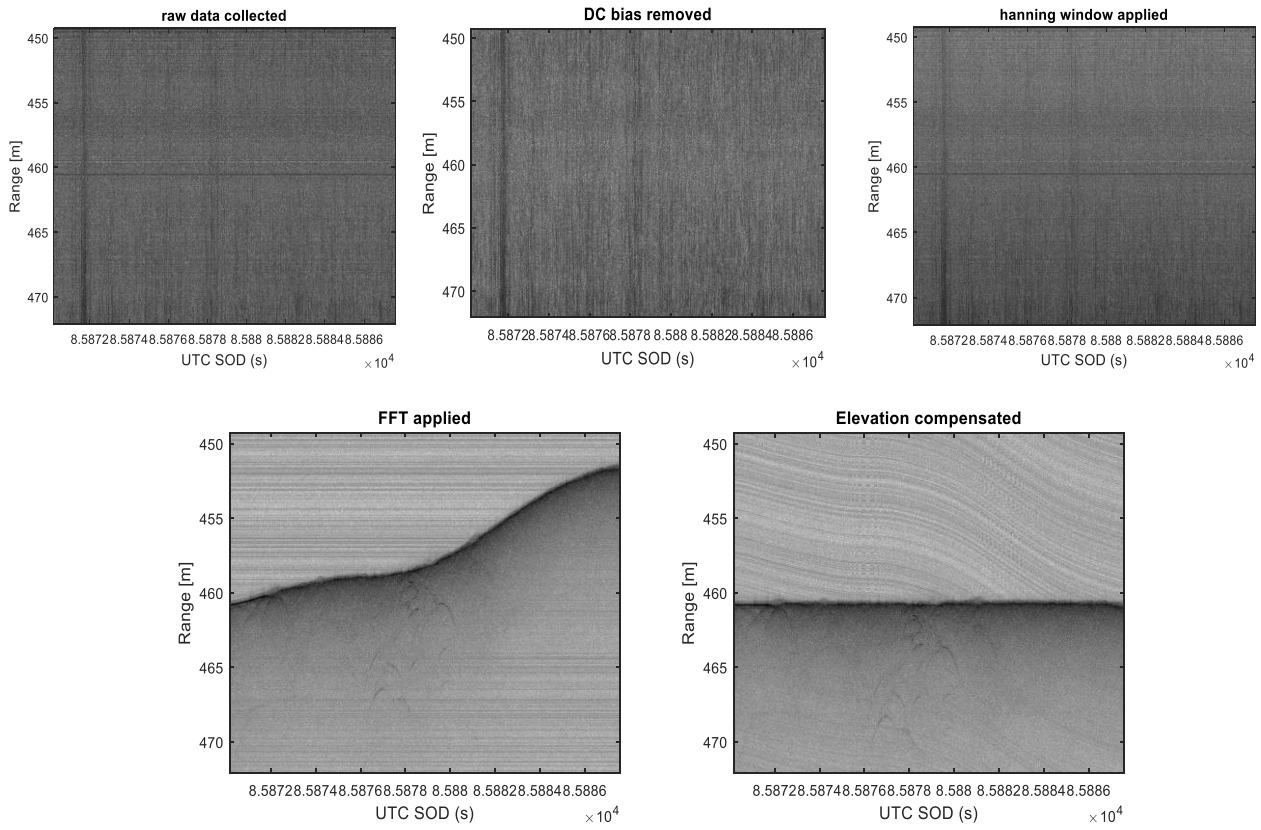

Figure 3:2: Example of snow radar echogram over sea ice without any additional processing steps

3.1.1 Coherent noise removal and deconvolution

Additional processing steps must be implemented to reduce the noise and other undesirable effects and further improve the signal quality significantly. Some of these include removal of coherent noise and suppression of range sidelobes. In the snow radar system's chirp generation described in chapter 2, after the FM and FDC sections there are in-band intermodulation products (IMDs) generated along with the chirp. These IMDs can intermix or mix up with the echoes to produce unwanted signals i.e., coherent noise. The causes of coherent noise might be many but the main reason is the system itself like signal coupling between antennas, and non-linearities within the hardware components. This coherent noise cannot be filtered by IF filters and thus removed by applying a mean filter in slow time domain. The cause of range sidelobes are the system deformities like the system component reflections, frequency non-linearities, etc. and can be

reduced by deconvolving with the system response. Since the system s response is difficult to be determined after aircraft platform integration, response of an open water lead on sea-ice where the SNR is very high is approximated for the system response for deconvolution. An example showing these 2 steps is shown in fig. 3.3.

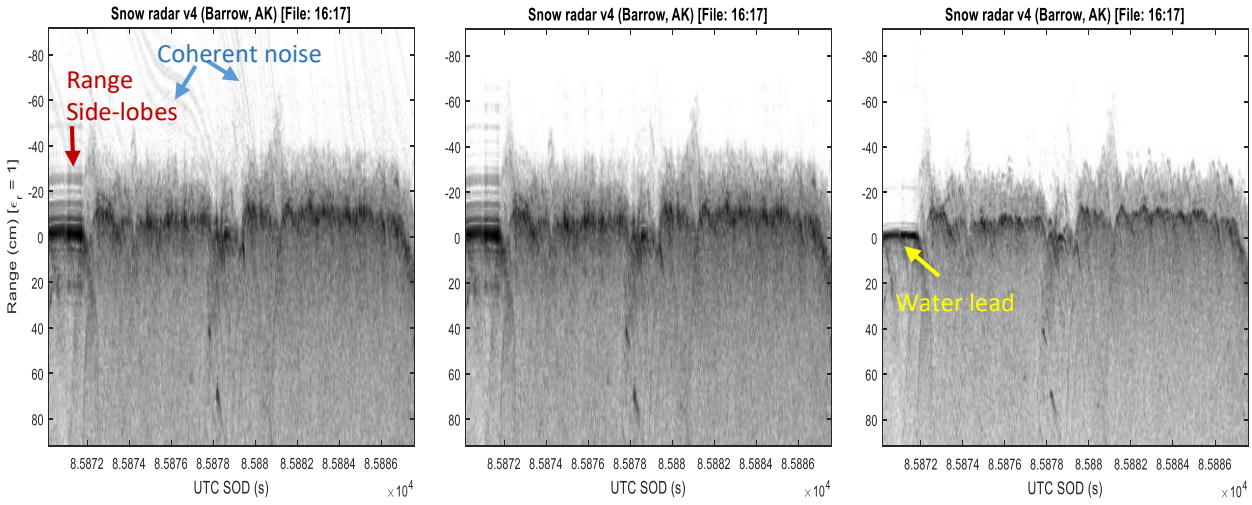

Figure 3:3: (a): Snow radar echogram without additional processing steps; (b): Coherent noise removed; (c): Echogram after coherent noise removal and system response deconvolution.

To study the snow cover over ice and land, and to accurately measure the snow thickness including very thin snow with a few centimeters thickness, and also to measure the backscatter we have increased the bandwidth and developed 2-18 GHz snow radar. But to accomplish this, in addition to the optimized hardware design, radars also must maximize the sensitivity by overcoming the signal loss with post data processing. One such advanced signal processing technique to improve the SNR and enhance the echogram quality further is SAR processing.

3.2 Geometric resolution of radar data

Geometric resolution is defined as the sensor's ability to distinguish between targets located closer and to effectively image them into pixels in either fast time (Range) or slow time (Azimuth) dimension. And to precisely determine the snow thickness of very thin snow cover, high resolution

models are very much required. In this section, a brief discussion of Range and Azimuth resolution is provided along with some of the options to improve them.

Range Resolution:

Generally, range resolution is proportional to the pulse duration. But designing hardware to generate and transmit pulses of very short duration is practically expensive and leads to low SNR. So, to overcome this the longer pulses are frequency modulated and range resolution of an LFM chirp can be derived by approximating pulse duration to inverse radar bandwidth [27, 28, and 29].

$$\Delta r = \frac{c_0}{2\,BW\,\sqrt{\varepsilon_{snow}}}$$

Where c: speed of light

BW: Receiver bandwidth

$\sqrt{\varepsilon_{snow}}$: Relative permittivity of snow defined as [27] $\sqrt{\varepsilon_{snow}} = (1 + 0.51\rho_{snow})^{3/2}$

For the 2-18 GHz snow radar, the range resolution is 0.9375 cm.

Azimuth resolution:

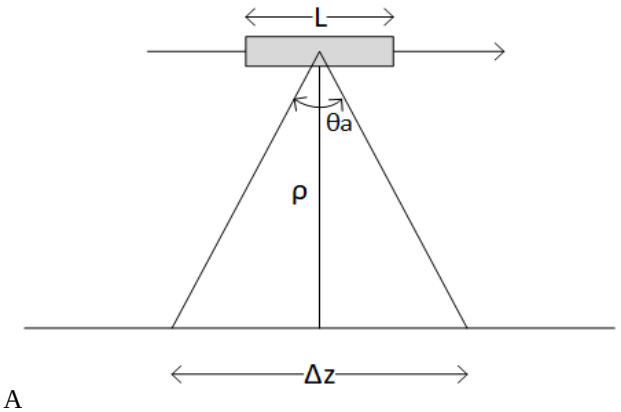

A

Figure 3:4: Geometry in the azimuth plane

From the geometry shown in fig. 3.4, it is obvious that azimuth resolution is the width of the antenna footprint. Thus the azimuth resolution for a real aperture radar (RAR) [30, 31] is given as

$$\Delta z_{rar} = \rho \, sin\theta_a = \frac{\rho\lambda}{L} = \frac{\lambda \, H}{L \cos\theta_a}$$

Where ρ is the nominal slant range which is dependent on height of the (H) and the antenna azimuth beamwidth (θ_a). Approximating the resolution for small angles (<1% for angles less than 13^0 and <10% for angles less than 42^0) and the azimuth beamwidth as $\theta_a \approx \lambda/D$, the azimuth resolution of a real aperture radar would now be

$$\Delta z_{rar} \approx \frac{H\lambda}{L}$$

Where λ is the wavelength and L is the antenna length in azimuth direction [31]. The length of the horn antenna for 2-18 GHz radar is 27.9 cm, the azimuth resolution for aircraft altitude of 500 m is 53.76 m which is very large.

It is evident from the above equation that longer antenna lengths produce finer azimuth resolutions. But due to the practical implications, shorter antennas are used but the azimuth resolutions can be improved by applying SAR processing.

The azimuth resolution of synthetic aperture radar can be determined with the help of the SAR geometry shown in below fig. 3.5 and the complete deduction is explained in [31, 32].

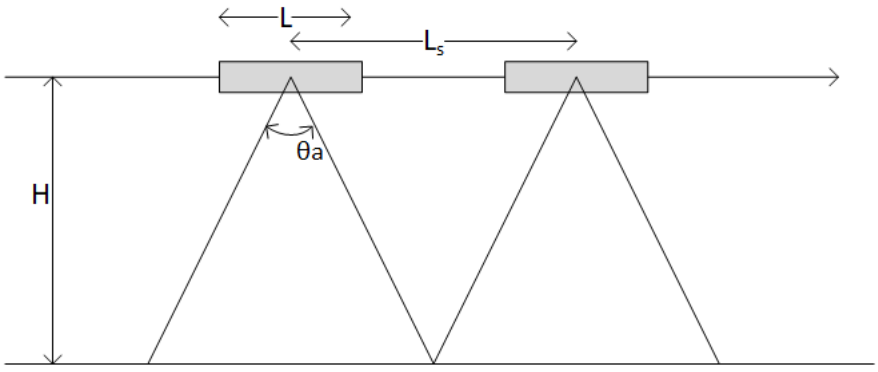

Figure 3:5: Elaborated geometry for azimuth resolution using synthetic apertures

In the above fig., for an antenna length of L moving at v m/s velocity, Ls is the maximum synthetic aperture length that could be achieved. This synthesized aperture length will result in a beamwidth equal to

$$\theta_s = \frac{\lambda}{L_s} = \frac{L}{2\,H}$$

Above statement shows that greater synthetic aperture lengths provide better resolutions. This gives us an antenna footprint as

$$\Delta z = H\,\theta_s$$

The finest azimuth resolution (Δz) that can be achieved with synthetic aperture is

$$\Delta z = \frac{L}{2}$$

From the above equation, it is shown that azimuth resolution is independent of aircraft altitude and wavelength and also shorter antenna lengths give finer resolutions. This is because with shorter antennas, we get wider beam widths and thus more area that is spanned by the antenna which makes the maximum synthetic length that can be considered higher. Also it can be implied from this concept that higher the altitude, larger is the antenna footprint and longer the maximum achievable synthetic array. But then the increase in distance gives us poorer resolution which is like being compensated by longer synthetic arrays. This concept is explained in detail in further sections. The maximum attainable azimuth resolution for 2-18 GHz would be 0.1395 m irrespective of aircraft altitude.

3.3 SAR Processing

3.3.1 SAR Introduction

The history of Synthetic Aperture Radar (SAR) imaging dates back to a very old time of 1950s [33] and has evolved since then accommodating several improvements in ice sheet mapping.

Spaceborne and airborne SAR has helped for better mapping of surface and basal conditions [34, 35, and 36]. There are two major advantages with SAR processing. Firstly, it improves the SNR and help us measure the snow thickness accurately since all the noise is suppressed to a very low level. Secondly, we can achieve finer resolutions with the synthesized longer apertures.

SAR is a two-dimensional (2D) imaging application where one dimension is range which is perpendicular to the radar's platform motion and the other is azimuth or along-track which is in the direction of radar's platform motion and orthogonal to radar beam. The azimuth resolution defined as the ability to distinguish various point targets in the azimuth direction is determined by the beam width of the antenna. The beam width is variant with the physical length of the antenna. So along-track length of the antenna can be increased to increase the azimuth resolution. But practical limitations arise to mount a large antenna on the aircraft and it also would not be cost effective. The solution to achieve finer resolutions in along-track dimensions without increasing the antenna length is to use the synthetic aperture technique.

3.3.2 SAR Processing Techniques

SAR processing utilizes the movement of the aircraft with respect to the target. As the aircraft progresses through the target, many beams are sent and received at different geometric positions as shown in figure 3.6 and when these return signals are coherently processed, images with the resolution of a wider aperture are generated.

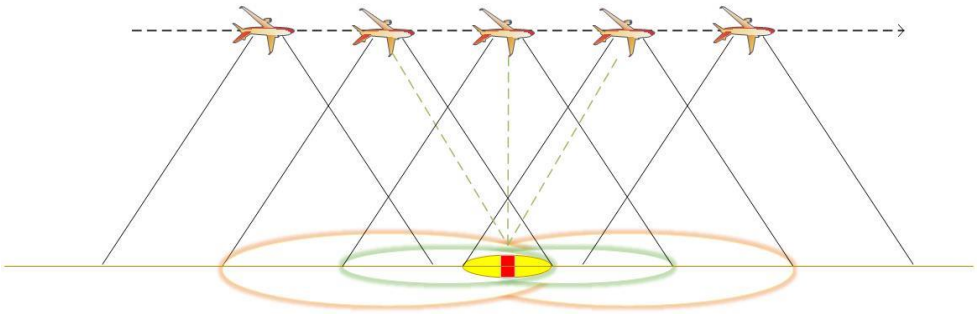

Figure 3:6 Radar signals transmitted and received at different positions

There are various SAR processing algorithms to focus the dispersed energy of a point target into a single point in both time and frequency domain. The frequency domain algorithms include Range-Doppler, Chirp-Scaling or f-k migration algorithm [37, 38, and 39]. The frequency domain algorithms are generally fast and takes advantage of the FFT in both domains. The algorithm that is being used in the current CReSIS toolbox is f-k migration method.

3.3.3 Elevation Compensation

Many SAR techniques require constant aircraft height throughout the flight path, but it is not possible in reality. These height variations result in defocusing, shift of target's location, etc. when SAR processed and hence these variations must be compensated for SAR processing. The original data collected is multiplied by $e^{jk_{air}\,2\delta h}$ [39] in frequency domain to get the elevation compensated data where δh is the height variations with respect to nominal height. This height variation can be determined from the Onboard GPS recordings taken as

$$\delta h = h_{gps} + \Delta h - mean\left(h_{gps} + \Delta h\right)$$

where $h_{gps}$is the elevation from the onboard GPS measurements, Δh is the height difference between antenna and onboard GPS receiver. This is obtained using flight dynamics with respect to Earth's coordinate system and the entire explanation of the derivation is given in [40]. This is implemented in Matlab. The original data is processed, and an echogram is generated. Now with the elevation from onboard GPS measurements, the shift index for each range line by which the data has to be shifted in fast time domain with respect to initial elevation for corresponding data is estimated as

$$elevation\ shift = \frac{elevation\ - initial\ elevation\ of\ data\ file}{dt * c}$$

Where c: velocity of light, and dt: fast time sample or fast time spacing

Now the original data file is shifted by the shift indices determined to get the compensated data.

An example of data before and after elevation compensation is shown in fig. 3.7.

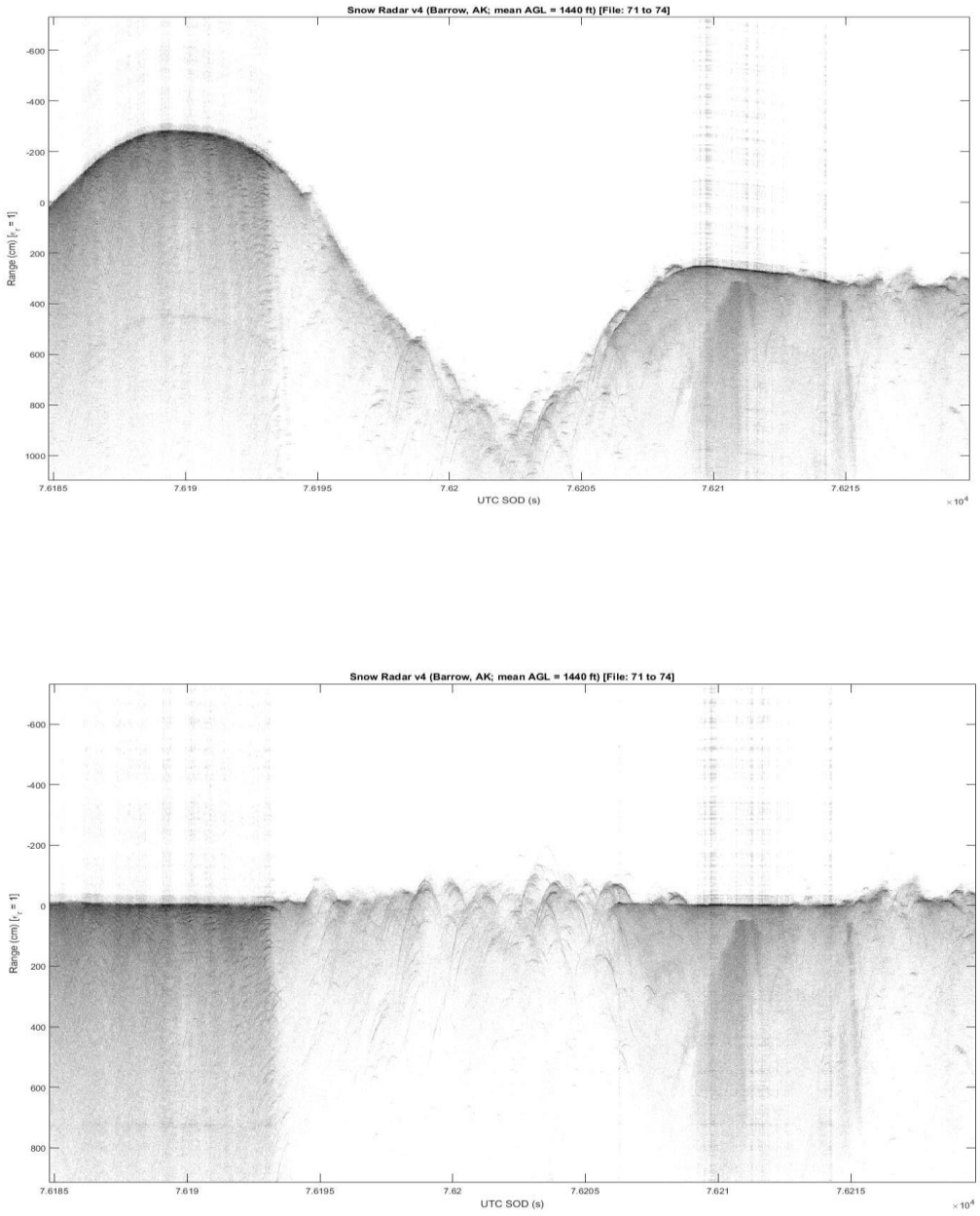

Figure 3:7: Snow radar echograms top: before elevation compensation bottom: after elevation compensation

3.3.4 f-k algorithm

The SAR algorithm that exists in the CReSIS toolbox is the f-k migration algorithm. The frequency-wavenumber (f-k) algorithm is implemented in Matlab and the process is explained here:

(1) The received raw data is processed as mentioned earlier in the signal processing section i.e., data is filtered and pulse compressed in frequency domain. To save memory, decimation in fast time can also be applied here. The data is now ready for SAR processing.

(2) SAR processing parameters like the aircraft altitude (h), velocity (v), frequency (f), wave numbers in both the directions (k_x, k_z) required are now computed from the known system parameters. The aircraft altitude is determined from heights obtained all along the along-track. Any unusual errors like sudden jump of the aircraft are corrected by comparing the altitude at both neighboring locations and assigning the value of previous location at the jump. For carrier frequency (Fc), frequency spacing (Δf), and along-track wave number spacing (Δk_y): the parameters f, k_x, and k_z are given as [40]

$$f = F_c + [-\frac{n}{2}\,\Delta f : \Delta f : \left(\frac{n}{2} - 1\right)\Delta f]$$

$$k_x = [-\frac{m}{2}\,\Delta k_y : \Delta k_y : (\frac{m}{2} - 1)\Delta k_y]$$

$$k_z = \sqrt{4k^2 - k_x^2}$$

Here k_z is estimated from the wave equation obtained with the wavefront reconstruction (WR) theory. According to WR theory explained in [41], the EM signal of radar is described by the wave equation

$$\left(\frac{\partial^2}{\partial x^2} + \frac{\partial^2}{\partial z^2} - \frac{4}{c^2}\frac{\partial^2}{\partial t^2}\right) S(x,z,t) == 0 \qquad (3.1)$$

Where x: horizontal coordinate (along-track), z: vertical coordinate (range track), t: time, and c: speed of light. This wave equation is converted to f-k domain by FFT in both slow time and fast time dimensions and inversely time domain equation can be found by IFFT as

$$S(x,z,t) = \int\int S(k,z,f)e^{(2\pi ft-kx)}dk\ df \tag{3.2}$$

Substituting 3.2 in 3.1, we can solve for reflectivity and refraction indices. The complete description is given by Dr. Jilu Li in [12].

(3) The SAR parameter, h mentioned above is expected to be constant and it is not. The motion correction is done with elevation compensation explained in section 3.2.3.

(4) Now FFT is performed in the slow time domain transforming signal S(f, x) to S(f, k_x).

(5) An idealized antenna radiation pattern is implemented in the k domain and is called as "K-filter" which determines the synthetic aperture length over which the data is integrated. The K-filter geometry thus takes the form of an ideal radiation case as shown in fig. For an aircraft at height h, having an antenna element with beamwidth β, the synthetic aperture length from the geometry is

$$L = 2h\tan(\frac{\beta}{2})$$

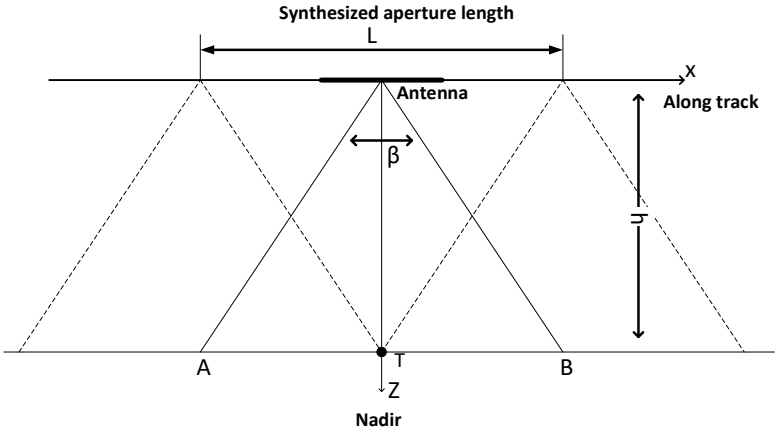

Figure 3:8: SAR imaging geometry

This geometry in f-k domain yields

$$\frac{\beta}{2} = sin^{-1}\frac{k_x}{2k}$$

Thus, the K-filter becomes

$$K_{filter} = 1 \qquad if \left|sin^{-1}\frac{k_x}{2k}\right| \leq \frac{\beta}{2}$$

$$K_{filter} = 0 \qquad if \left|sin^{-1}\frac{k_x}{2k}\right| > \frac{\beta}{2}$$

Now that the data is prepped for SAR processing and a K-filter is built, this filter is applied to the data in the f-k domain and windowed over k_x domain to reduce any side lobes using Hanning window.

(6) The data is now at the aircraft height h and it has to be migrated to the snow surface by multiplying the data with $e^{j\,kz\_air\,h}$.

(7) Sum up all frequency components at each depth by migrating the data through all range bins with a step size. This is nothing but summing the samples in each column.

(8) Now take IFFT of the data for all depths to get a final SAR processed image.

This algorithm is implemented for real data and found to increase the SNR and the azimuth resolution [11].

Summarizing, the signal processing steps to get the final echogram from the raw data collected is shown with a flow chart below.

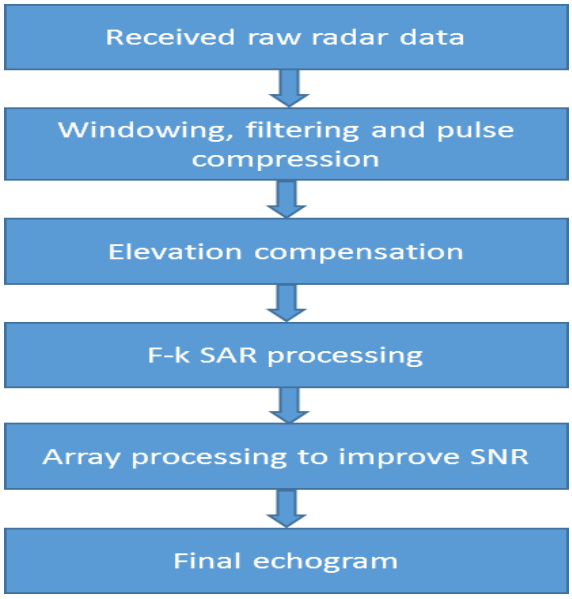

f-k migration technique which is based on wave front reconstruction concept takes care of the refractive properties of the wave until deeper layers to the bedrock as shown in fig. 3.9 but has a drawback of perfect motion compensation before SAR application. So this is generally ideal when refractive indices of the air-ice interface has to be taken into account like for MCoRDS which is developed to study the deeper layers of ice sheets. However, snow radar is developed for snow depth estimation which is present just few meters from the surface and deep and hence the inclusion of refractive index can be ignored for SAR processing. Time domain algorithms and the one we are choosing for our work are described in the next chapter.

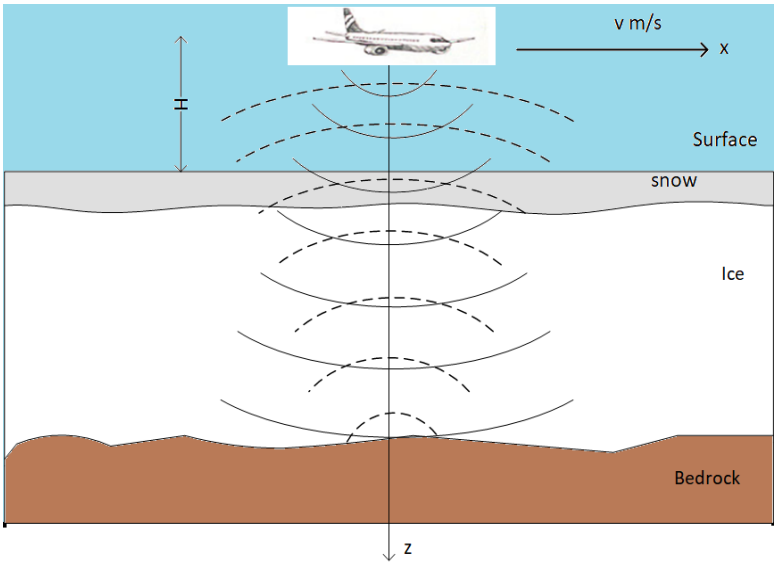

Figure 3:9: Wave fronts through the ice layers

4 TIME DOMAIN CORRELATING SAR PROCESSING

In the previous chapter we have seen the data processing flow from the raw data received to a final echogram. We have also discussed about the history and importance of SAR processing. While there are several SAR processing techniques, we have seen in brief about f-k SAR processing method which is in the CReSIS toolbox. In this chapter, time domain correlation SAR processing technique and the SAR simulator are explained elaborately. Multilook SAR processing is also introduced and explained.

4.1 Time Domain Correlation SAR Technique

In frequency-wavenumber (f-k) migration algorithm, the range is corrected by applying a phase shift in frequency domain. The drawback with this is it assumes the radar platform completely linear during the data acquisition while it is practically not possible and hence the data has to be corrected for elevation changes. An alternate way is to use the time-domain algorithms like Time Domain Back Projection (TDBP) and Time Domain Correlation (TDC) methods. Time Domain Correlation (TDC) is one technique where matched filter is implemented through sliding inner-product and Time Domain Back Projection (TDBP) is similar to TDC but the kernel is not constant, it updates with aircraft position. The algorithm we have adapted in this work is the TDC method because it is easy to implement. This technique cross correlates the radar data with the ideal point target data generated using given radar parameters making it a matched filter applied in space-time domain. To overcome the effects of non-linear trajectories, multilook SAR is implemented where the synthesized aperture is divided into looks which is discussed further in detail with example. TDC SAR algorithm is developed in Matlab for radar data. Let us see how this matched filter is built and used in the next sections. An assumption made here is that the phase across the antenna

footprint is solely due to aircraft motion and all observation angles are constant. Also the refractive index is ignored in this because snow is mostly on the surface and the refractive index of air is 1.

4.1.1 Synthetic Aperture Radar Simulator

SAR processing using time domain correlation is similar to applying a matched filtering and to generate the matched filter simple point target data is generated with the parameters same as snow radar. The required parameters for SAR simulator are mentioned in table 2 to 4.

Table 2: Waveform parameters

Parameter	***Symbol***	***Value***
Pulse duration	T_{pd}	240 us
Bandwidth	B	16 GHz
Start Frequency	F_0	2 GHz
Stop frequency	F_1	18 GHz

Table 3: Platform parameters

Parameter	***Symbol***	***Value***
Aircraft Altitude	H	500 m
Aircraft velocity	v	105 m/s

Table 4: Scene parameters

Parameter	***Symbol***	***Value***
Along track sample size	$\Delta x = v$. presums / PRF	0.2110 m
Scene Along track Length		461.4982 m
Sample Interval	Δt	3.9918 ns
Sample start time	ts	0 us
Sample stop time	tf	240 us
Number of fast-time samples	Nt	29890

Number of slow-time samples	Nx	2192
Target depth	d	500 m

The radar transmits a linear FMCW chirp $S_{tx}(t)$ of the form

$$S_{tx}(t) = \cos(2\pi f_0 t + \pi k t^2)$$

Where f_0: central frequency of the chirp

t: fast time of the signal

$k = \frac{B}{T_{pd}}$ is the chirp rate with B as the signal bandwidth and T_{pd} as the signal pulse duration

This transmitted signal is scattered by a single point target and the delayed echo is received by the radar as $S_{rx}(t)$

$$S_{rx}(t) = \cos(2\pi f_0 (t - t_0) + \pi k (t - t_0)^2)$$

Where t_0 is the round trip time delay defined as a function of Range of the target as a function of position (R(X)) and speed of light (c).

$$t_0 = 2R(X)/c$$

The range to the target can be calculated as a function of the platform position and height above ground. Assuming the aircraft is flying with constant velocity at a height (H(X)) above ground and images a point target from different positions (X) along the path. Ideally H is a constant since aircraft travels in a straight line, but height varies with X for non-linear trajectories which is the case practically. Nadir position being the center, range becomes a function of height and aircraft position (can employ simple Pythagorean Theorem to estimate) as

$$R(X) = \sqrt{X^2 + H(X)^2}$$

H(X) is not constant throughout the aircraft position and varies within a few meters. Such small variations in height would not make any difference in constructing the matched filter which is

explained in detail in section 4.6. However for our matched filter construction, it is assumed that the height is constant and non-linearities are handled by the multilooking. Hence matched filter is constructed at the range distance from the point of closest approach between aircraft and target i.e., nadir.

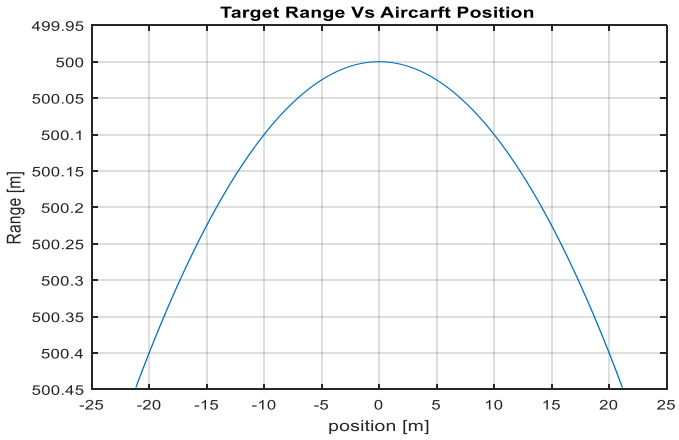

Figure 4:1: Function of Range (R) Vs Aircraft position (X)

Figure 4.1 shows that range of the target follows a hyperbola path along the aircraft position. When the target is approaching the target range decreases and as the aircraft moves away from the target, range increases having the minimum range at the nadir (vertex at nadir).

The received RF chirp is multiplied with the conjugate of transmitted chirp to obtain the IF signal which is defined as

$$S_{IF}(t) = \cos(2\pi f_0 t_0 + 2\pi k t_0 t - \pi k {t_0}^2)$$

The above IF signal equation is used at each antenna position to generate simulated IF data. The simulated IF data is similar to the actual radar data received without any noise and is processed similar to radar data as mentioned in signal processing section of chapter 3. The above mentioned IF signal can also be written as

$$S_{IF}(t) = e^{j\left(2\pi f_0 t_0 + 2\pi k t_0 \mathrm{t} - \pi k t_0^2\right)}$$

Now taking the FFT as $F(w) = \int_{-\alpha}^{\alpha} f(x) e^{-jwx}\, dx$

$$S_{IF}(w) = \int_{-\alpha}^{\alpha} S_{IF}(t) e^{-jwt}\, dt$$

$$S_{IF}(w) = \int_{-\alpha}^{\alpha} \left(e^{j\left(2\pi f_0 t_0 + 2\pi k t_0 \mathrm{t} - \pi k t_0^2\right)}\right) e^{-jwt}\, dt$$

$$= e^{j\left(2\pi f_0 t_0 - \pi k t_0^2\right)} \int_{-\alpha}^{\alpha} e^{j2\pi k t_0 t} . e^{-jwt} dt$$

$$= e^{j((2\pi f_0 t_0 - \pi k t_0^2)} . \frac{2\pi}{2\pi \int_{-\alpha}^{\alpha} e^{-jt\,(w - 2\pi k t_0)}\, dt}$$

Since we have $\frac{1}{2\pi} \int_{-\infty}^{+\infty} e^{-ik\,(y-x)}\, dk = \delta(y - x)$

$$S_{IF}(w) = e^{j\left(2\pi f_0 t_0 - \pi k t_0^2\right)} . 2\pi . \delta(w - 2\pi k t_0)$$

$\delta(w - 2\pi k t_0)$ is an impulse function at $f = k t_0$

Thus for the infinite bandwidth case, the FFT goes to an impulse at f = kt_0 with an associated phase of $e^{j\left(2\pi f_0 t_0 - \pi k t_0^2\right)}$. And for the impulse, SAR processing which is essentially an integration over that impulse results in sampling.

The data thus processed using the basic signal processing steps is shown in figure 4.2 and it can be seen how the echo from a point target is dispersed in several range lines at different sampling points in azimuth direction.

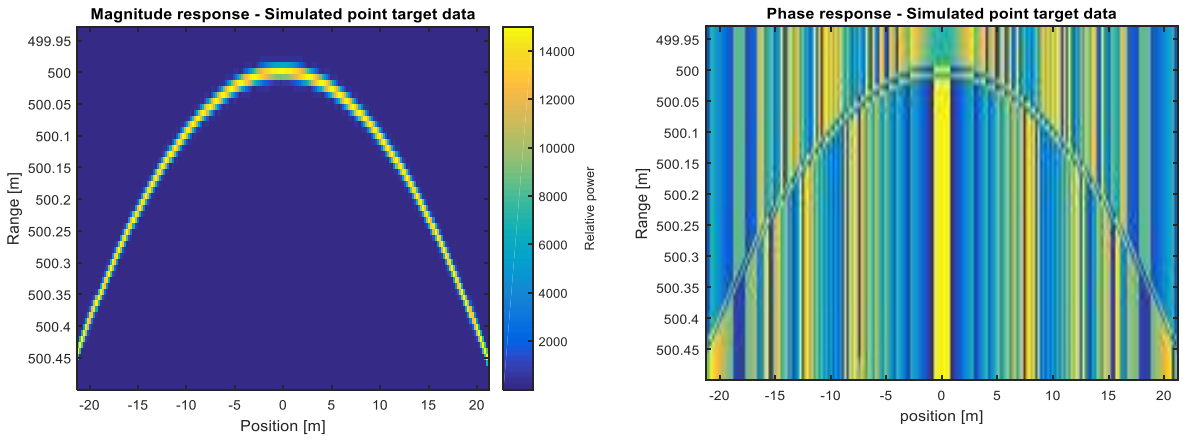

Figure 4:2: Magnitude and phase plots of simulated point data

The phase of the echo at each range line differs by an amount of $e^{j\,2\pi\,f0\,t0}$ in the equation of $S_{IF}(t)$. Now with SAR processing, the phases of the signal are corrected and then integrated coherently to focus the energy into a single point target.

4.1.2 SAR Technique

The time domain correlation SAR process in nut shell is depicted below in figure 4.3.

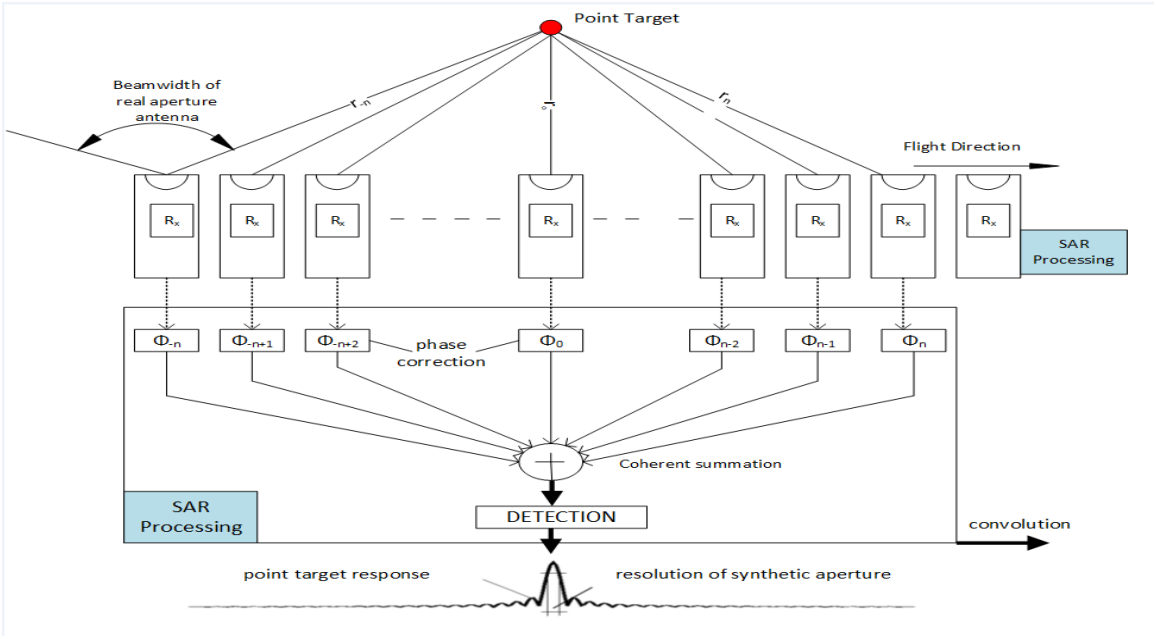

Figure 4:3: Time domain correlation method SAR processing steps

The phase correction and coherent summation is done with matched filter in our algorithm. The ideal simulated data is used as a matched filter for our SAR processing. Thus essentially, this is a matched filter application.

Now to validate the SAR processing technique, matched filter is applied on the simulated point target data to ensure

i. If the phases are cancelled out when the simulated point target data is multiplied with the matched filter
ii. And, theoretically when SAR processed, it should give a SNR improvement by a factor of 2 (3 dB) or a signal power improvement by a factor of 4 (6 dB) whenever the SAR aperture length is doubled. So now noise free simulated data should give the same results as expected theoretically.

For visualizing both magnitude and phase in a single image, RGB plots of the data are obtained by mapping the magnitude of the data into intensity and the phase of the data into hue. The below figure 4.4 shows the RGB plots of simulated point target, matched filter and product of simulated point target data with the conjugate of matched filter. Fig. 4.5 also shows the phase plot of the simulated data, the matched filter and the product of simulated data and the conjugate of mathced filter at 500 m range. It is clearly visible that from the figures 4.4 and 4.5 that on multiplication with the matched filter, the phases are corrected and has a constant phase throughout the rangelines.

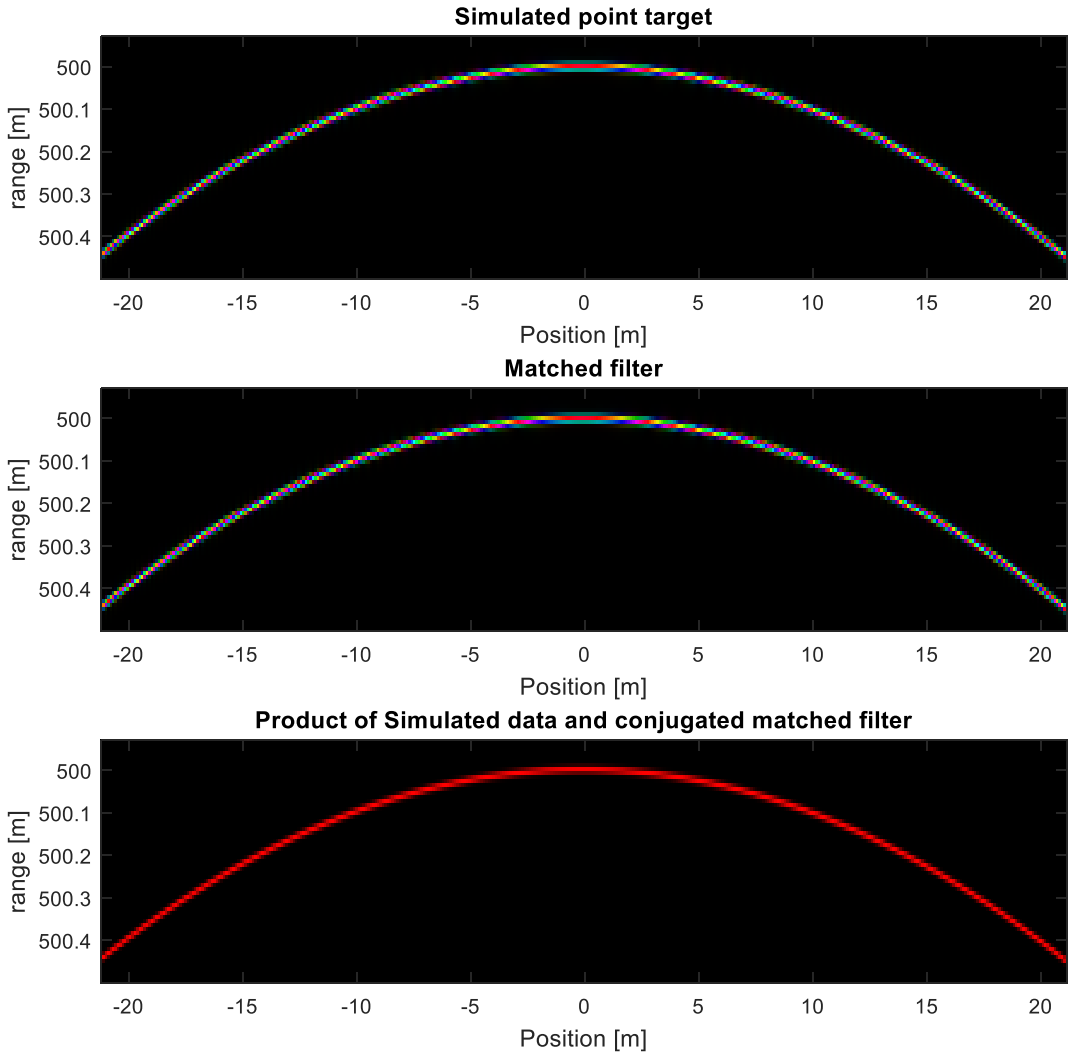

Figure 4:4: RGB plots of simulated point target, matched filter and product of simulated and conjugated matched filter.

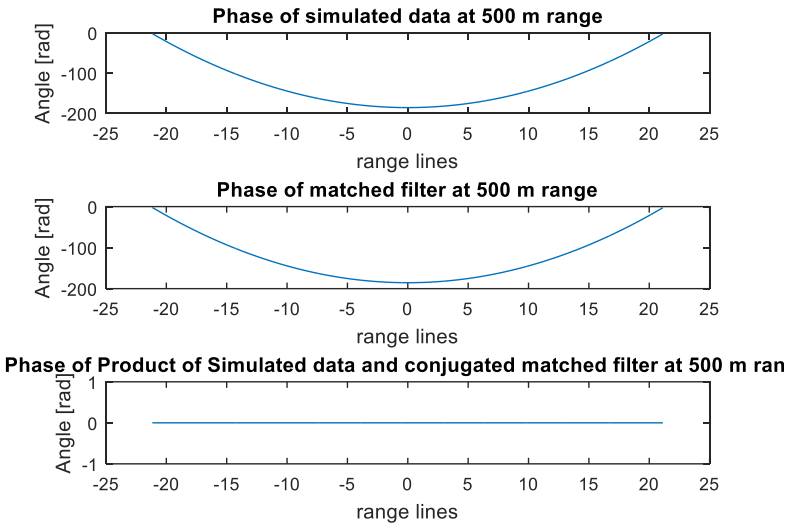

Figure 4:5: Phase plots of simulated, matched filter and product of both at 500 m range.

Now to check for the signal and SNR improvement, the simulated point target is SAR processed with different aperture lengths of 10, 20, 40, 80, and 160 range lines and the results are shown below in fig. 4.6.

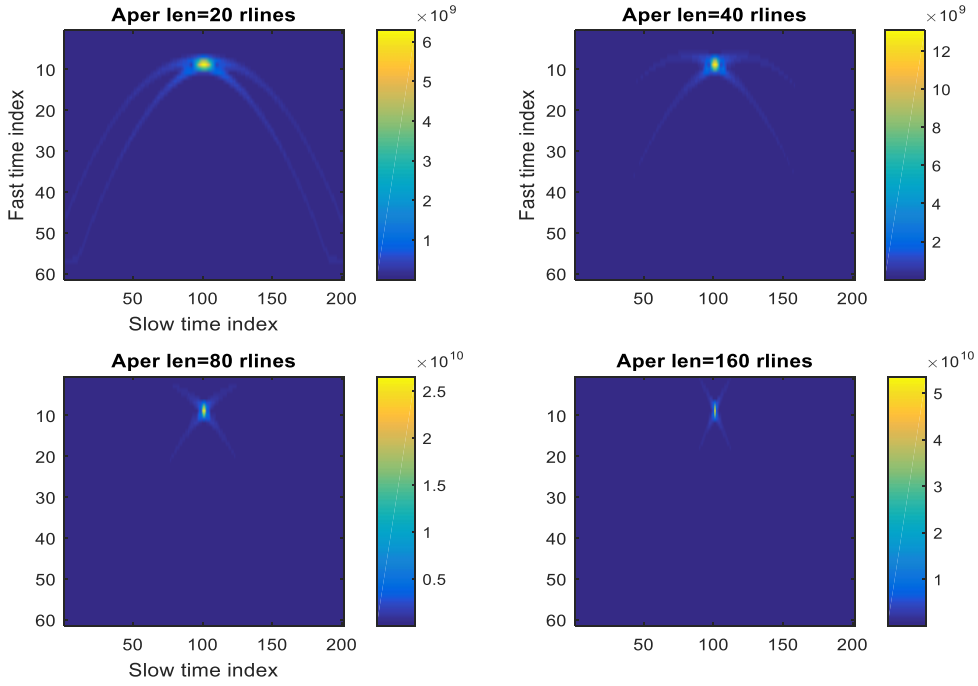

Figure 4:6: SAR processed simulated point target data for different aperture lengths.

Figure 4.7 shows the signal power improvement and the SNR imrovement over the aperture length. The signal improvement improvement of 6 dB is shown for doubling the aperture length and the SNR is imrpoved by a factor of 2 (3 dB) as the aperture length doubles. SNR of the data is measured with signal power as the peak power of the target echo and the noise power as variance of the absolute values of the noise floor.

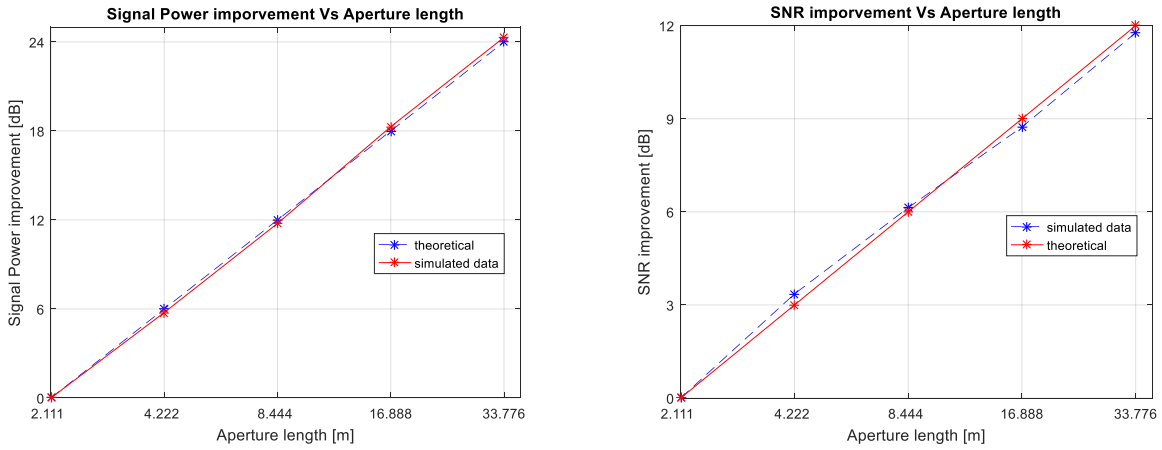

Figure 4:7: Signal Power improvement and SNR improvement for increasing aperture lengths

The A-scopes across the simulated point target in along-track dimension are shown below in figures 4.8 and 4.9.

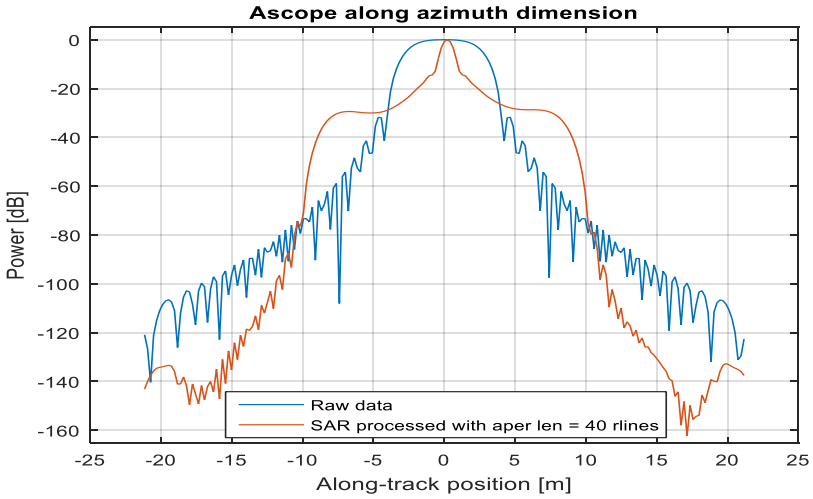

Figure 4:8: Ascope comparison of raw and SAR processed data in along-track dimension

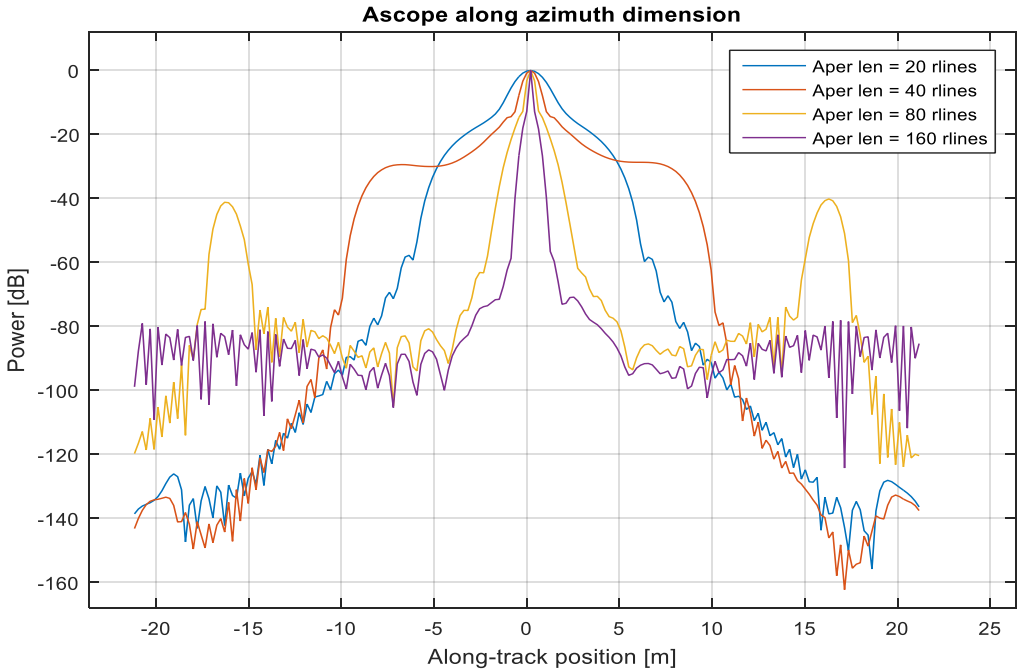

Figure 4:9: Ascope comparison for different aperture lengths in along-track dimension

It is observed that as the antenna beamwidth increases (aperture length increases), the azimuth resolution is better by almost twice in accordance with the theoretical value. This can be seen with the -3 dB values in the below table 5.

Table 5: -3dB resolutions along azimuth direction for increasing aperture lengths

Aperture length in range lines	***Azimuth resolution (m) [simulated data]***	***Azimuth resolution (m) [theoretical, fc=10 GHz]***	***Azimuth resolution (m) [theoretical, fc=18 GHz]***
Raw data	4.689	53.2	27.04
20 [4.2 m]	1.554	3.55	1.71
40 [8.4 m]	0.781	1.77	0.89
80 [16.9 m]	0.391	0.89	0.44
160 [33.8 m]	0.092	0.44	0.22

Now that the time domain correlation SAR technique is verified, this is used in our further studies and results when applied to point target data and real time data are presented in the next chapter.

4.2 Mismatched filter range SAR application:

From figures 4.4 and 4.5, we can see that the phase is perfectly compensated all through the aperture length when matched filter and point target are at same range. We have now simulated the point target at 500 m range and matched filter at 510 m range to see how this difference in range will affect the SAR performance. The RGB plots of the point target, matched filter and the product of point target and the conjugated match filter is shown in fig. 4.10. The phase is constant only up to 27.6 m azimuth distance and it was 42 m for perfectly matched range. The phases of point target at 500 m, matched filter at 510 m, and the product is shown in fig. 4.11. The phase of the product has small variations and is not a straight line unlike in fig. 4.5.

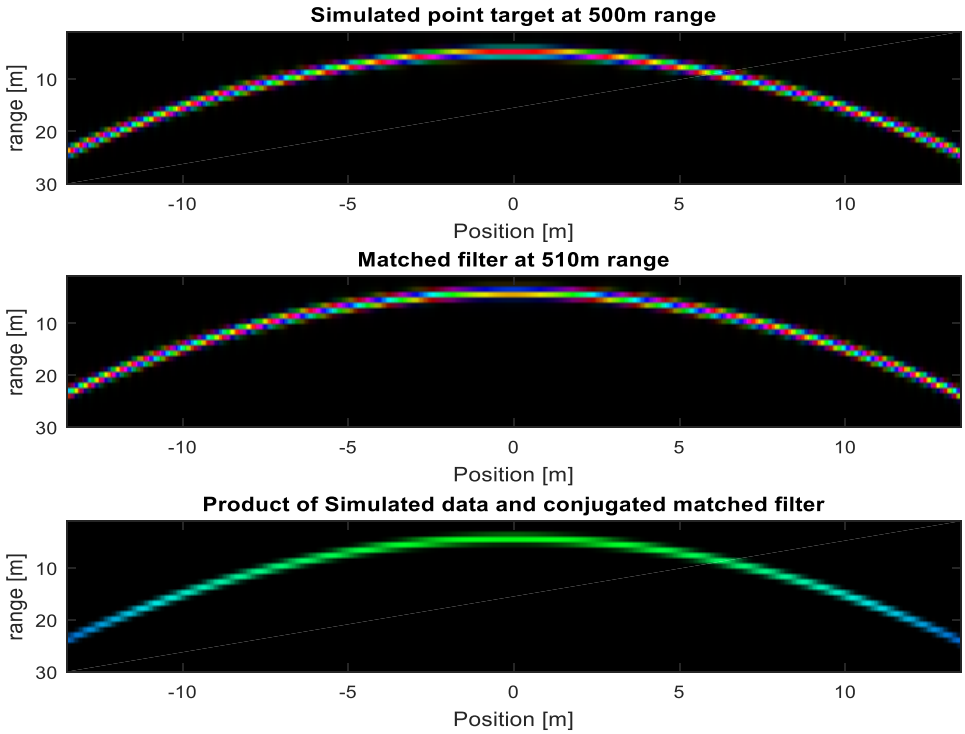

Figure 4:10: RGB plots of point target, matched filter with mismatched range and the product of both

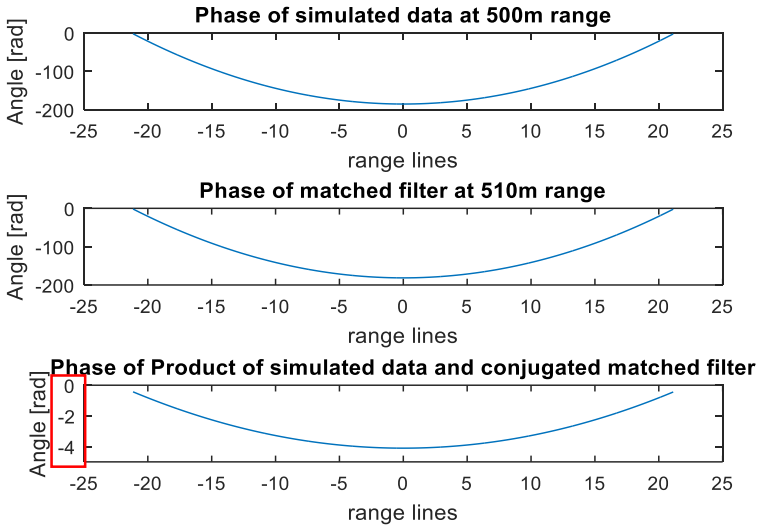

Figure 4:11: Phase plots of point target at 500m, matched filter at 510 m and the product of both.

We have generated point target data at 500 m range and constructed matched filters with different ranges from 470 m to 530 m. Aperture lengths which would give less than ±90 degree phase change are considered as the maximum synthetic aperture lengths. Below fig. 4.12 shows the maximum aperture length that can be considered for different ranges of matched filter with point target data at 500m. To obtain perfect maximum attainable aperture length, matched filter range can have a variation of ±2 m. However, for the field data, the maximum synthetic aperture length that can be considered is less than the maximum attainable due to several reasons. Considering it can't be more than 25 m based on field data sets examined, the filter range can have a variation of ±10 m.

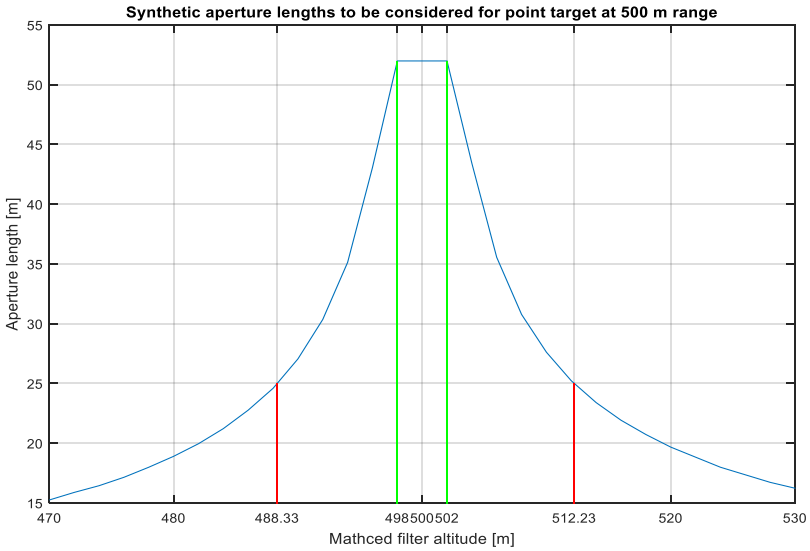

Figure 4:12: Maximum synthetic aperture length that can be considered for different mismatched range values of point target and matched filter

4.3 Altitude Vs SAR Processing

With all the developments we are able to map the snow surfaces with high resolution, but there are many regions that are being left unmapped. One solution to this would be reducing the antenna length to provide larger swath but then we must compromise with the azimuth resolution. This brings us to a consideration where both swath width and resolution are increased. And hence higher altitude remote sensing is gaining importance these days because they can provide large swath width with small antennas. These are also useful for the areas which require frequent monitoring. We have previously seen that the SAR performance varies with the beamwidth over which it is processed. And it must be especially taken care of for higher altitude data since the radar has a large fooprint at higher altitudes. This concept is explained here with simulated data at different altitudes. We have simulated the radar data with same parameters and at altitudes of 500 m, 1000 m, and 2000 m and also generated corresponding matched filters. Fig. 4.13 shows the SAR processing results for simulated data and matched filters mentioned above. It can be observed from the figure that double the altitudes require double the synthetic apeture length to achieve the same

azimuth resoltuion. This is when the flight trajectory is ideally linear and the phases are all cancelled out throughtout the footprint after SAR processing for all cases.

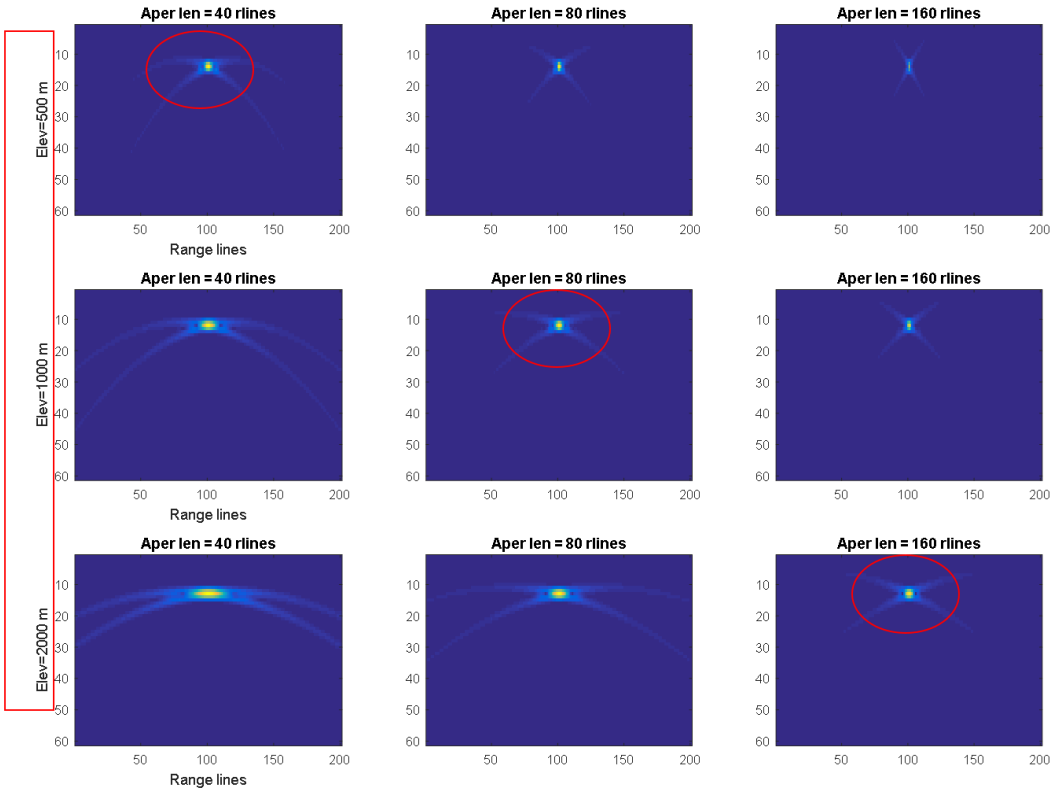

Figure 4:13: SAR processing results for data obtained at 500m, 1000m, and 2000m with different aperture lengths.

4.4 Aircraft non-linearities

When imaging the scene with the radar, the aircraft path does not follow a linear trajectory and has some low frequency non-linearities which might cause distortions in the SAR images. With TDC SAR method, these non-linearities are handled unlike frequency domain SAR techniques. Trjaectory non-linearities and how it affects SAR images is shown here. For simulations, these trajectory errors are described in terms of Root Mean Square Error (RMSE) and correlation length which determine the roughness of the path vetically and horizontally. Studying the real data collected by snow radar in various seasons, on an average the aircraft trajectories has RMSE values

around 1 m (0.6 m – 2 m mostly) and dynamic range of elevation less than 7 m (0.3 – 7 m) for an along-track distance of 4 km on an average, correlation factor between 0.1 and 0.3 for an aircraft altitude of 500 m and the errors are generally less for higher altitudes.

To see the effects of these trajectory non-linearities, let us simulate some data with random non-linear trajectory path with the above mentioned errors levels. Fig. 4.14 shown below shows the random non-linear trajectory created and the associated range on the left and the phase plots of simulated data, matched filter and the product of data and conjugated matched filter at 500 m range. It can be observed that the phase of the product takes the shape of the trajectory and from a set of simulations, it is seen that the phase deviation in radians is $1/4^{th}$ times height deviation in m. It can be seen that the phase do not cancel out as in ideal trajectory case of Fig. 4.5. Fig. 4.15 shows the SAR processed images for the non-linear trajectory for different aperture lengths and it is observed that distortions arise as the aperture length increases.

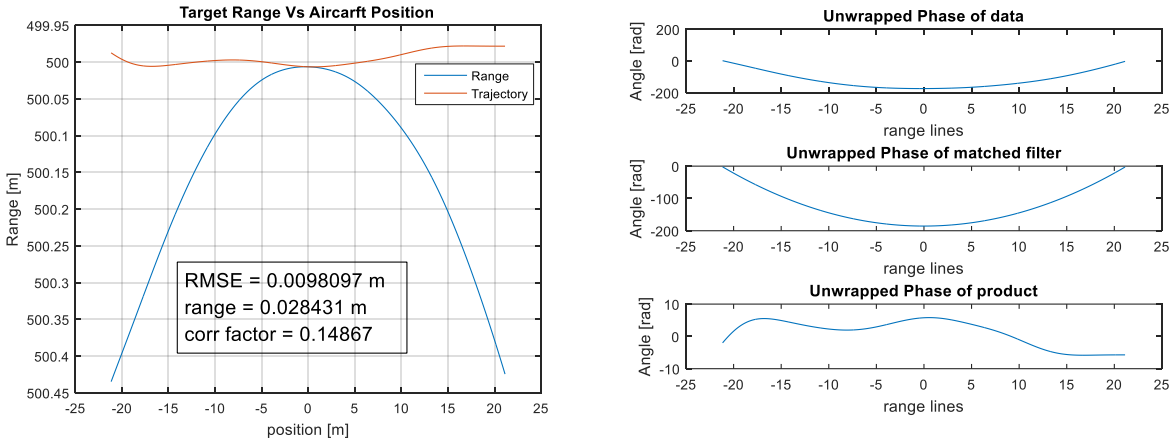

Figure 4:14: left: Non-linear trajectory and the associated range; right: Phase plots at 500 m range

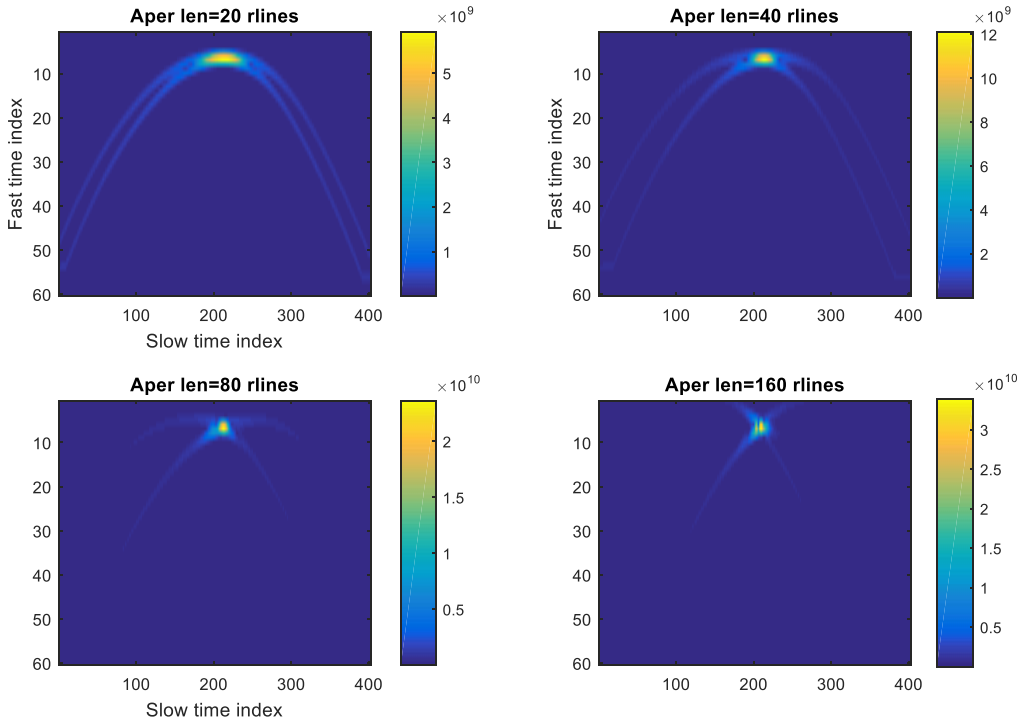

Figure 4:15: SAR processed images for the non-linear trajectory shown in left of fig. 4.13

Fig. 4.16 shows the signal power improvement plot for 50 randomly generated non-linear trajectories with the random input values of RMSE, dynamic range of trajectory and correlation length. Clearly the improvement doesn't coincide with the theoretical values as in ideal trajectory case. As the aperture length increases, the more non-linear the aircraft path is, and it affects the SAR image. The minimum, maximum and the mean parameters generated by Monte Carlo simulations are listed below in table 6.

Table 6: RMSE, Dynamic range and correlation length of Monte Carlo simulations

	RMSE	**Dynamic range (cm)**	**Correlation length**
Minimum	0.3531	0.9960	0.0874
Maximum	3.0074	8.5189	0.2325
Mean	1.2647	3.9911	0.1568

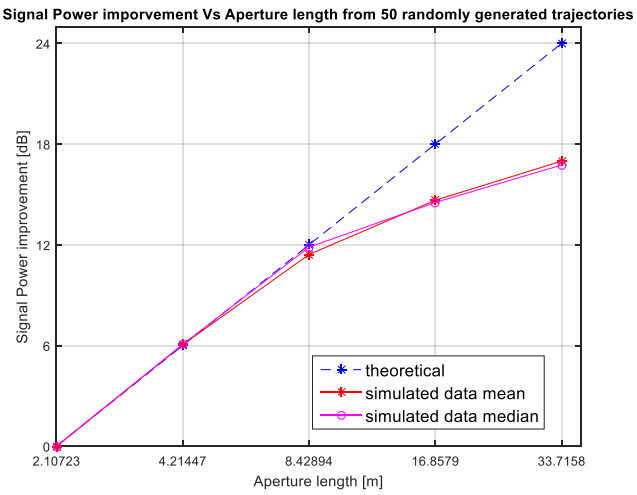

Figure 4:16: Signal Power improvement with mean and median of 50 randomly generated non-linear trajectories.

For a particular value of RMSE, signal power decreases as the correlation length decreases. This is shown in below plot from fig. 4.17. For RMSE values of 0.63 cm and 0.68 cm, for increasing correlation lengths, signal power reduced.

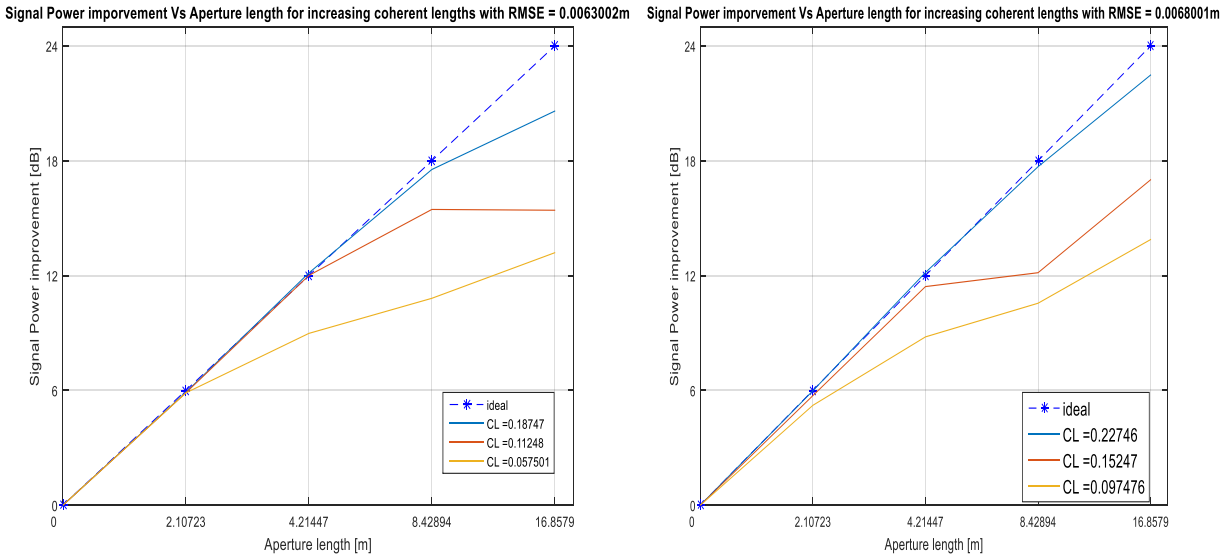

Figure 4:17: Signal improvement for different correlation lengths for RMSE value of 0.63 cm on the left and 0.68 cm on the right

Also, for a particular value of correlation length, signal power decreases as the RMSE value increases. Fig. 4.18 shows the signal decrement for increasing RMSE values and a fixed value of correlation factor of 0.1275. With this information, we can decide on the optimum aperture length

that can be considered based on the RMSE and the correlation length of the aircraft trajectory for that data set.

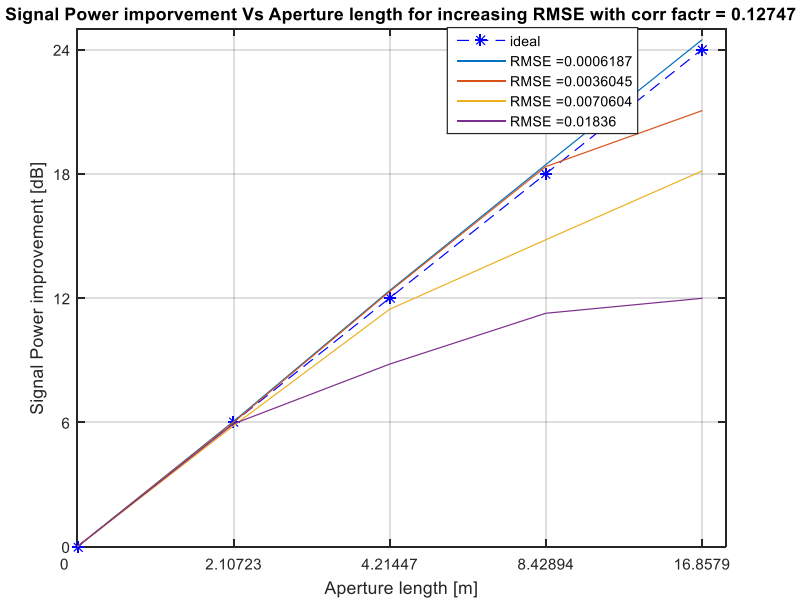

Figure 4:18: Signal improvement for different RMSE values and a fixed correlation length of 0.1275

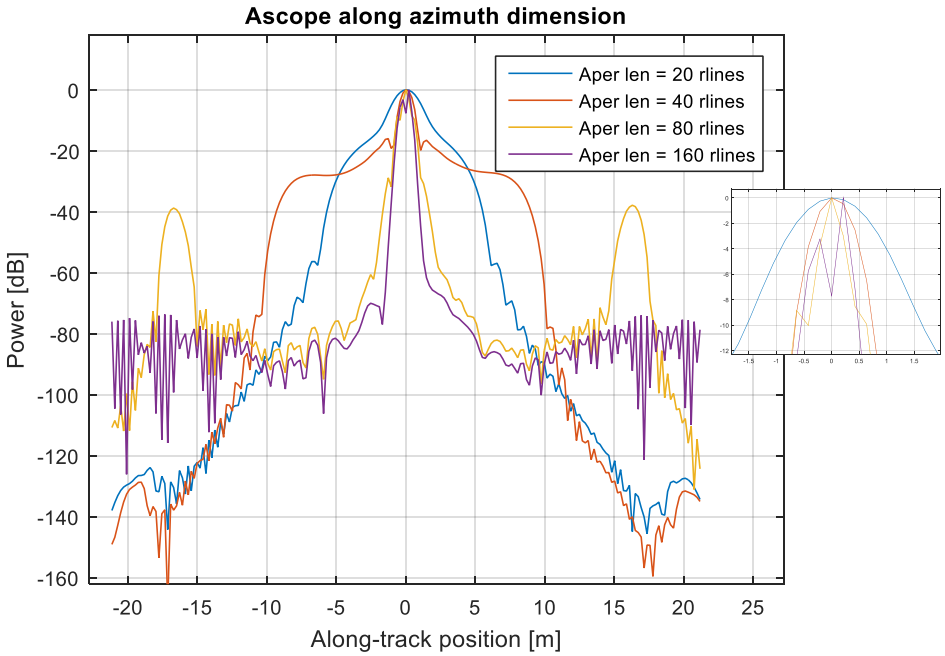

Figure 4:19: Ascope resolution of non-linear flight data

Fig. 4.19 above shows the Ascopes along azimuth directions and it can be seen that aperture length of 160 range lines has almost equal resolution as of 80 range lines unlike in ideal case shown in fig. 4.9. And also the target is focused right into the center. The -3dB resolutions for 20, 40, 80 and 160 range lines are 1.5755m, 0.7837m, 0.3757m, and 0.4190m respectively.

Also, when the radar echoes are processed coherently, the relative phases undergo constructive and destructive interference increasing the variance of the echoes which increase the speckle noise of the SAR image. This speckle noise is multiplicative and multiplies as the aperture length increases. Presence of speckle in echograms reduces the ability to distinguish objects of different scattering properties. This means the radiometric resolution, a term to quantify ability to distinguish between uniformly distributed targets with different scattering properties is increased. Speckle is generally removed by averaging images from different signal spectrum. To address both the problems speckle noise and aircraft non-linearities, "Multilook SAR" processing which is described in section 4.6 is employed.

4.5 Non-linearities Vs Altitude

We have already seen that when the flight path is non-linear, there are distortions in the SAR processing results. This concept becomes particularly crucial when studying data at different altitudes. In this section, we try to study how non-linearities in the path trajectory influence the SAR result at various altitudes and what are the factors that influence the distortion.

Fig. 4.20 shows the non-linear paths considered at different altitudes with some random RMSE values and correlation lengths.

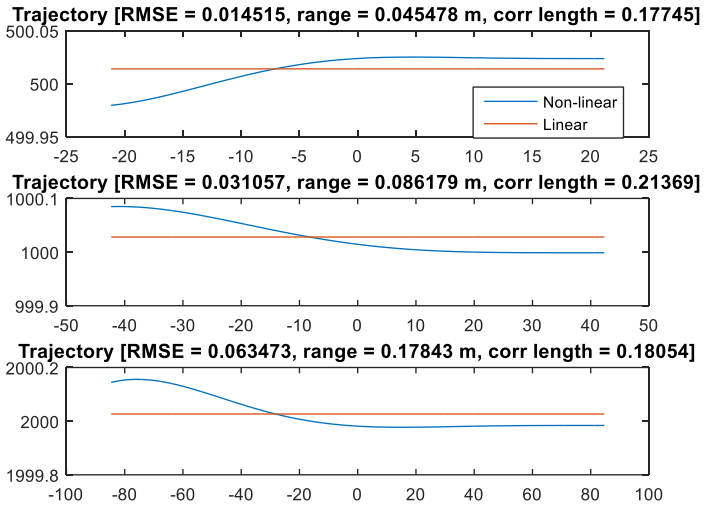

Figure 4:20: Non-linear paths for different altitudes

Fig. 4.21 shows the SAR processed result for the above taken data. As evident, the distortion is inversely proportional to the correlation lengths as greater correlation lengths indicate smoother trajectories and directly proportional to the RMSE since the non-linearity is less when RMSE is less. Fig. 4.22 shows the signal improvement for different altitude cases from an average of 50 random cases and the mean RMSE and correlation length values are as shown in below table 7 and it can be said from the values that the data at 500 m undergoes more distortion.

Table 7: RMSE ad Correlation lengths for various altitude data

Parameter\Altitude	**500 m**	**1000 m**	**2000 m**
RMSE	0.1425	0.2374	0.1931
Correlation length	0.1168	0.2330	0.1735

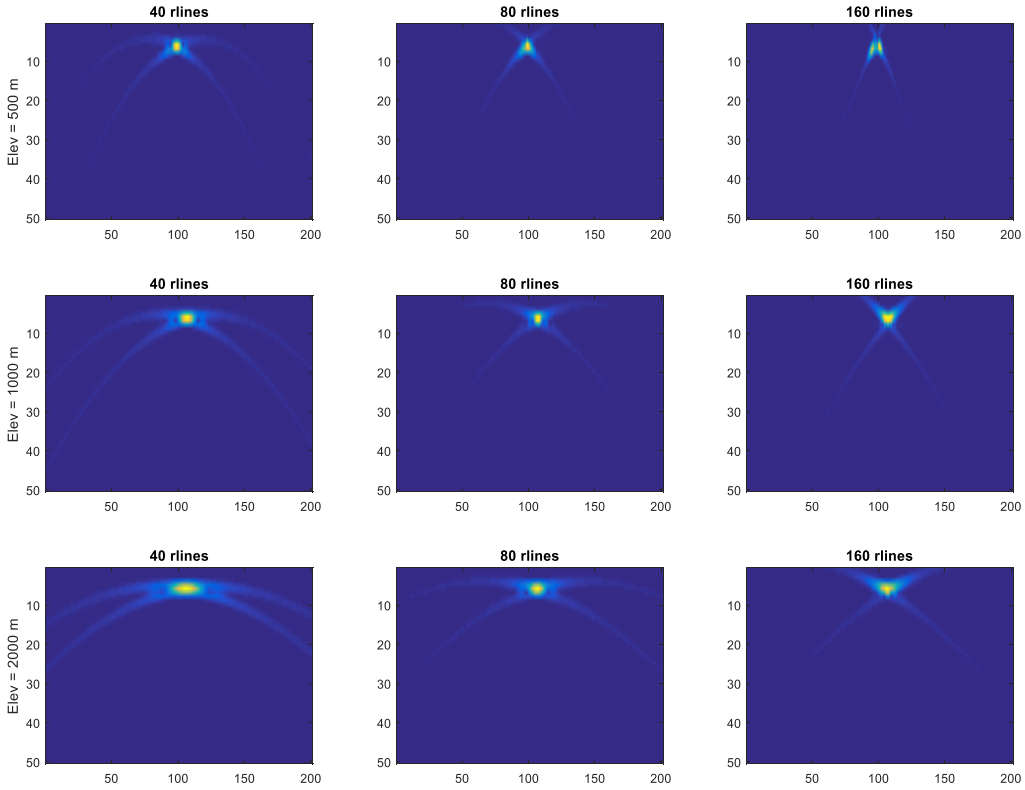

Figure 4:21: SAR processed images for non-linear trajectory data at different altitudes

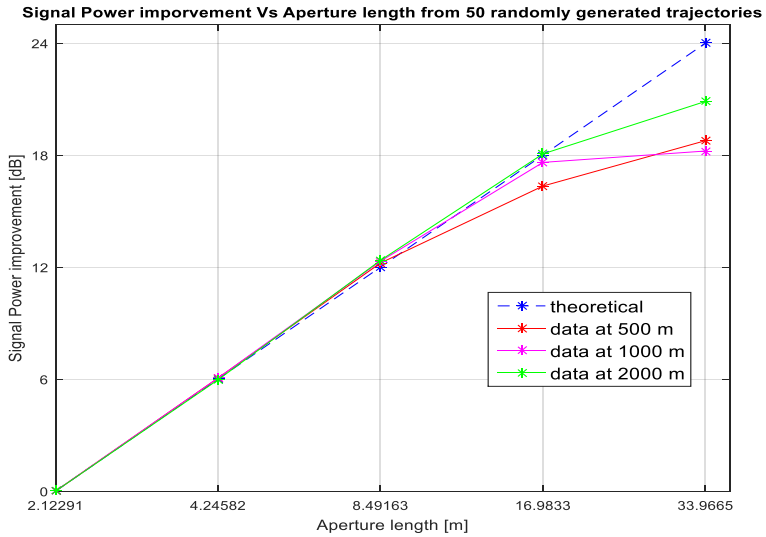

Figure 4:22: Signal Improvement for non-linear trajectories at different altitudes

4.6 Multilook SAR

In multilook SAR processing, the entire synthesized aperture is divided into several sub-apertures so that the non-linearity within the smaller sub aperture is negligible when compared to the non-linearity of the entire aperture. The same return taregt data is SAR processed multiple times with these sub-apertures and then averaged incoherently and hence the name “Multilook SAR processing”.

Here, the matched filter is divided into N fragements in the along-track dimension. Each of these fragment is windowed individually to reduce the side-lobes and is now time correlated with the radar data by convolution to generate a “look”. The output of this process is N data sets that are SAR processed with N fragements of the matched filter. These N looks are incoherently averaged to produce a final image. This way the sensitivity to the non-linear path is reduced as the entire path is processed several times and averaged and also the radiometric resolution is improved. However this process degrades the azimuth resolution of the processed image since a samller aperture length is used to generate the looks. This concept is explained pictorially in fig. 4.23.

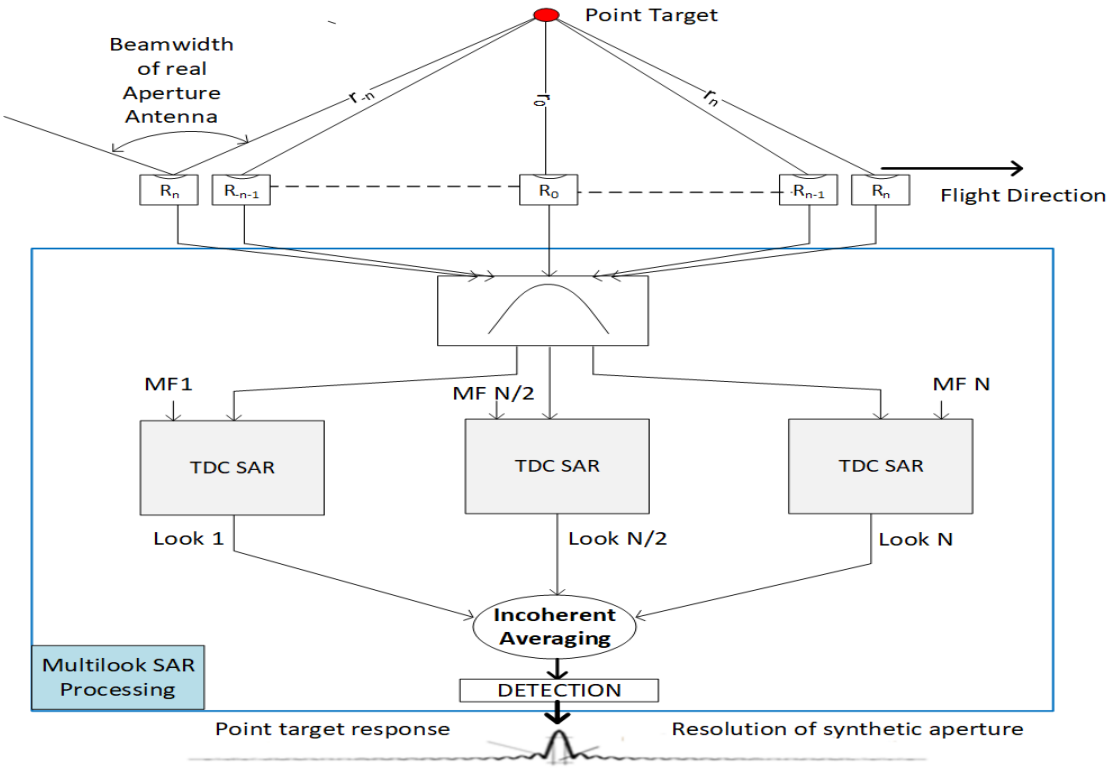

Figure 4:23 Graphical representation of Multilook SAR processing with no overlap

The radiometric resoltuion is defined as [42]

$$\gamma = 10\ log10\ (1 + \frac{\sigma}{\mu})$$

Where σ and μ is the standard deviation and mean of the target intensity values. The standard deviation of the speckle with N looks is now reduced [43] by $1/\sqrt{N}$ i.e.,

$$\sigma = \frac{\sigma}{\sqrt{N}}$$

And hence the radiometric resolution is decreased. But the azimuth resoltuion increases by a factor of N as the apeture length decreases by that amount.Azimuth resolution as a function of aperture length and number of looks become

$$\Delta z = \frac{\lambda}{L_s} N$$

Where L_s is the synthetic aperture length and λ is the wavelength.

So the number of looks is chosen to compromise between rediometric and azimuth resolution. The looks are overlapped usually by 40% to 60% [44].

For some non-linear path, Multilook SAR process with 40% overlap is applied for aperture lengths of 80 and 160 range lines and the final images are shown below in figures 4.24 and 4.25. It can be seent that Multilooked images with looks =2 gave better results. And as the looks increase the resolution is degraded and hence an optimum number of looks must be choosen.

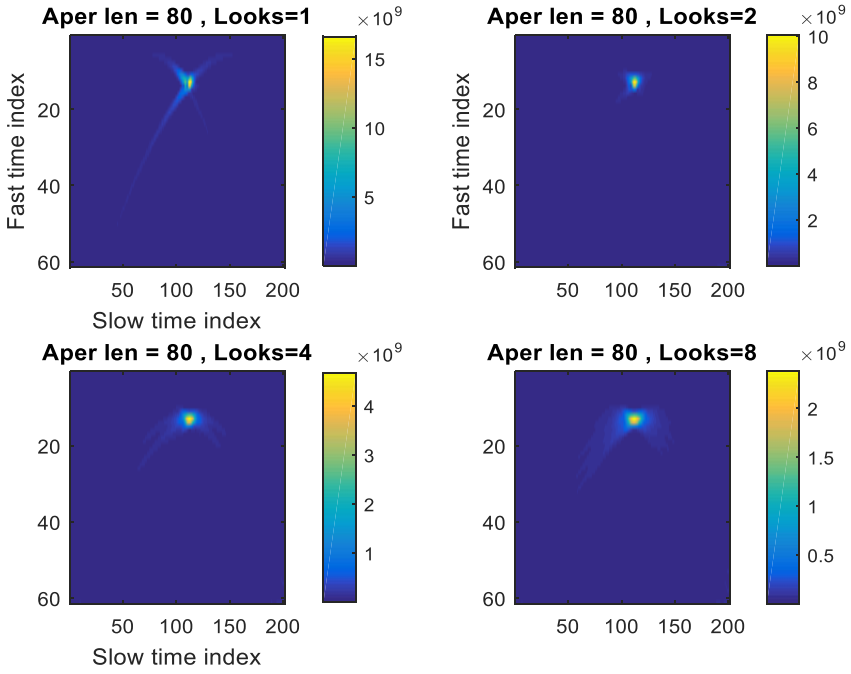

Figure 4:24: SAR processed and Multilooked simulated target data for Aperture length of 80 range lines

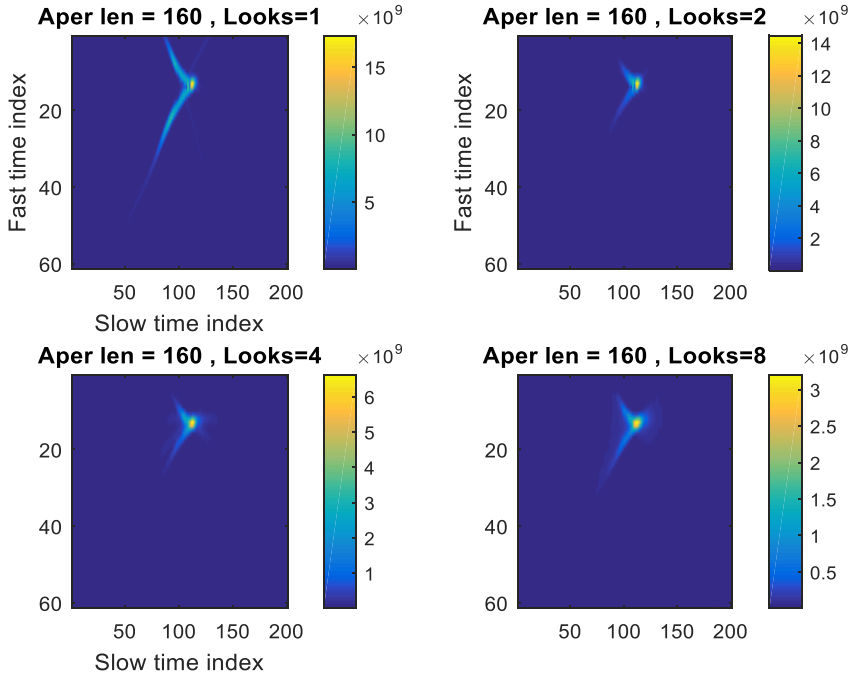

Figure 4:25: SAR processed and Multilooked simulated target data for Aperture length of 160 range lines

5 RESULTS AND COMPARISONS

We have seen the SAR and Multilook processing techniques and how the results vary for different parameters like the frequency of operation, altitude, etc. In this chapter, we will see some of the SAR processing results for simulated data, point target data, real filed data and also compare some low and high-altitude data.

5.1 Point target data

The point target data was taken from the test flight data in 2017 Greenland_P3 season for OIB mission. The data was recorded with the single channel 2-18 GHz waveform and a hyperbola where the return signal is strong is considered as the point target data instead of a corner reflector data. The magnitude and phase plots of the point target data are shown in fig. 5.1 along with matched filter plots in fig. 5.2.

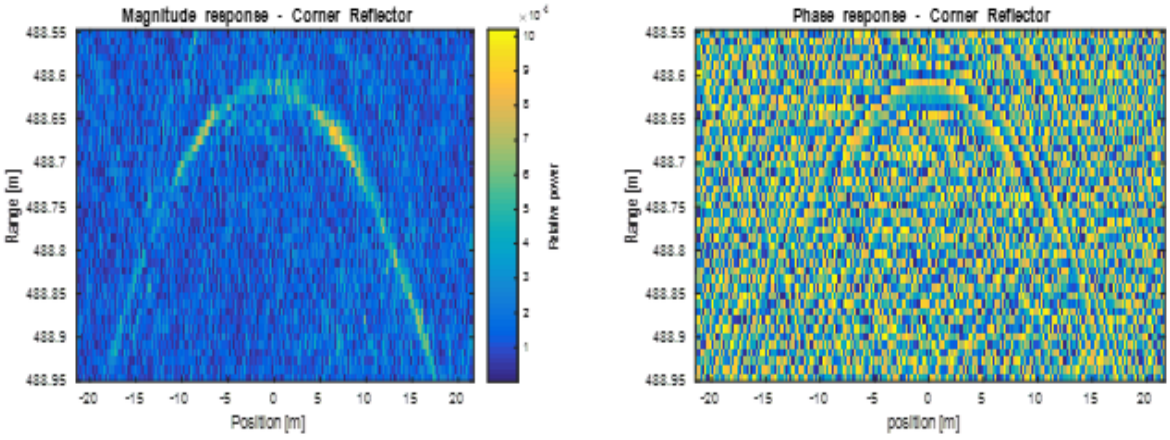

Figure 5:1: Magnitude and phase plots of point target data

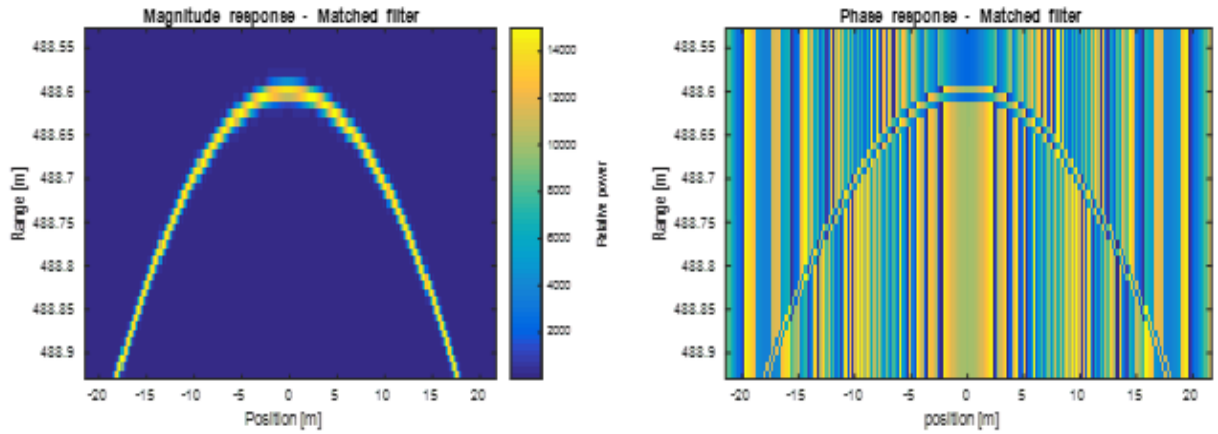

Figure 5:2: Magnitude and phase plots of matched filter (ideal simulated data)

The phase plots of both the point target data and the simulated data are shown below in fig. 5.3 and they are similar. The phase plot after the point target data is multiplied with the matched filter is also shown and it is almost flat but not ideally as the case of simulated data. The RGB plots of point target, matched filter and the product of point target and the matched filter are also shown in fig. 5.4.

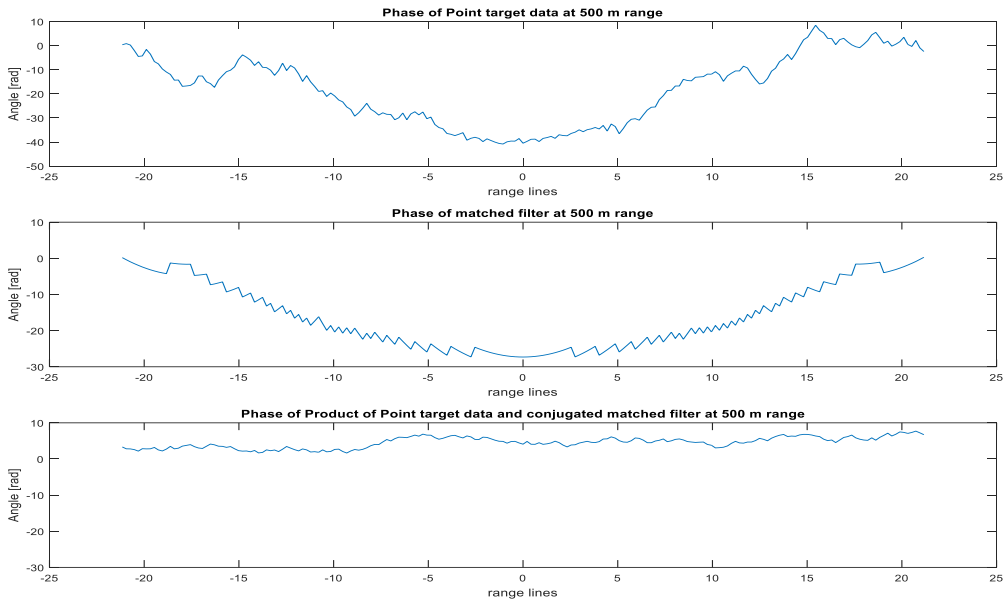

Figure 5:3: Phase plots of point target, matched filter, and product of both

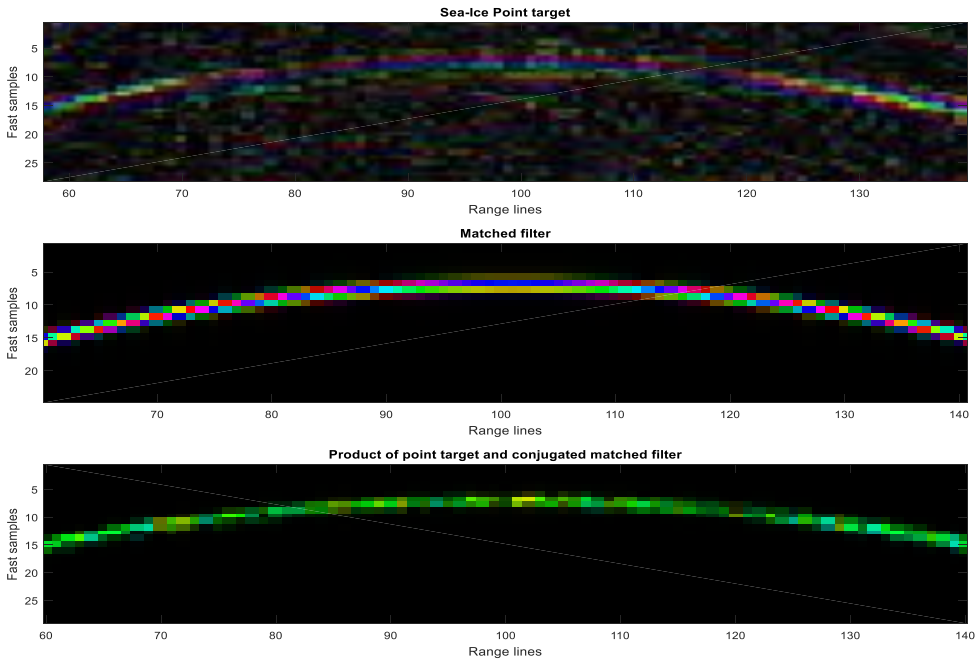

Figure 5:4: RGB plots of point target, matched filter, and product of both

This point target data is SAR processed for various aperture lengths and the results are shown in fig. 5.5. It can be seen from the figure that the SAR image is showing improvement for aperture lengths up to 80 range lines and then for aperture length of 160 range lines, signal strength is not greatly increased as expected to double (color bar). Also, the image quality or the azimuth resolution seems to be decreased. These factors can be shown elaborately through performance metric plots.

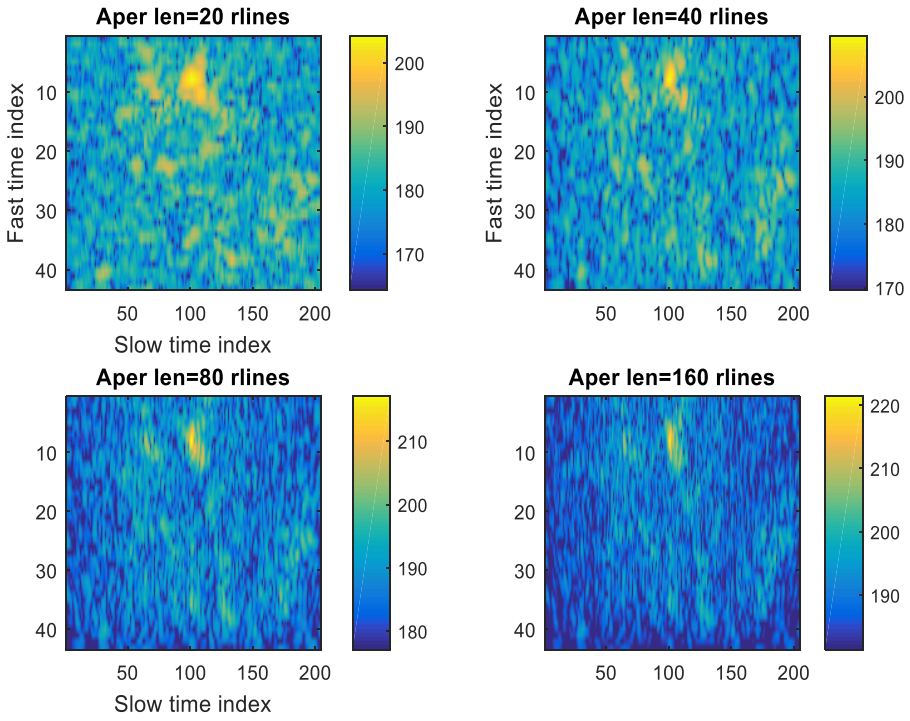

Figure 5:5: SAR processing result of point target data for various aperture lengths

The signal power improvement and the SNR plots are shown in fig. 5.6. From the signal strength plot, it is evident that the curve follows ideal plot up to 80 range lines and then improvement is not as expected. The SNR plot shows that the SNR value of the point target improves only a little after 80 range lines. This might be because of great increase of noise variance.

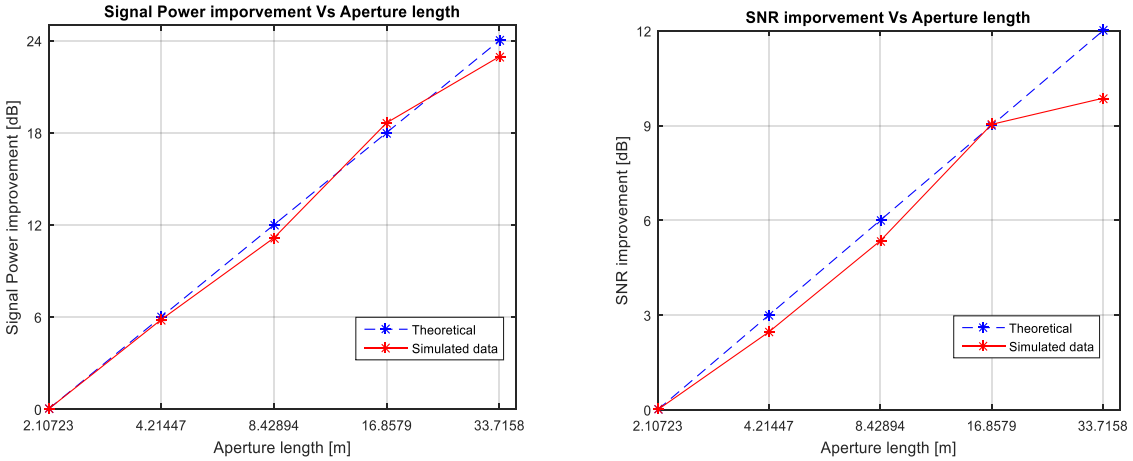

Figure 5:6: Signal Power Improvement and SNR improvement for point target data

To study how the noise is affected, noise variance is plotted in linear scale and log scale for these aperture lengths as shown in fig. 5.7. Since the noise is multiplicative, it is expected to double as the aperture length doubles and it is evident from the figure.

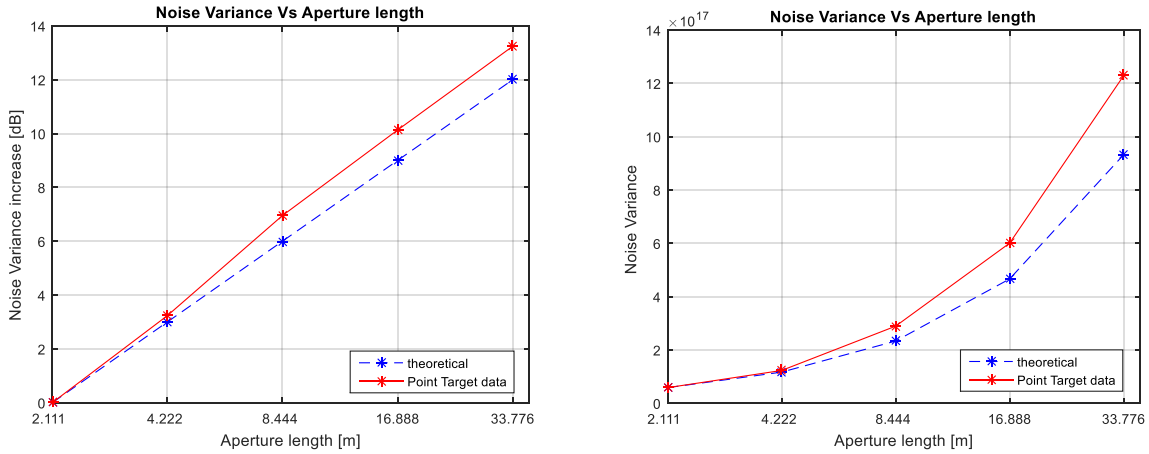

Figure 5:7: Noise variance plots in log scale and linear scale

The simulated data plot coincided with the ideal plot in signal power improvement because in the simulated case there is no limitation on the synthetic array length and can be taken as full travel distance travelled by the aircraft. In the real data case, there is a limitation in strip map SAR geometry on the length of the synthetic array being considered for SAR processing. This limitation arises by the fact that the region being images must be in the actual antenna beam as the aircraft moves horizontally. According to the geometry shown in fig. 5.8, the azimuth span of the actual antenna beam becomes [45]

$$L = r_n \, \theta_{ant}$$

$$L = \frac{r_n \, c}{L_{ant} \, fc \, \sqrt{\epsilon_r}}$$

Where r_n is the range at nadir; c is the speed of light; L_{ant} is the actual antenna length; fc is the center frequency in Hz; and ϵ_r is the refractive index. Substituting the values of the radar being

operated, we get the aperture length to be 53 m approximately which approximates to 190 range lines with an azimuth spacing of 0.2111 spacing in our case. The plot in fig. 5.6 shows that we can get the signal improvement as ideal case until 80 range lines which agrees with the above concept.

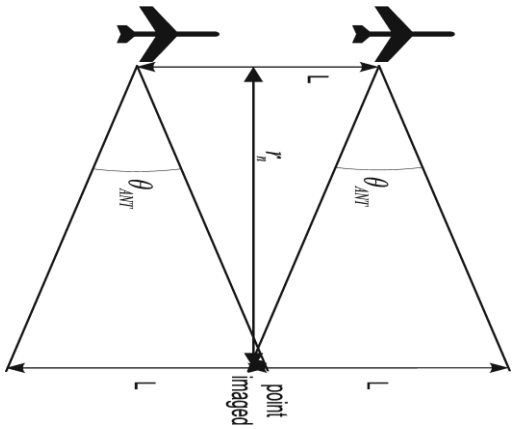

Figure 5:8: Synthetic aperture Radar geometry

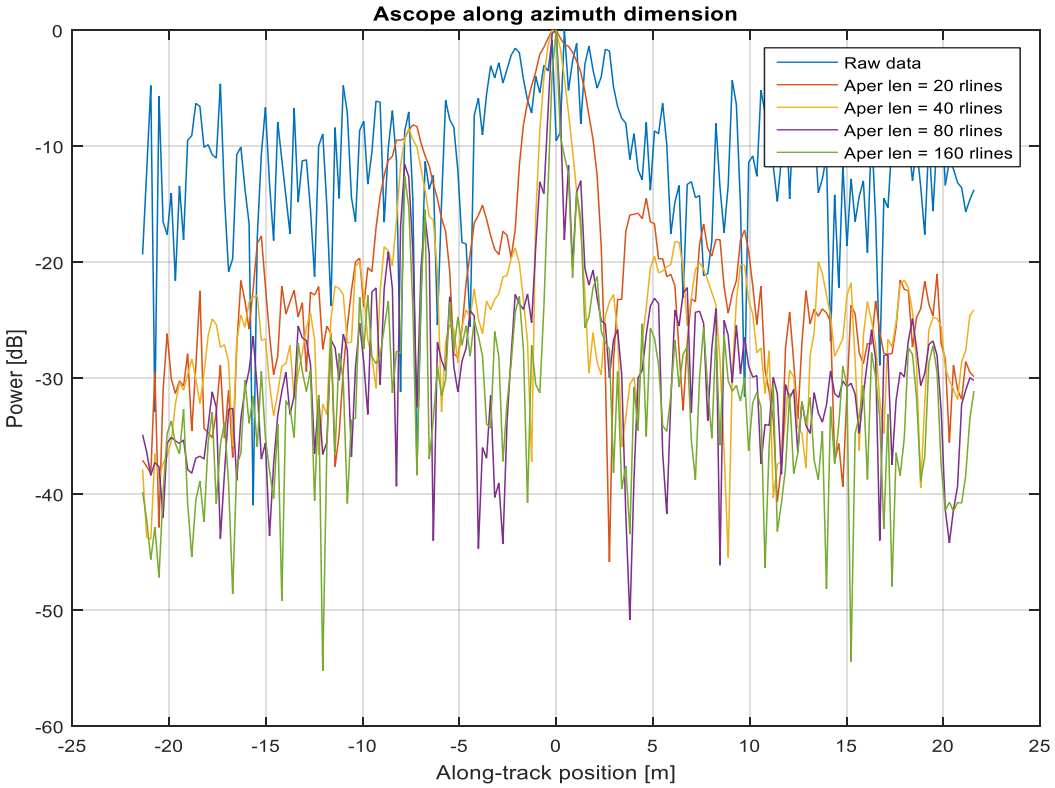

Figure 5:9: Ascope along azimuth dimension for various SAR parameters

The azimuth resolution values for the simulated data and the point target are mentioned in the below table 8.

Table 8: Comparison of Azimuth resolution of simulated point target and actual point target data

Aperture length in range lines [dx = 0.2111 m]	**Azimuth resolution (m) [Simulated]**	**azimuth resolution (m) [Point Target]**
Raw data	4.689	5.8283
20	1.554	2.1075
40	0.781	0.8825
80	0.391	0.3917
160	0.0920	0.2376

As seen earlier, the SNR did not improve as expected after 80 range lines, it is the same with azimuth resolution. The azimuth resolution values for simulated and point target data are varying. When the SAR length is taken more than the limited value, the performance of SAR is degraded. This effect is seen within the range of acceptable aperture lengths for this radar at 500 m height. This might be because of other attenuation effects the received signal strength decreases further at positions away from the nadir and the synthetic aperture length must be decreased further [42].

5.2 SAR processing results of field data

Now that the SAR processing technique is verified with both simulated and point target data, it is now applied to the collected field data by the snow radar. Several data sets are processed with various parameters like the SAR aperture length and the number of looks and the optimum parameters which give the best results in terms of SNR and the azimuth resolution for all the data has to be considered the optimum parameters.

The SAR processor is tested on sea-ice data collected on 10th March 2017 during the Greenland P3 mission over Laxon Line sea ice as shown in fig. 5.10. The radar operated over the entire snow radar's bandwidth of 2-18 GHz frequency at 500 m altitude. The SAR processed results rae shown from fig 5.11 to 5.15.

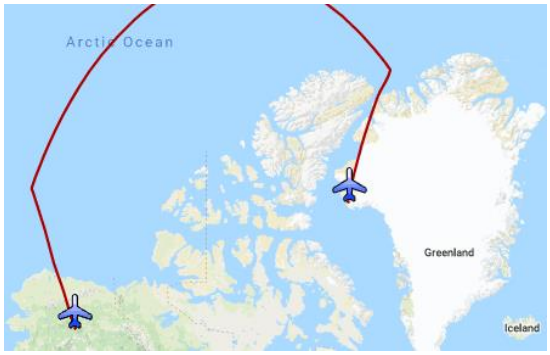

Figure 5:10: Flight line on March 10th over Laxon Line from Greenland P3 mission.

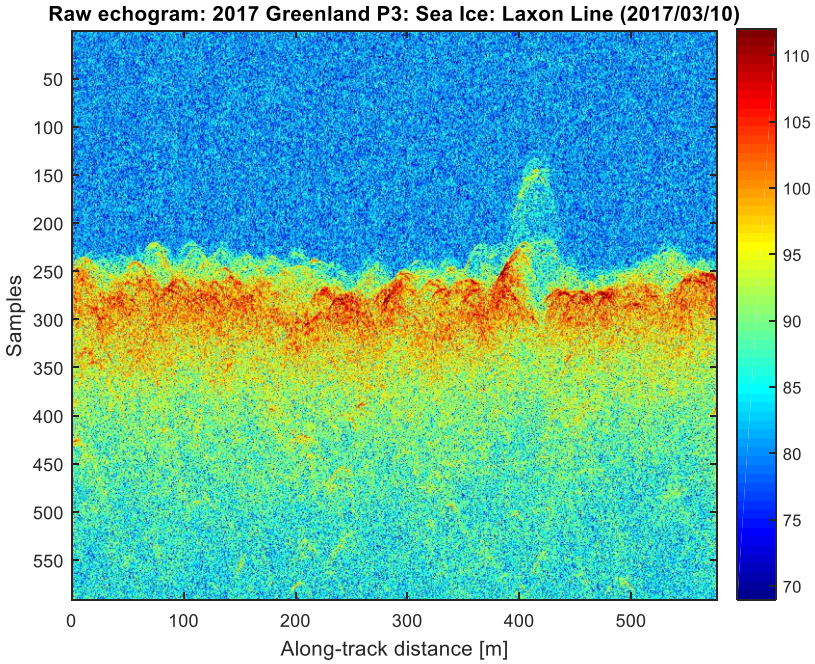

Figure 5:11: Raw echogram of snow radar from 2017 Greenland P3 mission

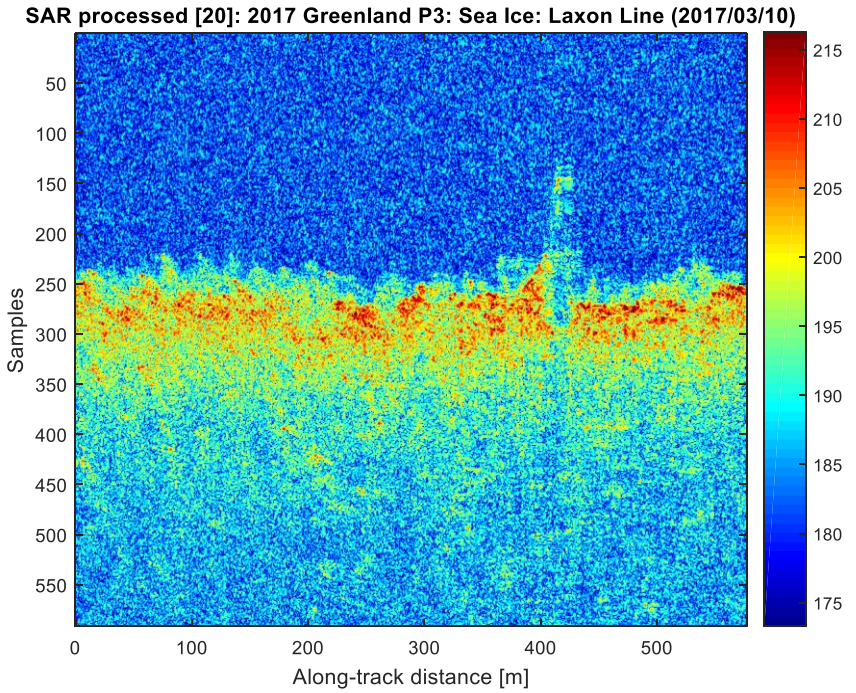

Figure 5:12: SAR processed echogram with aperture length of 20 range lines

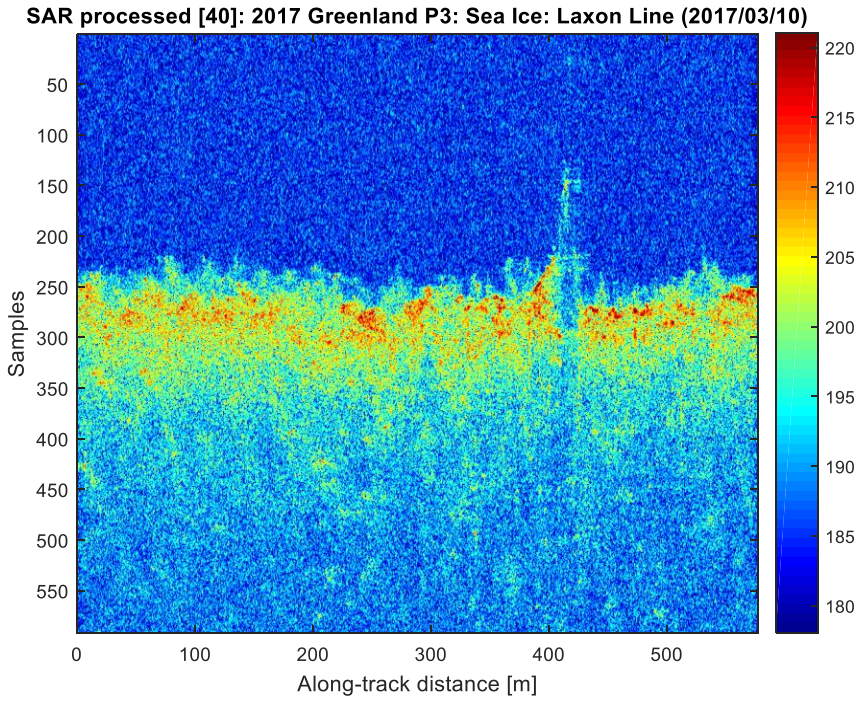

Figure 5:13: SAR processed echogram with aperture length of 40 range lines

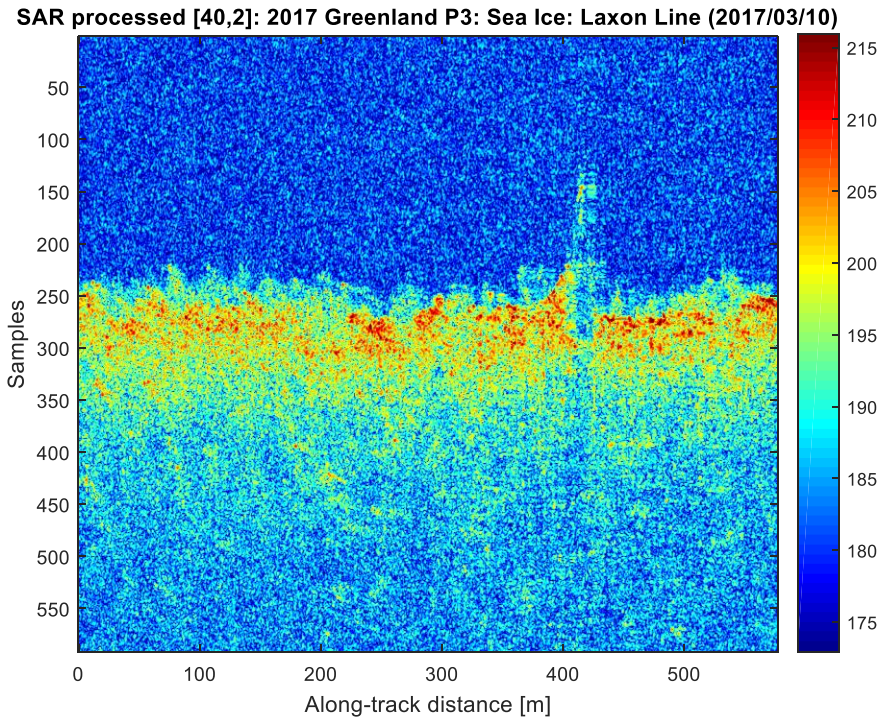

Figure 5:14: Multilook SAR processed echogram with aperture length of 40 range lines and 2 looks

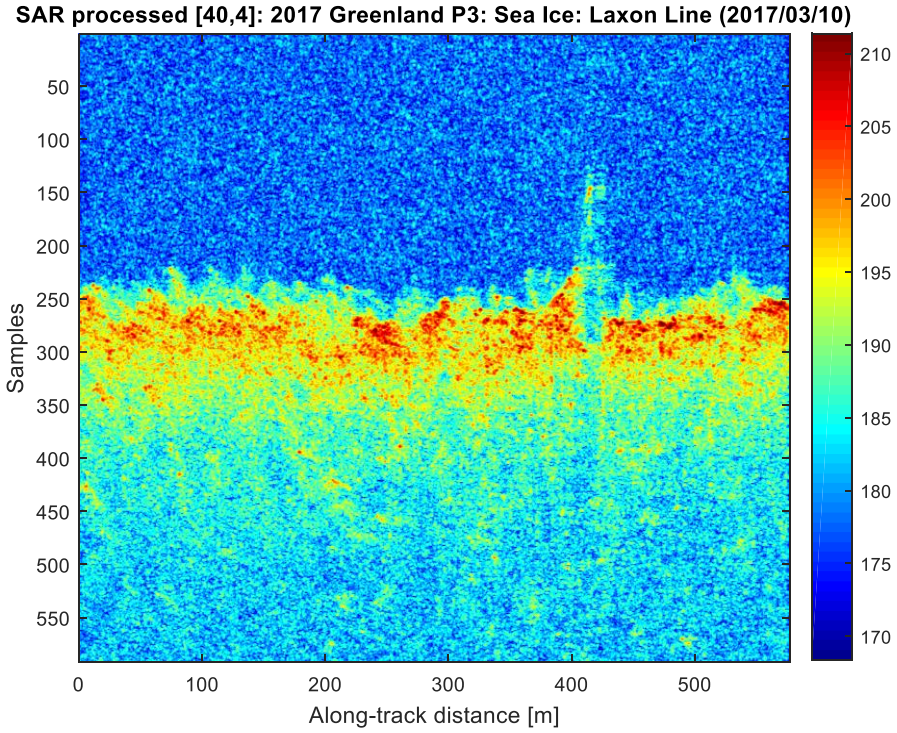

Figure 5:15: Multilook SAR processed echogram with aperture length of 40 range lines and 4 looks

From the images shown above, it is evident that multilook SAR processed echogram with 40 range lines and 4 looks optimum.

A part of the above data is shown in fig. 5.16 with various SAR parameters too see what would be the optimum SAR parameters.

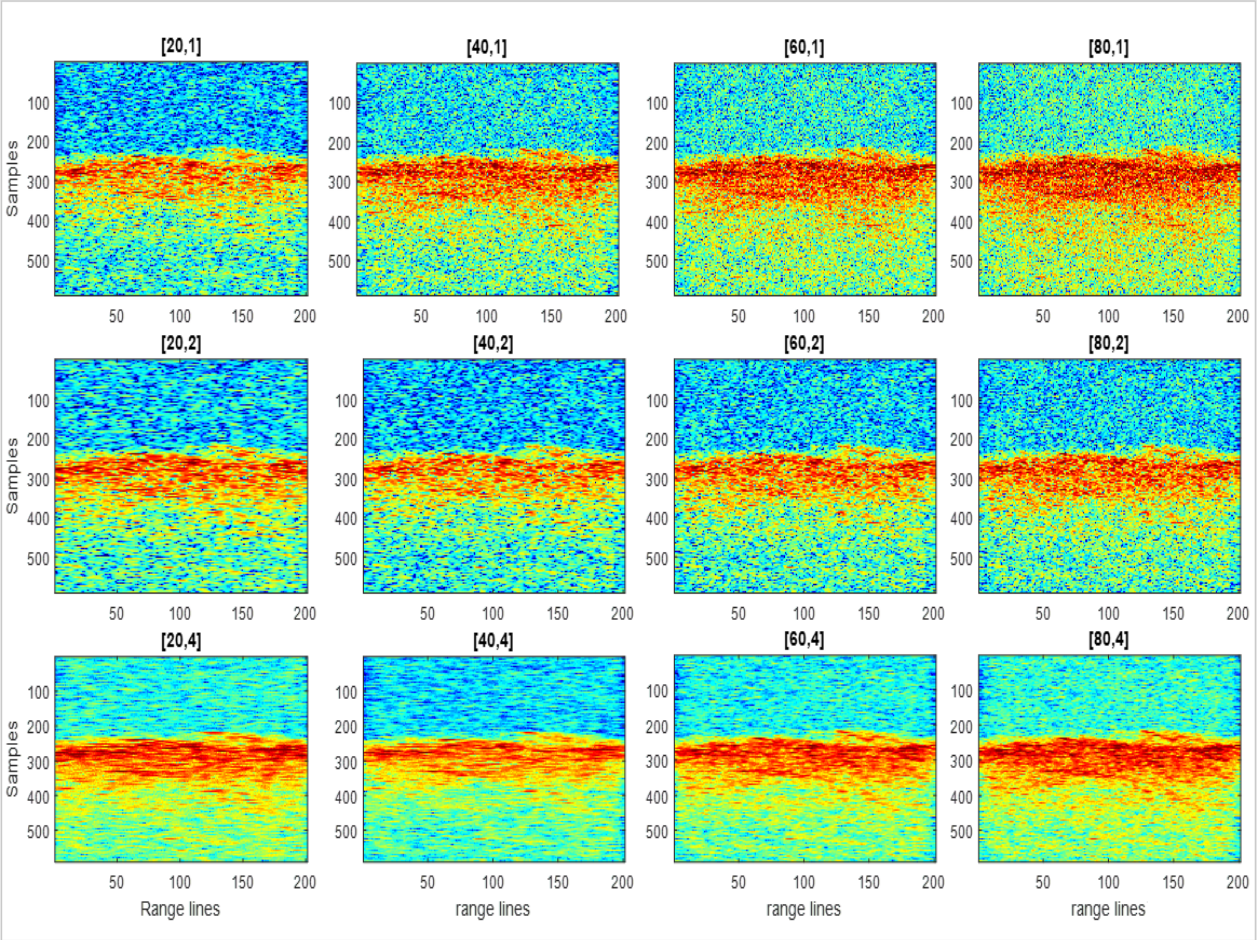

Figure 5:16: SAR processed data over sea ice with different aperture lengths and looks

A point reflector from the above data is processed with different aperture lengths and looks to see how individual point targets are processed with SAR. The point target and the SAR processed results are shown in Fig. 5.17 and 5.18.

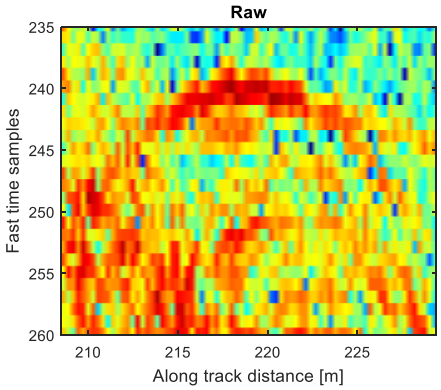

Figure 5:17: Point target from the above data

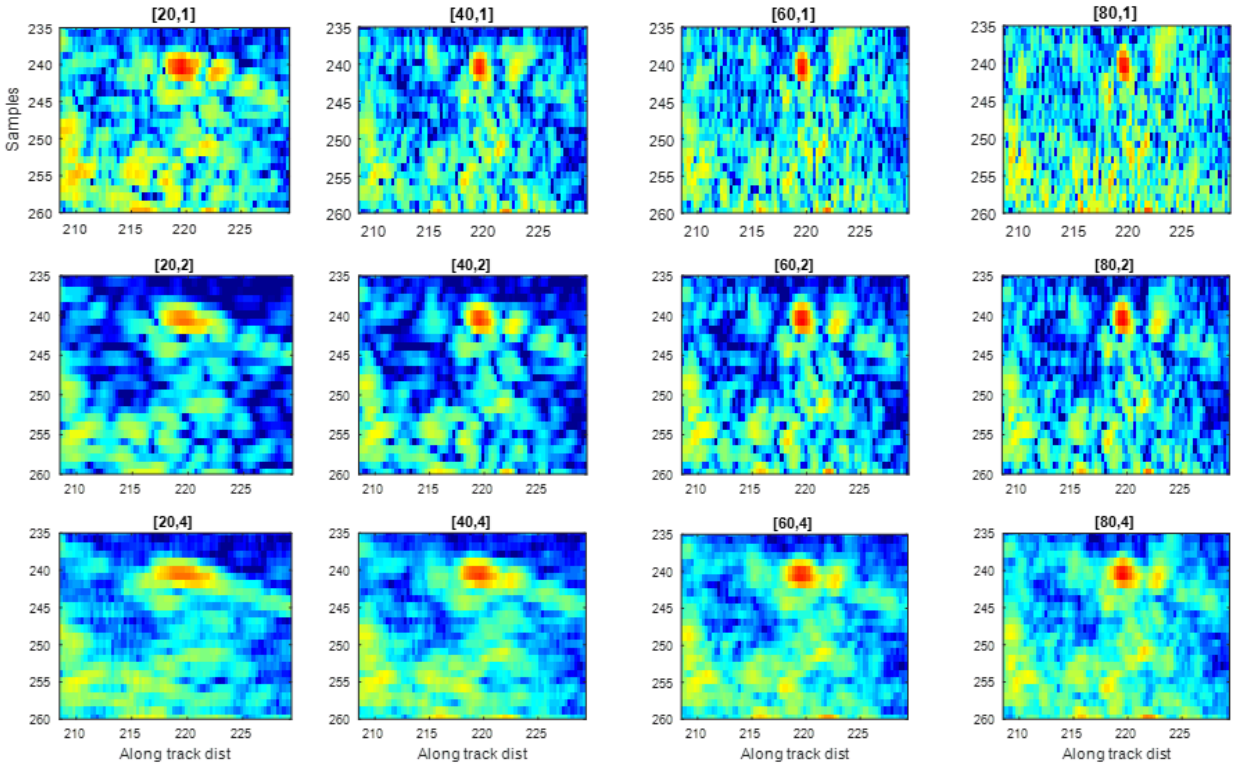

Figure 5:18: SAR processed point target for various SAR parameters

The SNR and Ascopes are calculated for the point target and are plotted as shown in fig. 5.19.

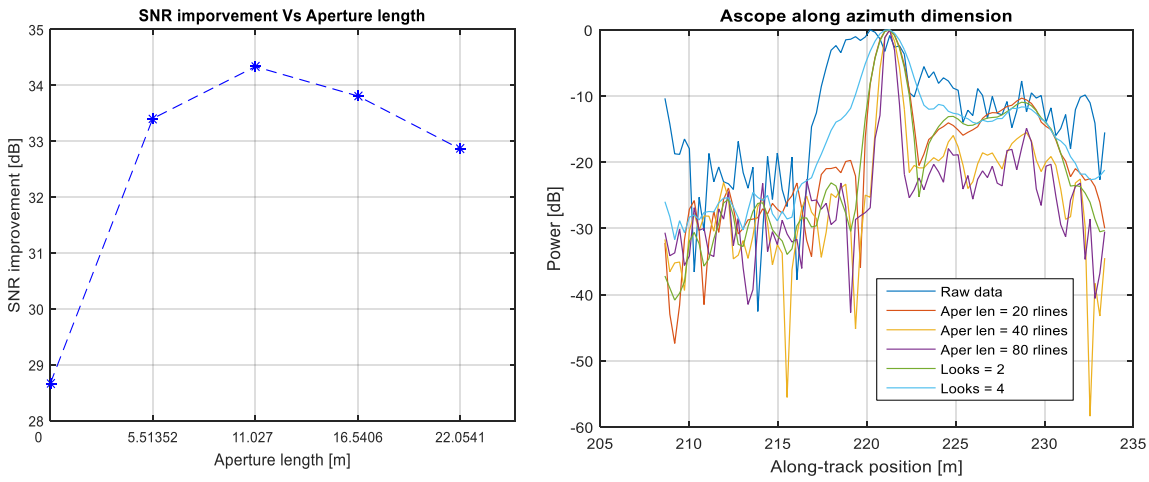

Figure 5:19: SNR and Ascope of the point target shown in fig. 5.17

The SNR values and the azimuth resolution are shown in below table

Table 9: SNR values and Azimuth resolutions of point target in 5.17

[Aper len, # looks]	SNR (dB)	Azimuth resolution (m)
Raw data	28.66	3.9455
20, 1	33.40	1.8615
40, 1	34.33	0.7451
80, 1	32.85	0.5818
40, 2	34.27	1.2606
40, 4	35.15	1.8840

From the SNR and azimuth resolution values, optimum parameters would be 40 range lines and 4 looks. To check if this is the same with other point target from the same data, we have chosen one more point target data and SAR processed with different parameters. The point target chosen and the SNR plot is shown in fig. 5.20.

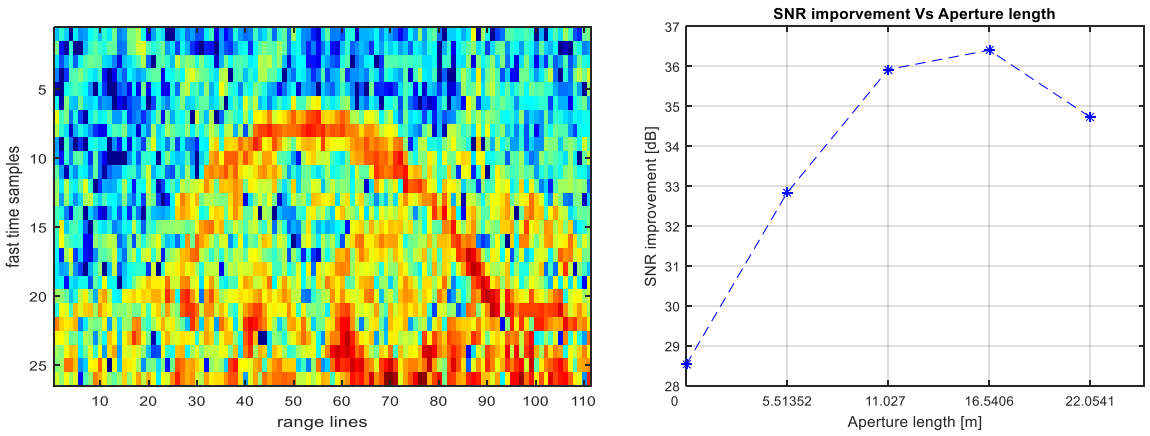

Figure 5:20: Point target data and the SNR for increasing aperture lengths

For this point target, SNR improvement can be found for upto 60 range lines unlike the earlier point target case. So choosing the aperture length is a bit tricky and depends on the data. Longer apertures might be optimum for perfect point targets but for distributed targets, the SNR is not constant all through the antenna footprint and decreases as we move away from the nadir position. The concept of distributed targets and how SNR varies is described by Logan Smith in [46].

Some other field data examples are shown here. Below are the echograms for Sea Ice data collected on May 4th, 2016 in South Canada Basin with 2-8 GHz snow radar. It can be seen from the echograms and SAR processed images shown in fig. 5.21 to 5.24 that snow-air interface and snow-ice interface can be clearly distinguished from SAR processed image with 40 range lines and 4 looks.

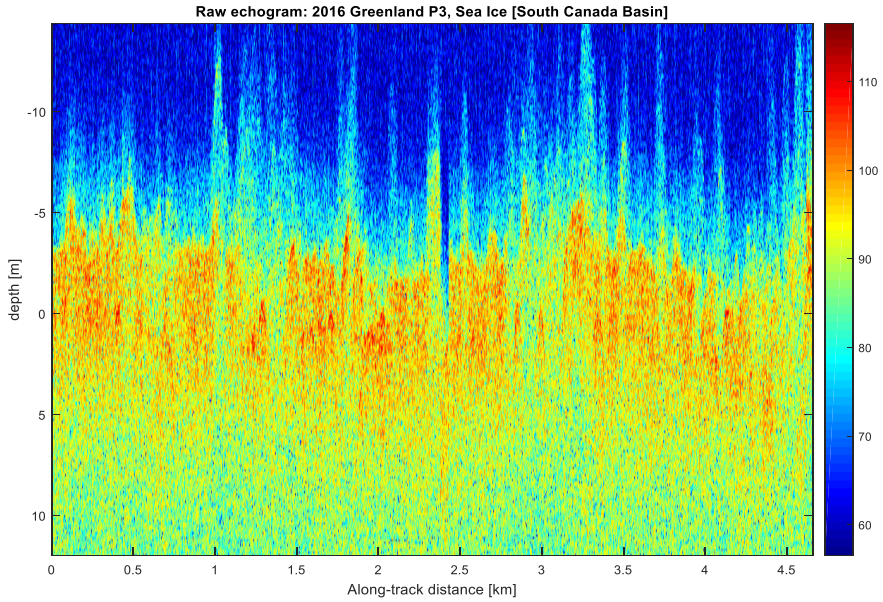

Figure 5:21: Raw echogram of sea ice

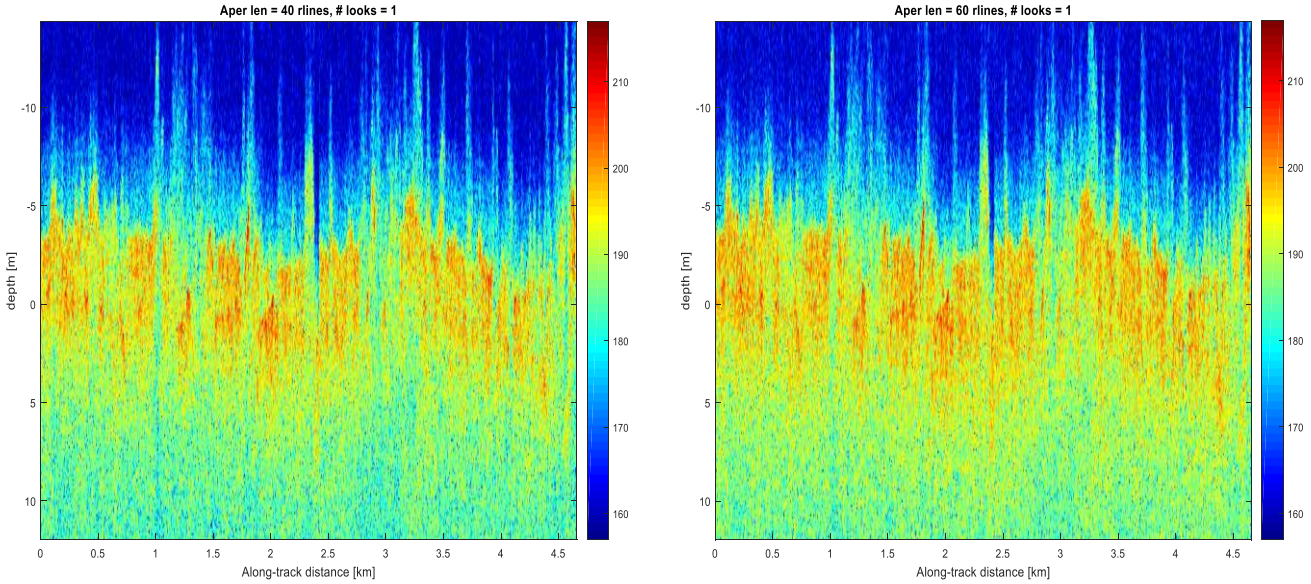

Figure 5:22: SAR processed echograms with different aperture lengths and 1 look.

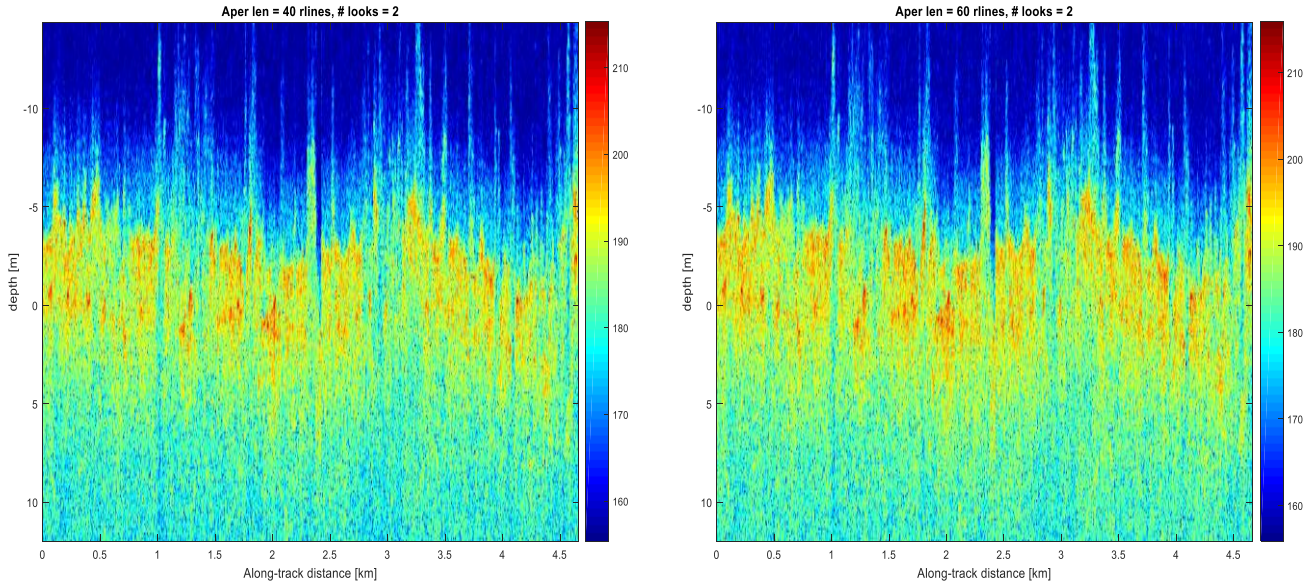

Figure 5:23: SAR processed echograms with different aperture lengths and 2 looks

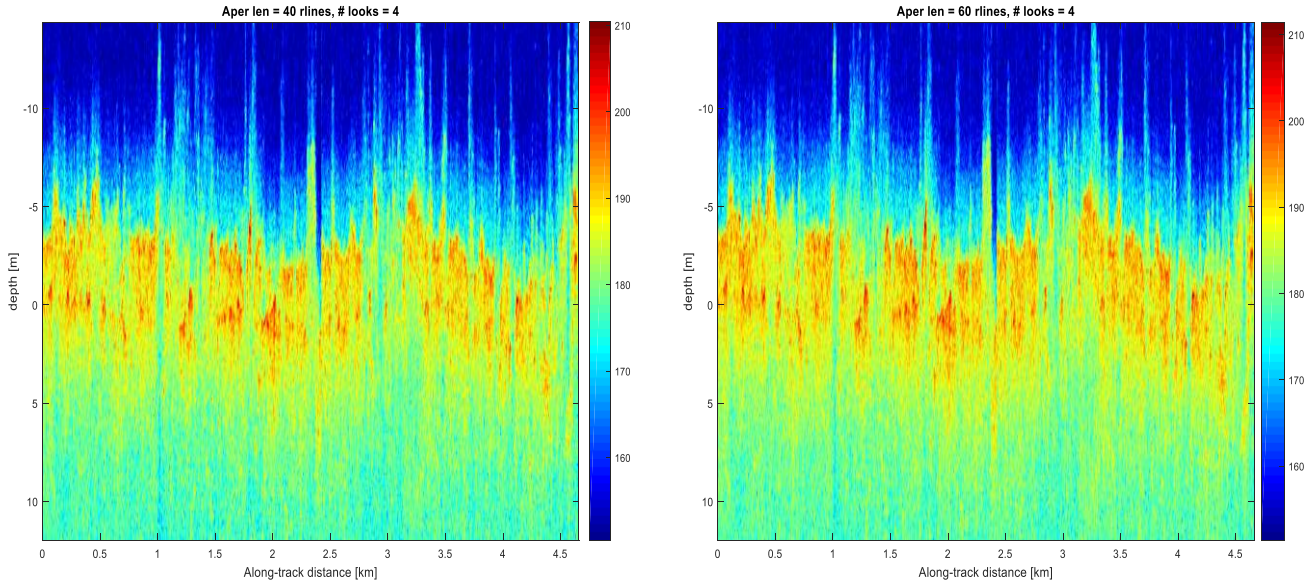

Figure 5:24: SAR processed echograms with different aperture lengths and 4 looks

This echogram has a rough surface and to see if the phase variation due to the surface roughness degrades the SAR performance, a point target data is selected from the data shown in fig. 5.21.

The point target before and SAR processing with different aperture lengths and looks are shown in fig. 5.25 and 5.26.

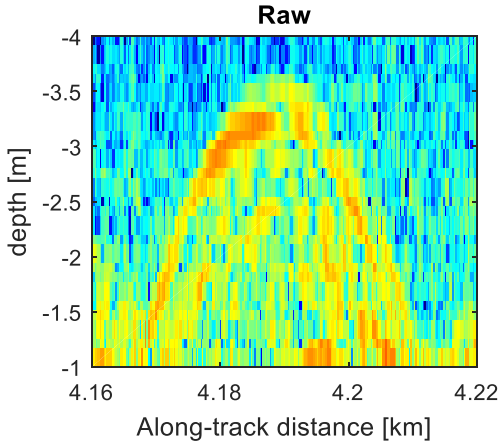

Figure 5:25: Point target before SAR processing

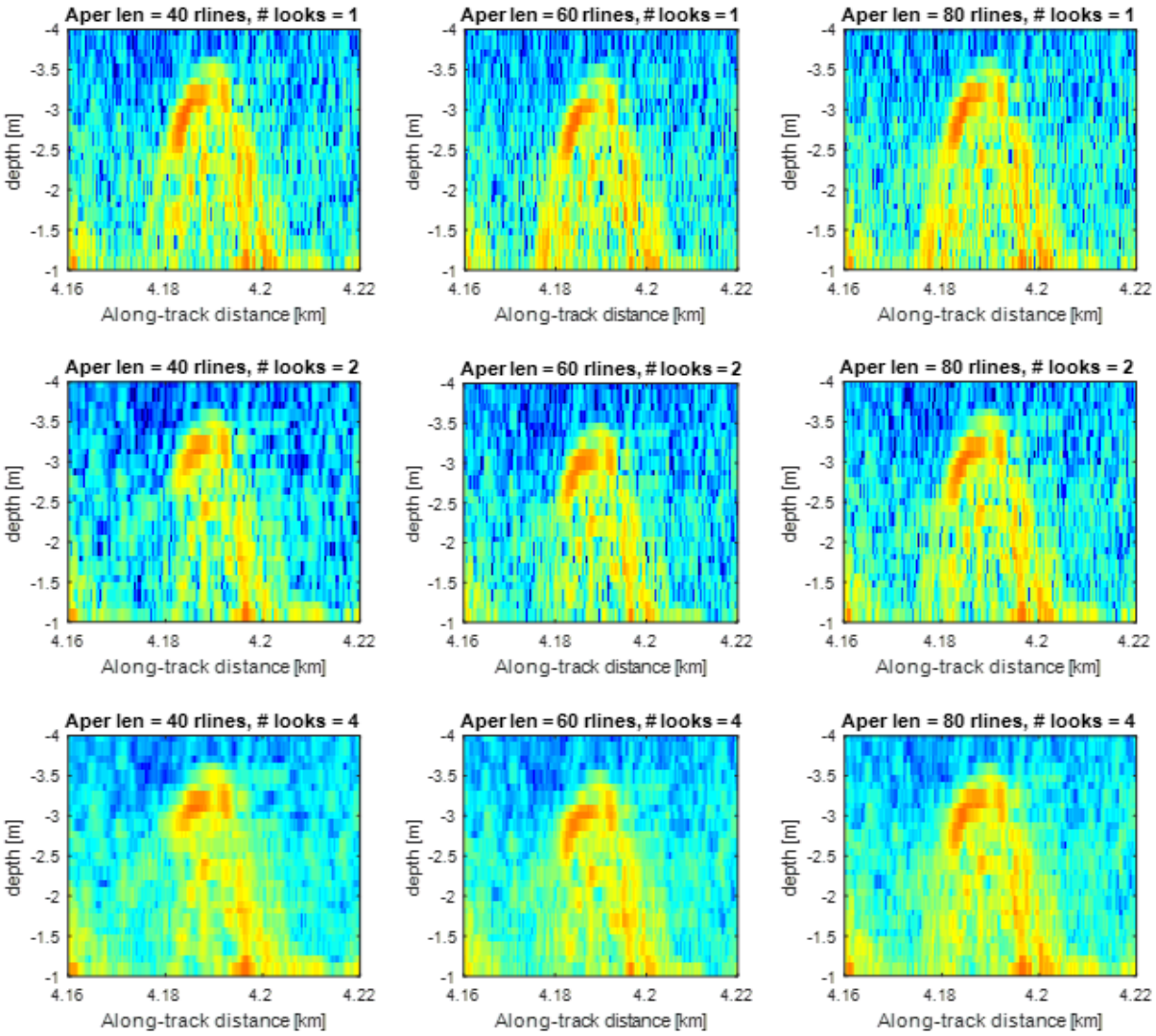

Figure 5:26: SAR processed point target for various aperture lengths and looks

Due to the surface roughness the phase errors are not properly compensated for 1 look and when the number of looks is increased, we get better results. Aperture length of 40 range lines and 2 looks give an optimum result.

Now we have sea ice data collected on 17th March in 2014 Greenland P3 mission around North Beaufort Loop West Barrow. Below figures shows the raw and SAR processed data with different parameters. SAR processed echograms with 40 range lines gave clear snow depth measurement.

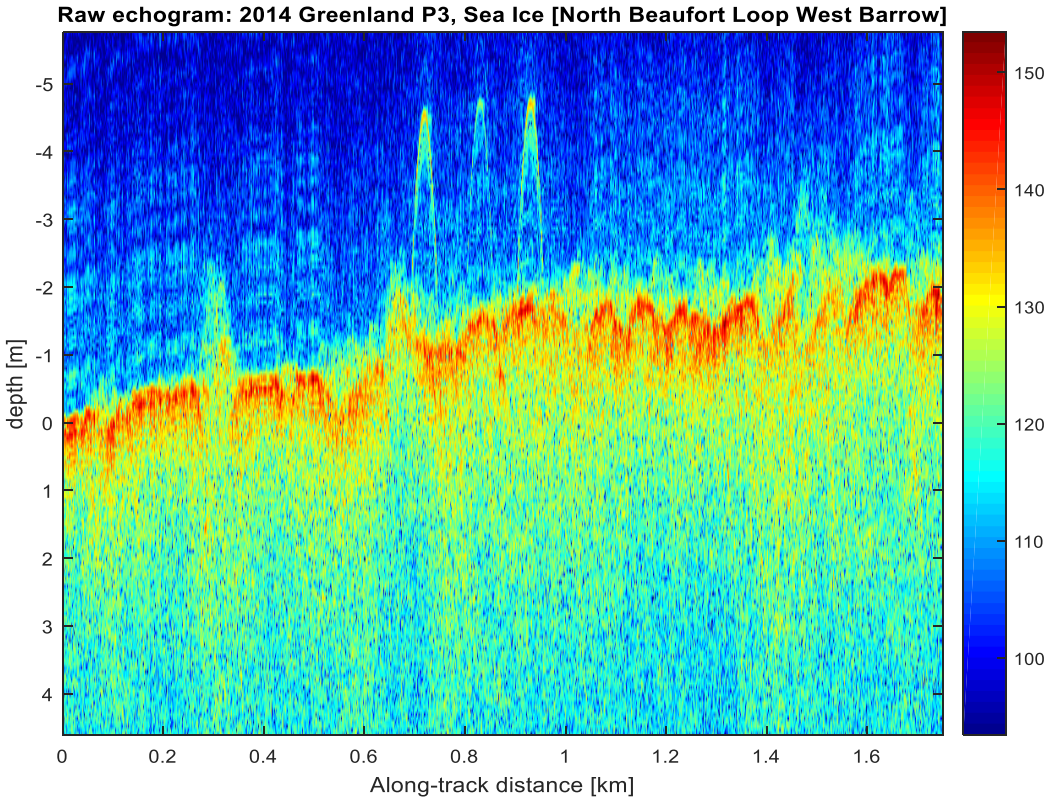

Figure 5:27: Raw echogram of sea-ice data

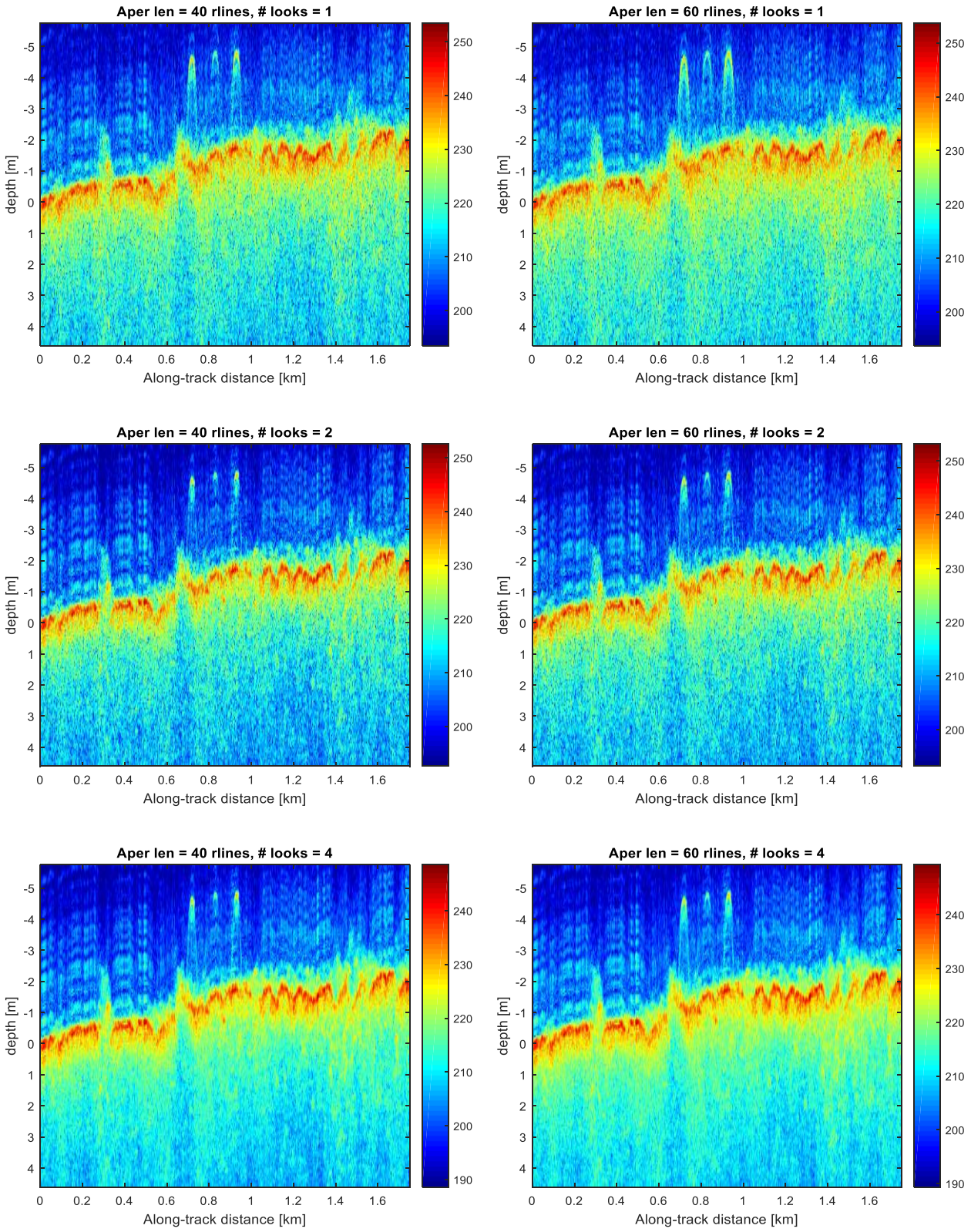

Figure 5:28: SAR processed echograms with different SAR parameters

Raw and SAR processed echograms of snow depth for data collected over Cryovex 2 sea ice data from 2017 Greenland P3 mission with 2-18 GHz bandwidth are shown below in fig. 5.29 and 5.30.

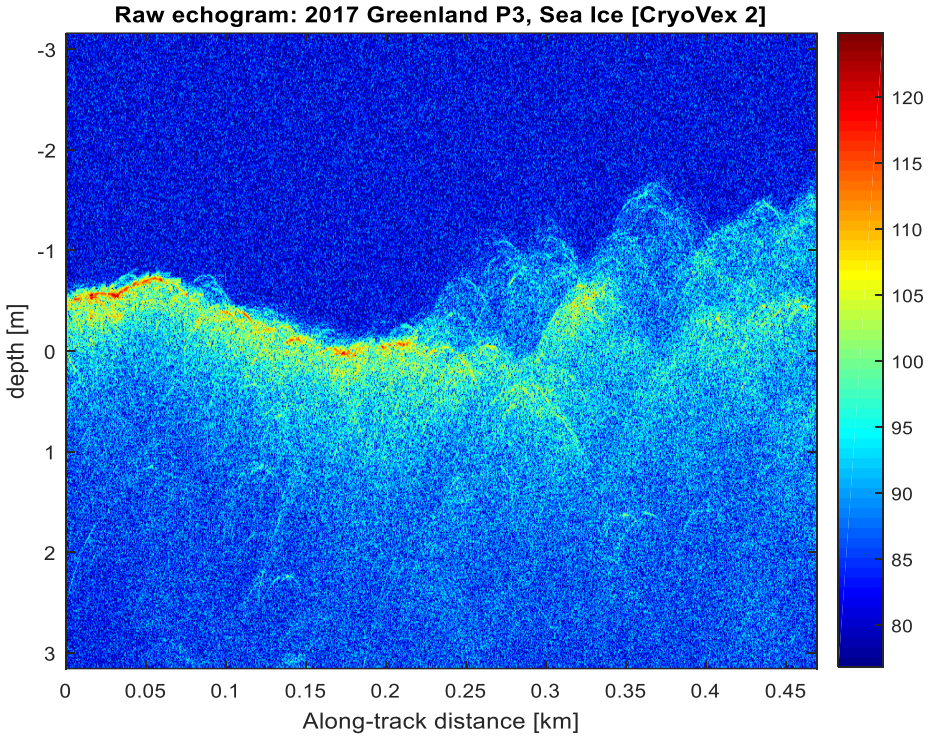

Figure 5:29: Raw echogram

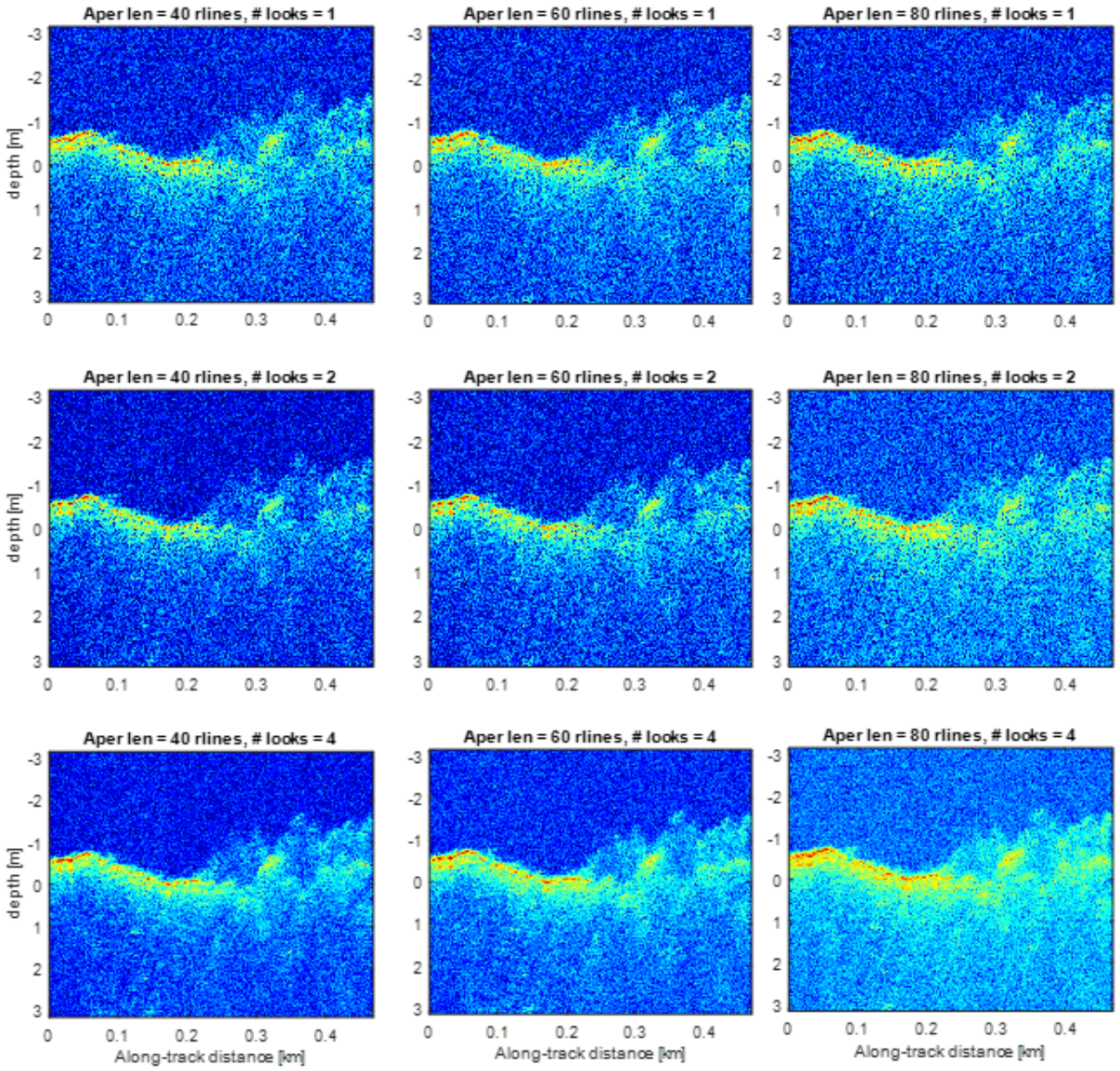

Figure 5:30: SAR processed echograms for various aperture lengths and looks

5.3 Low and High-Altitude data

Snow radar collected both low and high-altitude data over the same region in the west Greenland near Kangerlussuaq during 2016 Greenland P3 mission on May 18, 2016 and May 19, 2016 respectively. The radar parameters are changed for the snow radar operating at High altitude. The frequency of operation was changed from 2-8 GHz to 2-5 GHz for high altitude. From the GPS data, two flight lines were seen to be crossing over a point as shown in below fig. 5.26.

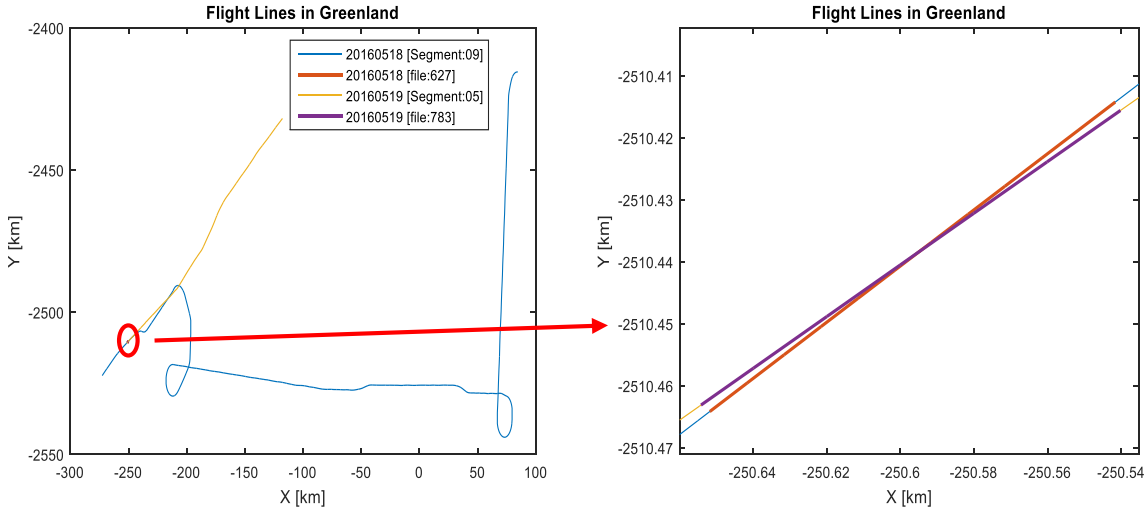

Figure 5:31: Flight lines on May 18, 2016 and May 19, 2016 from Greenland P3 mission

The raw and SAR processed echograms for both the low and high altitude data are shown in below figures from 5.27 to 5.31.

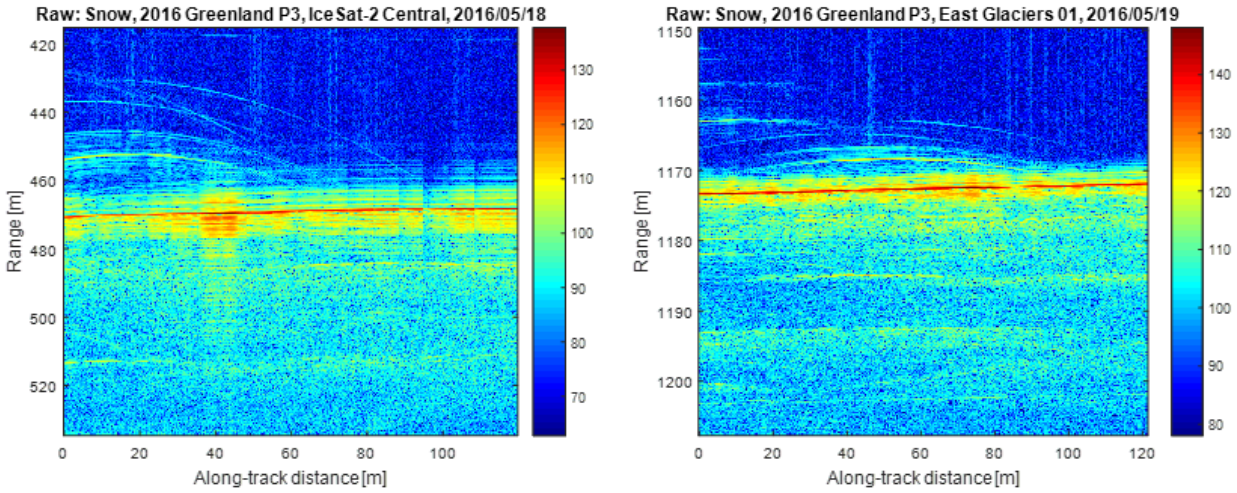

Figure 5:32: Raw echograms for the above data. Left: Low altitude; right: High altitude

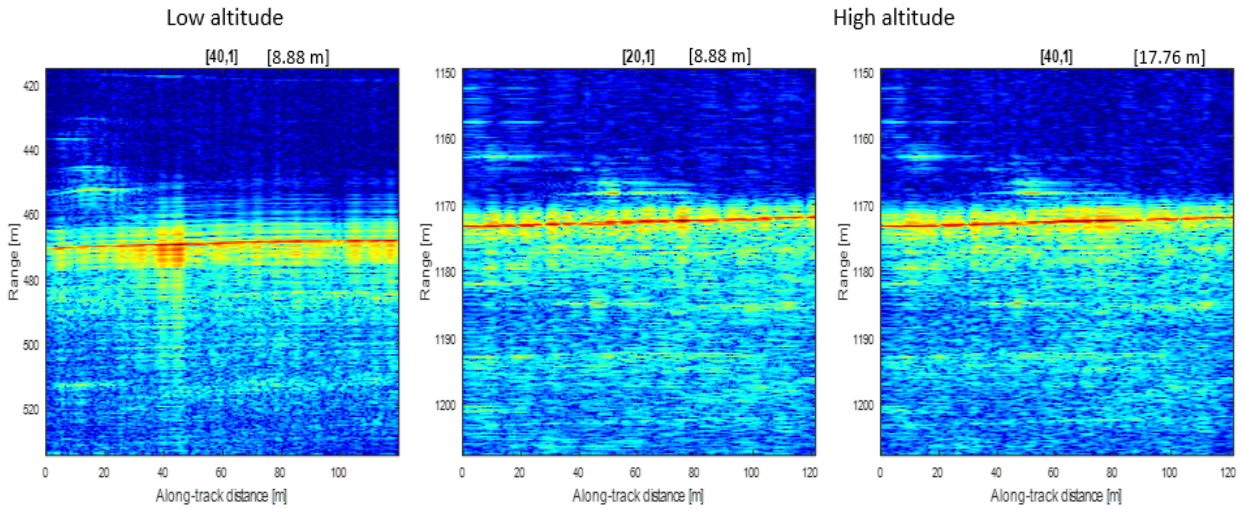

Figure 5:33: SAR processed echograms for 1 look (i) Low altitude with 40 rl; (ii): High altitude with 20 rl; (iii): High altitude with 40 rl

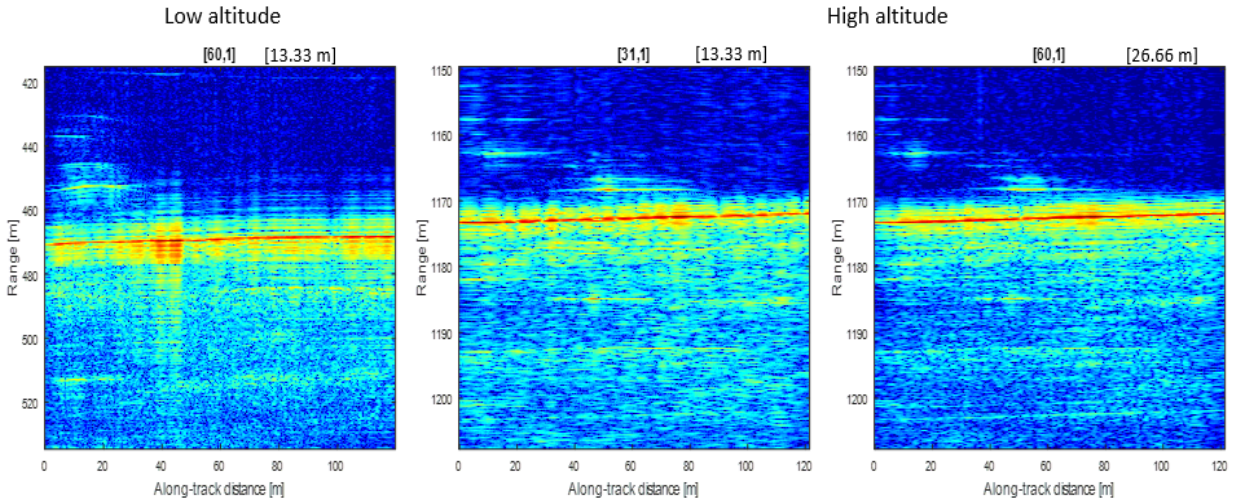

Figure 5:34: SAR processed echograms for (i) low altitude with 60 range lines; (ii): High altitude with 31 range lines and; (iii): High altitude with 60 range lines

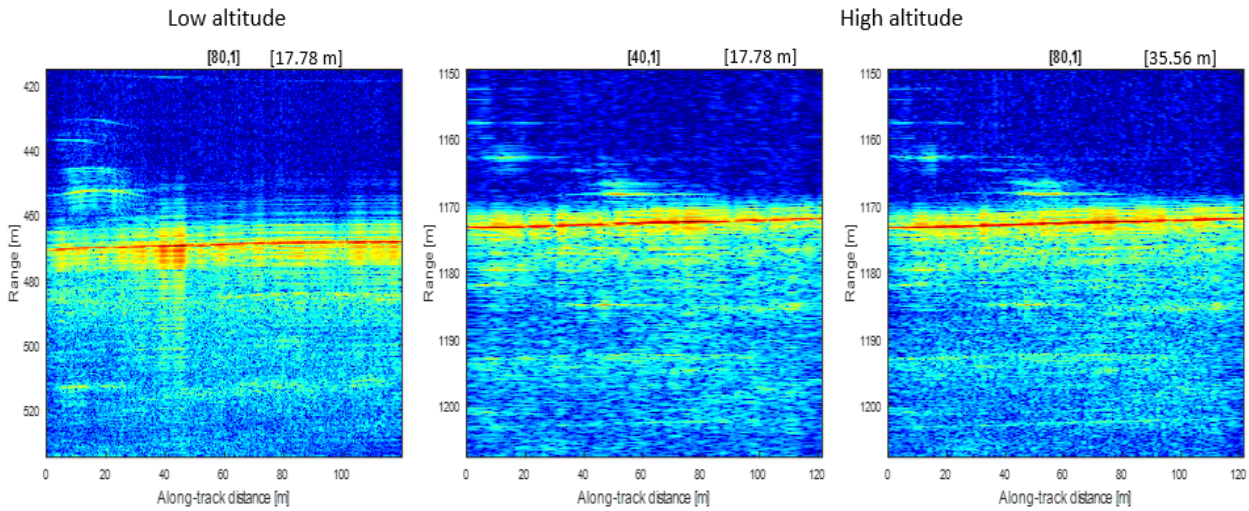

Figure 5:35: SAR processed echograms for (i) low altitude with 80 range lines; (ii): High altitude with 40 range lines and; (iii): High altitude with 80 range lines

It can be seen from the images that SAR processed echograms with aperture length of 40 range lines and 4 looks better and hence these can be considered as the optimum parameters. But the azimuth spacing of low altitude data is 0.2221 m and that of high altitude is 0.4356 m and hence the optimum aperture length for high altitude is almost double to that of low altitude data.

The TDC SAR simulator is built and tested on point target data and also on different data collected from various seasons. For all the data sets, 40 range lines aperture length and 4 looks gave the optimum results.

6 Summary

6.1 Summary

Accurate models of ice sheets are very much required to fully understand the effects of global warming on sea level rise. In order to obtain them, it is important to make sure that radar systems with high capabilities are developed and employed. At CReSIS an ultra-wideband radar system operating over a frequency range of 2-18 GHz is built to increase the radar system's performance and to map the ice sheets accurately. Along with the improved radar systems, it is equally important to employ efficient post processing techniques on the collected radar data that increase the radar's sensitivity and to analyze the snow models precisely. One such technique to improve SNR and resolution is SAR processing. Several SAR processing techniques both in time and frequency domain have been explained. In this work, a time domain correlation SAR processing technique is taken into consideration and explained.

Time domain correlation SAR processing is explained and validated with ideal simulated radar data. It increased the SNR and azimuth resolution as expected theoretically. The advantage of having longer aperture lengths in increasing the SNR comes with a cost of increased noise variance. The radar data have random multiplicative noise and it increases as the aperture length increase. Also, aircraft non-linearities have effect on the SAR processor. To overcome these effects, multilook SAR processing technique where the SAR aperture is divided in azimuth direction into number of looks has been introduced and explained. It is shown how multilooking SAR has improved the performance by reducing the noise variance and remediating the effect of aircraft non-linear motion. The effect of aircraft non-linearities at different altitudes vary since the aircraft footprint is large for higher altitudes and it is also shown with simulated data at different altitudes.

Now, the SAR processing is verified with point target data from the field data collected by the snow radar. The results were similar to the simulated ideal data. Now that the SAR simulator is validated, it is applied to the sea ice data collected by the snow radar in 2016 Greenland P3 and 2017 Greenland P3 missions as a part of the OIB campaign. The echograms were presented and observed that SAR processing could achieve fine azimuth resolution of 1.5 – 1.8 cm approximately for different data sets. Low and High altitude data collected over same region were also presented and compared.

The optimum processing parameters like the aperture length and number of looks depends on the application and our requirement. Though longer apertures give best resolutions for the simulated point target, there are limits on the aperture length when applied to real data. The antenna along-track beamwidth, platform errors, signal attenuation as the distance increases from the nadir position, large surface roughness that cause phase errors due to scattering angle are some to mention. Based on all these effects, it is better to keep mediocre aperture lengths of around 17 m for altitudes of 500 m and multilook the data.

6.2 Future Work

The first thing would be to test it on more data sets and see if this is applicable to those as well. Other SAR algorithms that exist in the CReSIS toolbox can be made adaptable to the snow radar and compare the results with this algorithm. We have seen that the optimum SAR parameters depend more on the data and thus could not quantitatively determine the optimum SAR parameters. Finding more quantitative ways of determining the optimum looks would be beneficial so we can incorporate that into the CReSIS toolbox and not analyze each data set.

References

[1] J. Hansen, L. Nazarenko, R. Ruedy, M. Sato, J. Willis, A. Del Genio, et al., "*Earth's energy imbalance: Confirmation and implications*," science, vol. 308, pp. 1431-1435, 2005.

[2] M. Vermeer and S. Rahmstorf, "*Global sea level linked to global temperature*," *Proceedings of the National Academy of Sciences,* vol. 106, pp. 21527-21532, 2009.

[3] D. Vaughan, J. Comiso, I. Allison, J. Carrasco, G. Kaser, R. Kwok, P. Mote, T. Murray, F. Paul, J. Ren, E. Rignot, O. Solomina, K. Steffen and T. Zhang, "*2013: Observations: Cryosphere. In: Climate Change 2013: The Physical Science Basis*," Cambridge University Press, Cambridge, United Kingdom and New York, NY, USA, 2013.

[4] Tedesco, M. (1971). *Remote sensing of the cryosphere.* New Jersey, NJ: Wiley Blackwell.

[5] J. A. Curry, J. L. Schramm, and E. E. Ebert, "Sea ice-albedo climate feedback mechanism," Journal of Climate, vol. 8, pp. 240-247, 1995.

[6] National Snow & Ice Data Center. (2017), "*Quick facts on Ice Sheets".* Retrieved from https://nsidc.org/cryosphere/quickfacts/icesheets.html

[7] Nesje, Atle and Svein Olaf Dahl, *Glaciers and Environmental Change*, pp 48, Oxford University Press, New York, 2000.

[8] J. D. Paden, R. R. Forster, I. Das, J. R. McConnell, M. Tedesco, C. Leuschen and P. Gogineni, "*Annual Greenland accumulation rates (2009–2012) from airborne snow radar*," The Cryosphere, vol. 10, pp. 1739-1752, 2016.

[9] B. Medley, "Airborne-radar and ice-core observations of snow accumulation in West Antarctica," University of Washington, 2013.

[10] U. B. Wade, "Airborne Measurement of Snow Thickness over Sea Ice," IGARSS 2008 - 2008 IEEE International Geoscience and Remote Sensing Symposium, Boston, MA, 2008, pp. III - 222-III - 225.

[11] Vaughan, D. G. et al. Observations: Cryosphere. In: Climate Change 2013: The Physical Science Basis. Contribution of Working Group I to the FifthAssessment Report of the Intergovernmental Panel on Climate Change [Stocker, T.F., D. Qin, G.-K. Plattner, M. Tignor, S.K. Allen, J. Boschung, A. Nauels, Y. Xia, V. Bex and P.M. Midgley (eds)]. (Cambridge University Press, 2013).

[12] I. Immoreev and D. V. Fedotov, *"Ultra-wideband radar systems: advantages and disadvantages"* in IEEE Conference on UltraWideband Systems and Technologies (UWBWST) Dig. Tech. Papers, May 2002, pp. 201–205.

[13] https://cresis.ku.edu/content/research/sensors/radar

[14] F. Rodriguez-Morales et al., "*Advanced Multifrequency Radar Instrumentation for Polar Research*," IEEE Transactions on Geoscience and Remote Sensing, Vol. 52, No. 5, pp. 2824-2842, 2013.

[15] P. Kanagaratnam, T. Markus, V. Lytle, B. Heavey, P. Jansen, G. Prescott, and S. Gogineni, "*Ultrawideband radar measurements of thickness of snow over sea ice*," IEEE. Trans. Geosci. Remote Sens., vol. 45, no. 9, pp. 2715–2724, Sep. 2007.

[16] H. P. Marshall and G. Koh, "*FMCW radars for snow research*," Cold Reg. Sci. Technol., vol. 52, no. 2, pp. 118–131, Apr. 2008.

[17] G. Koh, N. E. Yankielun, and A. I. Baptista, "*Snow cover characterization using multiband FMCW radars*," Hydrol. Process., vol. 10, no. 12, pp. 1609–1617, Dec. 1996.

[18] B. Panzer, C. Leuschen, A. Patel, T. Markus, and S. Gogineni, "*Ultrawideband radar measurements of snow thickness over sea ice*," in Proc. IEEE Int. Geosci. Remote Sens. Symp., 2010, pp. 3130–3133.

[19] B. Panzer, D. Gomez-Garcia, C. Leuschen, J. Paden, F. Rodriguez-Morales, A. Patel, T. Markus, B. Holt, and S. Gogineni, "*Development of an ultra-wideband radar for measuring snow thickness on sea ice*," J. Glaciol., vol. 59, no. 214, pp. 244–254, 2013.

[20] A. Patel et al., "*Fine-Resolution Radar Altimeter Measurements on Land and Sea Ice*," IEEE Transactions on Geoscience and Remote Sensing, Vol. 53, No. 5, pp. 2547-2564, 2015.

[21] A. Patel, S. Gogineni, C. Leuschen, F. Rodriguez-Morales, and B. Panzer, "*An ultra wide-band radar altimeter for ice sheet surface elevation and snow cover over sea ice measurement*," presented at the Amer. Geophys. Union, Fall Meeting, San Francisco, CA, USA, 2010, C41A0518.

[22] D. Gomez-Garcia, F. Rodriguez-Morales, P. Gogineni, and C. Leuschen, "*KU-band radar altimeter for surface elevation measurements in polar regions using a wideband chirp generator with improved linearity*," in Proc. IEEE Int. Geosci. Remote Sens. Symp., 2012, pp. 4617–4620.

[23] J. B. Yan, D. Gomez-Garcia, Y. Li, S. Gogineni, C. Leuschen, and J. Brozena, "*Ultra-wideband FMCW radar for airborne measurements of snow over sea-ice and land*," IEEE Transactions on Geoscience and Remote Sensing (submitted).

[24] J. B. Yan, S. Gogineni, B. Camps-Raga, J. Brozena, "*A dual-polarized 2–18 GHz Vivaldi array for airborne radar measurements of snow*", IEEE Transactions on Antennas and Propagation, vol. 64, no. 2, pp. 781-785, 2016.

[25] Yan, J.-B, S Gogineni, D Gomez-Garcia, J McDaniel, Y Li, D Challa, J Brozena, "*Multichannel ultra-wideband airborne radar for snow backscattering measurements*", IEEE International Symposium on Phased Array Systems and Technology (PAST), 2016.

[26] Website: https://data.cresis.ku.edu/#SR

[27] A. E. Robertson, "Multi-baseline Interferometric SAR for Iterative Height Estimation," Master's thesis, Brigham Young University, 1998.

[28] M. Soumekh, Synthetic Aperture Radar Signal Processing with MATLAB Algorithms. New York, NY: John Wiley & Sons, Inc., 1999.

[29] G. Franceschetti and R. Lanari, Synthetic aperture radar processing, F. Shapiro, Ed. CRC, 1999.

[30] M. E. Tiuri, A. H. Sihvola, E. Nyfors, and M. Hallikaiken, "The complex dielectric constant of snow at microwave frequencies," *Oceanic Engineering, IEEE Journal of,* vol. 9, pp. 377-382, 1984.

[31] C. Elachi, Spaceborne Radar Remote Sensing: Applications and Techniques. New York, NY: IEEE, 1988.

[32] D. P. Duncan, "Motion Compensation of Interferometric Synthetic Aperture Radar," Master's thesis, Brigham Young University, 2004.

[33] Lasswell, S. W., History of SAR at Lockheed Martin, Proceedings of the SPIE, Vol. 5788, 2005, pp. 1-12.

[34] Fahnestock, M., Bindschadler, R., Kwok, R. and Jezek, K., Greenland Ice Sheet Surface Properties and Ice Dynamics from ERS-1 SAR Imagery, Science, Vol. 262, No. 5139, pp. 1530-1534, Dec. 3, 1993

[35] Leuschen C., Gogineni S. P. and Tammana D., SAR Processing of Radar Echo Sounder Data, Geoscience and Remote Sensing Symposim, 2000. Proceedings IGARSS 2000. IEEE 2000 International.

[36] Joughin, I. R., Fahnestock, M. A., MackAyeal, D., Bamber, J. L. and Gogineni, S. P., Observation and Analysis of Ice Flow in the Largest Greenland Ice Stream, Journal of Geophysical Research, Vol. 106, No. D24, pp. 33021-34034, Dec. 27, 2001

[37] Cumming I.G., and Wong F. H., Digital Processing of Synthetic Apeture Radar Data, Algorithms and Implementation, Artech House, 2005

[38] D. P. Duncan, "Motion Compensation of Interferometric Synthetic Aperture Radar," Master's thesis, Brigham Young University, 2004.

[39] Soumekh M., Synthetic Aperture Radar signal processing with MATLAB Algorithms, John Wiley & Sons, Inc.

[40] Dr. Jilu Li, "Mapping of Ice Sheet Deep Layers and Fast Flowing Outlet Glaciers with Multi-Channel High-Sensitivity Radar", Doctoral Thesis, 2009.

[41] Yilmaz, Ö., Seismic Data Processing, Investigations in Geophysics, Society of Exploration Geophysicists, vol. 2, pp.507-518, 1987

[42] P. Oliver and D. Vidal-Madjar, "Empirical esetimation of the ERS-1 SAR radiometric resolution," Int. J. Remote Sens., vol. 15, no. 5, pp. 1109–1114, 1994.

[43] Alberto Moreira, "Synthetic Aperture Radar (SAR): Principles and Applications", Microwaves and Radar Institute.

[44] Alberto Moreira, "Improved Multilook Techniques Applied to SAR and SCANSAR Imagery", IEEE transactions on Geoscience and remote sensing, Vol. 29, No. 4, July 1991.

[45] A. Gunawardena and D. Longstaff, "A matched filter based synthetic aperture radar (SAR) algorithm for stepped frequency ground penetrating radar," Proceedings International Radar Conference, Alexandria, VA, 1995, pp. 239-243.

[46] Logan Sanders Smith, "Validation of CReSIS Synthetic Aperture Radar Processor and Optimal Processing Parameters", Thesis dissertation.